

©Copyright 2013

Andrew A. Ganse

Uncertainty and Resolution in Full-Waveform, Continuous,
Geoacoustic Inversion

Andrew A. Ganse

A dissertation
submitted in partial fulfillment of the
requirements for the degree of

Doctor of Philosophy

University of Washington

2013

Reading Committee:

Robert I. Odom, Chair

Kenneth Creager

John Booker

Program Authorized to Offer Degree:
Department of Earth and Space Sciences, University of Washington

University of Washington

Abstract

Uncertainty and Resolution in Full-Waveform, Continuous, Geoacoustic Inversion

Andrew A. Ganse

Chair of the Supervisory Committee:
Professor Robert I. Odom
Department of Earth and Space Sciences

The ocean geoacoustic inverse problem is the estimation of physical properties of the ocean bottom from a set of acoustic receptions in the water column. The problem is considered in the context of equipment and spatial scales relevant to naval sonar. This dissertation explores uncertainty, resolution, and regularization in estimating (possibly piece-wise) continuous profiles of ocean bottom properties from full-waveform acoustic pressure time-series in shallow-water experiments. Solving for a continuous solution in full-waveform seismic and acoustic problems is not in itself new. But analyses of uncertainty, resolution, and regularization were not included in previous works in this category of ocean geoacoustic problem. Besides quantifying the quality of individual inversion results, they also provide an important tool: Methods and details in these topics build to a pre-experiment design analysis based on the problem resolution, which can be estimated without measurements (i.e. before the experiment takes place). The resolution of the bottom inversion is calculated as a function of array configuration, source depth, and range. Array configurations include 40-element horizontal line arrays (HLAs) from 200-1200m long towed at 10m depth, with source range defined as that to closest HLA element, and single and multiple vertical line arrays (VLAs) which cover the water depth. Monte Carlo analyses of the inversion within the local minimum show the extent to which the linear descriptions of uncertainty and resolution used in the experiment design analysis are valid approximations. Since full-waveform geoacoustic inversion is a nonlinear inverse problem, the resolution analysis results are dependent on the

choice of bottom model for which they are calculated. Resolution analyses for six widely differing bottom profiles are compared, and at the geometries and frequencies considered in this dissertation, the results and conclusions from the point of view of experiment design decisions are in fact largely similar, with the exception of the presence of a low velocity zone in the bottom model (from which acoustic energy does not return to the receivers). The techniques and conclusions in this work are appropriate when inverting for P-wave velocity profiles in shallow (200m) water, at relatively short (≤ 3 km) range with flat bottom, and at low frequency (~ 100 Hz).

TABLE OF CONTENTS

	Page
List of Figures	iii
List of Tables	vi
Chapter 1: Introduction and background	1
1.1 Motivation	1
1.2 Overview of the geoacoustic inverse problem	2
Chapter 2: Our full-wave geoacoustic forward problem	6
2.1 Experiment geometry	6
2.2 Ocean bottom model	9
2.3 Acoustic data	11
2.4 Derivatives of the forward problem	11
Chapter 3: Mathematical description of the inversion method	18
3.1 Overview	18
3.2 Frequentist regularized Gauss-Newton inversion	19
3.3 Objective function	23
3.4 Uncertainty and resolution	25
Chapter 4: Inversion of the full-wave geoacoustic problem	29
4.1 Objective function and choices of starting models	29
4.2 Data pre-processing	34
4.2.1 Bandpass filtering the noisy data	34
4.2.2 Down-weighting seafloor reflections in the data	35
4.3 Inverting a continuous bottom model with smoothing regularization	37
4.3.1 Solving for the solution model	38
4.3.2 Resolution and uncertainty of the solution model	42
4.3.3 Analyzing nonlinear aspects of model resolution and uncertainty via Monte Carlo	50

4.4	Inverting a piece-wise continuous bottom model: specifying layer discontinuities in the inversion	51
4.4.1	Knowledge of discontinuity locations	53
4.4.2	Inversion using discontinuity locations	54
4.4.3	Effects of error in discontinuity locations	55
4.4.4	Effects of data noise on level of structure between discontinuities	58
4.5	Effects of errors in the forward problem and in the model	62
4.5.1	Data noise vs. modeling error	62
4.5.2	Using empirical fits to relate physical properties	63
4.5.3	Source and receiver positioning errors	66
4.5.4	Unmodeled bathymetry	68
4.5.5	Internal wave variability in the water	70
4.5.6	Location/time-varying sea-surface roughness	72
4.6	Summary and conclusions	73
Chapter 5:	Resolution analysis of the geoacoustic problem for experiment design	75
5.1	Three levels of resolution summarization	78
5.1.1	Averaging kernels	78
5.1.2	Diagonals of the model resolution matrices	81
5.1.3	Trace of the resolution matrix	83
5.2	Resolution over varying experiment geometries and array configurations	87
5.2.1	Results at different source depths for given array configurations	87
5.2.2	Results for different array configurations at a given source depth	89
5.3	SVD analyses of those geometry and array comparisons	96
5.4	Monte Carlo analysis to examine where linear approximations of resolution and uncertainty are valid and invalid	102
5.5	Results compared between different candidate bottom profiles	106
5.6	Summary and conclusions	111
Bibliography	114
Appendix A:	Generalized singular value decomposition formulation of resolution	121
A.1	Definition of generalized singular value decomposition	121
A.2	Derivation of the resolution matrix in terms of the GSVD	122

LIST OF FIGURES

Figure Number	Page
2.1 Geometries for synthetic problem formulation	7
2.2 Raytrace depiction for this problem.	8
2.3 P-wave velocity model and associated profiles of S-wave velocity, P- and S-wave attenuations, and density.	10
2.4 Time and frequency representation of source pulse used in the forward problem.	12
2.5 Spectra of unfiltered and filtered received signal with various noise levels. . .	13
2.6 A multi-faceted view of a few derivatives in the Jacobian matrix.	17
4.1 Comparison of velocity and slowness forms of least-squares-based objective functions.	31
4.2 Three 2D slices through the high-dimensional geoacoustic objective function, in both velocity and slowness perturbations.	33
4.3 The time domain dataset before and after de-weighting of the seafloor interface reflections and multiples.	38
4.4 Tradeoff curve for inversions of data with noise $\sigma_d = 0.50$ using smoothing regularization.	40
4.5 Change in norm of model perturbation as a function of iteration number. . .	41
4.6 A selection of inverted models corresponding to points on the L-curve in Figure 4.4.	42
4.7 Model resolution matrices for the 7th, 10th, and 14th inverted models on the L-curve in Fig. 4.4.	43
4.8 Model resolution kernels and smoothed true model for 10th model result on the tradeoff curve in Figure 4.4.	45
4.9 Model solution uncertainties to first order for smoothing regularization without specifying layer discontinuities.	46
4.10 Tradeoff between uncertainty and resolution in the geoacoustic solution. . . .	47
4.11 Model solutions for the same problem from several different starting models. .	48
4.12 Plots of superposition of noisy “measured” data and predicted data, and of residuals.	49
4.13 Monte Carlo solutions to the Chapter 4 VLA problem.	51

4.14	Monte Carlo estimates of $\mathbf{Rm}_{\text{true}}$ and averaging kernels for the Chapter 4 VLA problem.	52
4.15	The original and the new regularization matrix \mathbf{L} which specifies model discontinuities.	56
4.16	Piece-wise continuous inversion result for two different starting models.	57
4.17	Smoother and rougher solutions for four discontinuities specified in the regularization.	58
4.18	Solution given errors in discontinuity locations supplied to the regularization.	59
4.19	Comparing structure in piece-wise continuous inversion solutions over increasing noise.	61
4.20	Singular values and first singular vectors of the Jacobian matrices of derivatives with respect to P-wave slowness, S-wave slowness, density, and P- and S-wave attenuations.	65
4.21	Sensitivity of the data misfit χ^2 to perturbations in V_s and ρ with respect to the nominal values given by the Hamilton regressions.	66
4.22	The relationship between RMS bathymetry height and the change in travel-time of the first bottom reflection for each receiver.	70
4.23	Acoustic arrival time variations due to water column variability over five hours, from SW06 experiment (reprinted from reference [31]).	72
5.1	Rays for the experiment geometries and one of the bottom model profiles used in the analysis.	76
5.2	Averaging kernels computed from complete synthetic inversions with a 1km HLA.	80
5.3	Resolution matrix diagonals computed from the complete synthetic inversions of the VLA problem.	82
5.4	Relation between resolution matrix diagonals and averaging kernels.	83
5.5	Resolution matrix traces computed from the complete synthetic inversions of the VLA problem.	84
5.6	Averaging kernels as a function of depth, source range, and source depth for a 1km HLA.	90
5.7	Averaging kernels as a function of depth, source range, and source depth for a 200m HLA.	91
5.8	Averaging kernels as a function of depth, source range, and source depth for a VLA.	92
5.9	Improvements in stability and resolution with lengthening and positioning of HLA.	93
5.10	Improvements in stability and resolution with lengthening and positioning of VLA.	94

5.11	Range dependence of singular value spectra corresponding to the 200m and 1km HLA problem geometries in Figure 5.6.	97
5.12	Singular vectors corresponding to the 1km and 200m HLA problem geometries in Figure 5.11.	99
5.13	Monte Carlo solutions to the Chapter 5 VLA problem.	103
5.14	Monte Carlo estimates of $\mathbf{Rm}_{\text{true}}$ and averaging kernels for the Chapter 5 VLA problem.	105
5.15	Six different bottom model profiles used to compare effects of “true” model on the resolution results.	107
5.16	Overlaid resolution diagonals for six different bottom model profiles in the VLA problem.	109
5.17	Zoom and labeling of two of the overlaid resolution diagonal plots from Figure 5.16.	110

LIST OF TABLES

Table Number	Page
4.1 Comparison of largest singular values of Jacobian matrices w.r.t. problem parameters.	64

ACKNOWLEDGMENTS

The author wishes to express appreciation to committee members: R. Odom, K. Creager, J. Booker, and K. Bube. Significant discussions and support outside committee: R. Andrew (APL-UW), S. Dosso (U-Vic), T. Maravina (STAT-UW), D. Tang (APL-UW), J. Mercer (ESS-UW & APL-UW), K. Williams (APL-UW), J. Lundin (ESS-UW), A. White (ESS-UW). Institutional appreciation: Applied Physics Laboratory for the generous APL-UW Graduate Fellowship, US Office of Naval Research (ONR) for support of intervening and concurrent project-work. Also thanks to R. Andrew and J. Mercer for great flexibility and encouragement while working for them at the same time as finishing this dissertation.

DEDICATION

To my wife Adrienne and children Aubrey and August –
I love you and I thank you for persevering all this time.

“Daddy! August and I wrote a huge storybook for you. It’s called ‘PHD’ and it’s a
thousand hundred hundred pages long. It took a really long time to write, like almost two
whole days!” – five-year-old Aubrey Ganse

Chapter 1

INTRODUCTION AND BACKGROUND**1.1 Motivation**

The Navy’s engineering interest in improving sonar performance in shallow waters is dependent upon an understanding of features and properties in the ocean subfloor which interact with the sonar acoustics. This need in turn drives the geophysical science goal of understanding the nonlinear inversion of ocean bottom properties from hydrophone-based measurements given an acoustic source in the water, within the context of typical naval equipment and frequencies. This problem is closely related to terrestrial seismic inversion and certainly to marine seismic inversion, but at different frequencies and size scales than typically used in seismology and oil exploration work. While specific formulations vary across the field of geoacoustic inversion, the overall problem is to estimate the ocean bottom properties as a function of position in the top few hundred meters of the ocean bottom, given finite measurements of acoustic pressure from arrays of hydrophones located in the water column.

With a few exceptions (clarified shortly), the geoacoustic inversion community has largely focused on Bayesian estimation of an ocean bottom described by a handful of parameters – a couple of homogeneous or constant-gradient layers. In the exceptions involving continuous bottom inversion, uncertainty and resolution of the solution are rarely computed and have not been explored deeply, and virtually not at all for the waveform geoacoustic inverse problem. The advantage to considering the problem in terms of waveform inversion is that Parseval’s Theorem shows that a least-squares based objective function can be the same for time domain data, which is considered in this dissertation, as it is for frequency domain data, which has a successful history in the geoacoustic community under the name “matched field inversion”. (Some forms of matched field inversion allow for unknown source spectrum elements – the complete source spectrum is assumed known

in this time and frequency domain problem equivalence.) At the same time, waveform inversion in the time domain has a recent history in the seismic inversion literature with success via linearization methods [42, 41, 74, 75, 8, 77], and full-waveform data provides more information about the model than say travel-time data.

This dissertation quantitatively explores the uncertainty, resolution, and regularization in (possibly piece-wise) continuous geoacoustic waveform inversion, to build a framework for quantitatively planning the design of a geoacoustic experiment based on the details of the inversion that the experiment is supporting.

1.2 Overview of the geoacoustic inverse problem

The estimation of ocean bottom geoacoustic properties from acoustic receptions in the water column is a nonlinear inverse problem that is inherently unstable and non-unique. There are two broad approaches to solving these geoacoustic estimation problems in the underwater acoustics community, as succinctly stated by Chapman [9]. The first aims only to reproduce the scattered sound field in the ocean for the purposes of sonar performance prediction, and thus is not overly concerned with the non-uniqueness of the ocean bottom solution itself. The second aims at actually trying to learn, as accurately as possible, something about the true ocean bottom in the area, distinguishing what can be uniquely learned from what cannot. This second approach is also of value to the sonar performance prediction community, in that databases of ocean bottom properties used to model the scattered sound fields could be independent from the geometries and frequencies of the experiments originally used to estimate them, or in allowing further analysis of geological features such as those which cause “geoclutter” (undesirable but non-random components in the sonar signals, from buried ancient riverbeds for example[57]). To this end, in this work we explore details in the inversion of the ocean bottom in this second approach, the approach of geophysical inverse theory.

There have been numerous examples of the geoacoustic inverse problem seen in the literature over the years, with many variations and formulations [54, 56, 55, 43, 23, 10, 20, 17, 18, 6, 53, 50, 51, 52, 38, 37, 35, 16]. Commonly in the underwater acoustics community, probabilistic methods are employed to estimate the properties of just a few layers, assumed

to be homogenous or with a constant depth-gradient. For those focused purely on reproducing the oceanic scattered sound field, this minimal parameterization of the ocean bottom may be perfectly adequate for that purpose. But for those interested in discovering as much as possible about the properties and structure of the ocean bottom in a particular area, one may potentially gain more information about the ocean bottom by formulating it as a (possibly piece-wise) continuum, and letting the data and physics of the problem determine the resolution of the features resolved in the bottom. Typically this might take the form of a more smoothly varying structure between layer discontinuities. A relatively small number of ocean geoacoustic papers have in fact used some kind of continuous inversion approach in other problem formulations in the past [54, 43, 53, 50, 51, 6, 52]. In fact, Rajan [56, 55] briefly explored aspects of full-waveform continuous geoacoustic inversion in two papers in the early nineties, but analyses of uncertainty, resolution, and regularization were not included in that work, and these are what ultimately constrain the usefulness of a given solution. In this paper we specifically explore the uncertainty, resolution, and regularization of a linearized, continuous approach to the inversion of a full-waveform geoacoustic inverse problem.

Specifically, the problem investigated here is narrowed to the estimation of range-independent P-wave velocity as a function of depth below seafloor, from full-waveform pressure timeseries recorded on a vertical line array (VLA) of hydrophones which spans most of the water depth, or on a horizontal line array (HLA) of hydrophones towed just below the ocean surface (10m deep) by a ship. While a one-dimensional (range independent) ocean bottom is focused on in this paper, the techniques explored here can be expanded to a two- or three-dimensional ocean bottom. Some natural questions to consider are:

1. How do the uncertainty and resolution of the inverted solution change with experiment geometry?
2. How are the uncertainty and resolution affected by noise and modeling error?
3. How does problem nonlinearity affect conclusions drawn from linear tools for uncertainty and resolution of the inverted solution?

Since there is a finite amount of information in the measured data, there is a limit to the resolution of this continuous medium that can be estimated, and this resolution limit can be explored before measurements are taken. In fact, this pre-experiment resolution information can be used to optimize or improve the experimental geometry, formulation of the data, or formulation of the ocean bottom for the greatest resolution of the inverted ocean bottom properties. Experiment design and optimization are not in themselves new, even in the underwater and ocean acoustic communities. For example, Dosso and Wilmut [20] explored information content of a Bayesian geoacoustic inverse problem that had one fluid sediment layer over a fluid basement. Their work analyzed improvements in the marginal posterior probability densities of properties in those layers as a function of experiment geometry, frequencies, and other such factors. Barth and Wunsch [5] optimized geometries of an ocean acoustic tomography experiment by maximizing the smallest unregularized eigenvalue of the linearized problem. Experiment design for similar problems in seismology includes the following references: [13, 12, 11, 58, 60]. There have also been just a few works in the underwater acoustics community in which the results do include the resolution of the solution for continuous inversions of the ocean bottom [43, 54, 6, 53, 50, 51, 52]. However, as far as we have seen, a pre-measurement resolution analysis for the continuous ocean bottom geoacoustic problem, comparing different experiment geometries and array configurations, has not been published. In fact, in 2000 Curtis and Maurer [14] called attention to the issue more broadly within the geophysical inversion community at large, that experiment design is little studied but should be:

“Since 1955 there have been more than 10,000 publications on inversion methods alone, but in the same period only 100 papers on experimental design have appeared in journals. Considering that the acquisition component of an experiment defines what information will be contained in the data, and that no amount of data analysis can compensate for the lack of such information, we suggest that greater effort be made to improve survey planning techniques.”

A typical form of full-waveform problem used in the ocean geoacoustic community is called “matched field inversion” (MFI), which expresses the measured and predicted data as

complex-valued frequency spectra, often with the source spectrum considered unknown and normalized out by modifying an L_2 norm of data misfit into a Bartlett processor [10, 20, 17]. In this work we assume the source spectrum is known, for example via monitor hydrophone placed near the source, allowing us to retain the L_2 norm for data misfit in our problem. We keep the data in the time domain as in examples of linearized full-waveform inversion by Luo, Zhou, and Schuster [42, 41, 74, 75] found in the reflection seismology literature. Note that brief algebra via Parseval’s Theorem shows that the L_2 norm of time-domain data misfit is precisely proportional to the L_2 norm of complex-valued frequency-domain (known-source-spectrum) data misfit, as was used for example in Rajan’s [56, 55] waveform inversion papers mentioned above.

For a problem as nonlinear as full-waveform inversion, regardless of whether a linearized method can home in on a solution or how accurately it can approximate its uncertainties, an important and fundamental caveat remains. The objective function of the problem is quite multi-modal, i.e. it has numerous minima due to cycle-skipping, which results from the oscillating measured and predicted waveforms lining up on the wrong period. As demonstrated by Dosso [20], the deepest minimum is sometimes not even the one that corresponds to the true ocean bottom structure when there is noise on the measured data. For a linearized method one must use a starting model that is close enough to the solution, that is, somewhere within the local minimum of the solution. The full-waveform inversions of Luo, Zhou, and Schuster mentioned above use a travel-time-based (thus weakly nonlinear) “pre-problem” to handle this situation. As further detailed in Section 4.1, our particular problem is at low enough frequencies with narrow enough bandwidth that we may use a heuristic approach to determine that our (quite general) starting model is in the same minimum as the solution.

The upcoming chapters of the thesis shall begin with a definition of the forward problem, then describe the particular inversion method used, and present details specific to solving the waveform geoacoustic inverse problem considered here, all leading up to the use of an inversion-based resolution analysis to aid design and planning of an inversion-based geoacoustic experiment.

Chapter 2

OUR FULL-WAVE GEOACOUSTIC FORWARD PROBLEM

The “forward problem” in this work is the mathematical prediction of seismo-acoustic wave propagation for a particular experiment geometry and source signal, producing predicted acoustic responses at a set of hydrophones given a vector of parameters describing the continuous (or piece-wise continuous) ocean bottom model. The “inverse problem” is the estimation of the ocean bottom model given the noisy, measured acoustic signals at the receivers. This chapter defines the geometry and forms of the model and of the data used in this problem; many of the issues raised here about the modeling limitations are expanded upon later in Section 4.5.

2.1 Experiment geometry

The geometry of the problem has two forms. One is based on a vertical line array (VLA) arrangement of N receivers, at range R from the source and at depths z_0 to z_N , as seen in Fig. 2.1a. The other is based on a towed horizontal line array (HLA) of N receivers, all at depth z_0 , with ranges from R_0 to R_N as represented in Fig. 2.1b. The depths and ranges of the receivers are varied to compare the effect of different geometries on the ability to resolve the bottom properties. In this dissertation the number of hydrophone receivers is $N = 40$ always, although they can be split up between multiple arrays. The VLA receiver depths essentially span the water column, between $z_0 = 20\text{m}$ to $z_N = 176\text{m}$ below ocean surface, with receivers equally spaced within. The HLA receiver ranges (defined as between the source and first receiver in the array) covers $R_0 = 0.1\text{km}$ to $R_0 = 3.0\text{km}$ and lengths between 200m and 1200m. The source depth $z_s = 5\text{m}$ in Chapter 4 and $z_s = 5\text{m}$, 100m, or 195m in Chapter 5. The top 120m of the range-independent ocean bottom is estimated in the VLA problem in Chapter 4, and the top 240m of the range-independent ocean bottom is estimated in the VLA and HLA problems in Chapter 5.

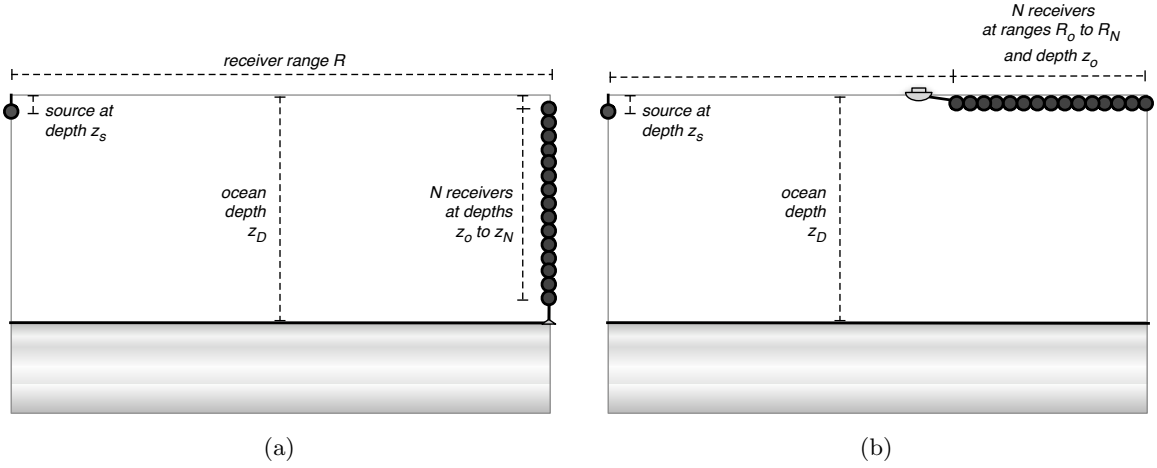


Figure 2.1: Geometries for synthetic problem formulation: (a) vertical line array (VLA) at range R with receivers at depths z_0 to z_N , and (b) towed horizontal line array (HLA) at depth z_0 with receivers at ranges R_0 to R_N , used in synthetic problem formulation. In Chapter 4, $z_s = 5\text{m}$ and $R = 1.0\text{km}$; in Chapter 5, $z_s = 5 - 195\text{m}$ and $R = 0.1 - 3.0\text{km}$. In the VLA problem, $z_0 = 20\text{m}$, $z_N = 176\text{m}$, and $N = 40$ but can be distributed over multiple VLAs. In the HLA problem, array length $R_N - R_0 = 200 - 1200\text{m}$, and $N = 40$. In both problems ocean depth $z_D = 200\text{m}$.

The depth z_D of the ocean in this shallow water problem is 200 meters. The ocean soundspeed profile used for the majority of the example runs in this work is a mildly downward refracting one as seen for example in Mediterranean experiments [20, 17, 18], parameterized by the four points listed in the caption of Figure 2.2.

The wave propagation calculation used in the inversion itself uses a full-waveform elastic method (described further below), but an acoustic raytrace is still a quick and convenient way to qualitatively gauge where the majority of the acoustic energy is going in the problem. We can see for example in Figure 2.2 that the VLA is placed to intersect the bulk of the acoustic energy that interacts with the ocean bottom. If the array were closer or farther away, there would be less information about the bottom in the receptions, and poorer resolution of the bottom structure in the inversion solution. This idea (and its equivalent for other geometry variables) is the focus of the resolution analysis in Chapter 5. Of course, in an inversion of real data, one does not know the true bottom profile, which was used to produce Figure 2.2. But in exploring the synthetic problem or planning a new experiment

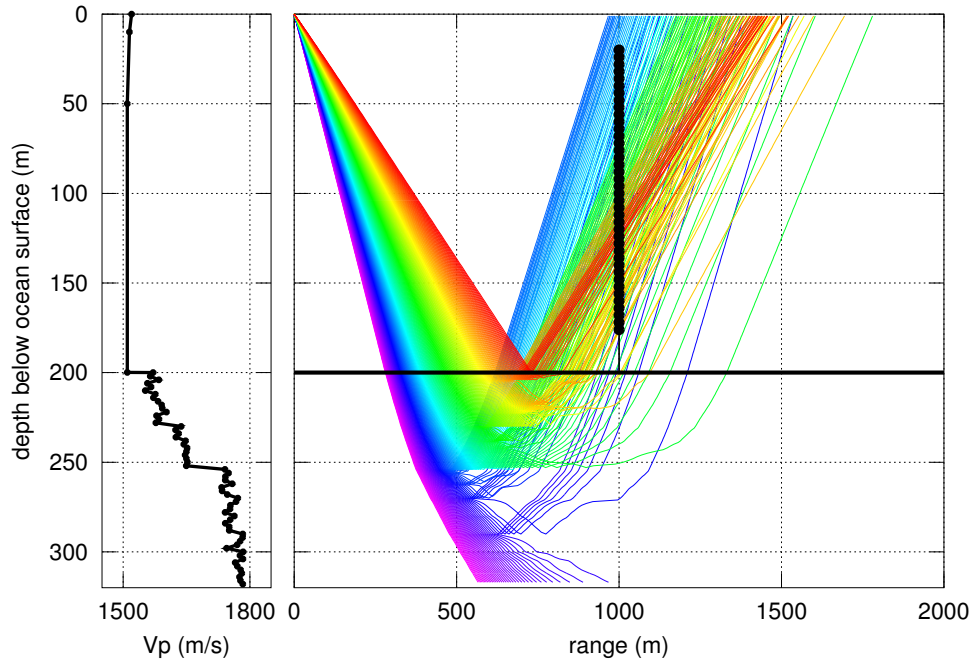


Figure 2.2: “True” P-wave velocity profile and raytrace depiction for the VLA problem explored extensively in Chapter 4; similar raytraces for the geometries in Chapter 5 are shown in that chapter. Rays shown are from $55 - 76^\circ$ with respect to vertically downward. The source is at upper left ($z_s = 5\text{m}$), the heavy black horizontal line at 200m depth represents the seafloor, and the VLA is depicted by the heavy black vertical bar at 1000m range. The soundspeed profile in the water is very mildly downward refracting, parametrized via (and linearly interpolated between) the four depth values: $0\text{m}=1520\text{m/s}$, $10\text{m}=1515\text{m/s}$, $50\text{m}=1510\text{m/s}$, $200\text{m}=1510\text{m/s}$. One sees a range dependence to the intensity of acoustic energy (density of rays) returning from the seafloor due to the refraction shown in the figure; the VLA at 1000m intersects the bulk of the energy; for the data to have information about deepest part of the bottom velocity model (below 290m), an additional VLA at much greater range would be required. Such range dependency of array placement is explored in Chapter 5.

based on previous results in an area, such a raytrace can be qualitatively useful if one bears in mind that it may miss details of the full-wave solution.

2.2 Ocean bottom model

Since this is a synthetically produced example, we begin with a known “true” ocean bottom model, from which we calculate the synthetic data and then add noise of various levels. While in reality one does not know the true ocean bottom, in an exploratory analysis one can learn much about the problem using a known solution and synthetic data before inverting data from a real experiment.

In these synthetic problems one can choose anything for the “true” bottom, and in fact in Chapter 5 there is discussion of variability of the resolution analysis results across differing true bottom models. But as the rest of the dissertation up to that point is more focused on the various details and methods in the inversion and analysis of uncertainty and resolution, the same recurring true bottom model is chosen for that material so that the reader may compare results back and forth across chapters and sections. This recurring ocean bottom P-wave velocity model focused on in this work is the one seen in the ray trace diagram in Fig. 2.2. Its choice was somewhat ad-hoc but specifically chosen to explore three points: 1.) the structure of the profile has a finer scale of roughness than the inversion is expected to resolve due to the limited source wavelength and geometry; 2.) there is both a smaller and a larger discontinuity in the profile (at about 28m and 52m depth below seafloor, respectively) which the inversion is expected to resolve but which should cause strong effects on the uncertainty and resolution of the inversion result beneath them; and 3.) there is also smooth background structure that is hoped to be resolved between the discontinuities, to differing levels dependent on the amount of noise in the data.

The propagation code (described further in next section) is elastic and requires inputs of density, S-wave velocity, and P- and S-wave attenuations in addition to the P-wave velocity profile. But since one of the major motivations of this work is the pre-experiment resolution analysis of Chapter 5 based on P-wave velocity, and also a P-wave velocity solution can provide a useful stepping-stone for subsequent estimations of the other properties, in this work those other properties are simply based on the P-wave velocity using empirical

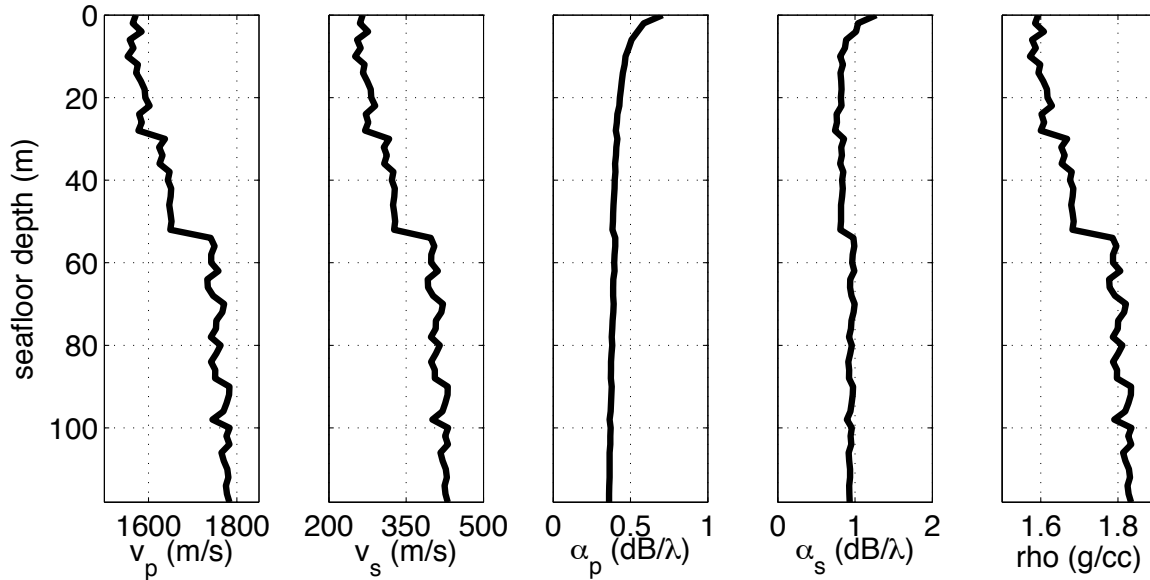


Figure 2.3: P-wave velocity model and associated profiles of S-wave velocity, P- and S-wave attenuations, and density. This is the same P-wave velocity model for the ocean bottom as used in Figure 2.2, and is used extensively in Chapter 4 as the “true” model of the synthetic inversions.

regression relationships. The regressions used are those of Hamilton [28, 29] for a sand-silt bottom, and the resulting profiles for those quantities corresponding to the P-wave velocity profile in Fig. 2.2 are shown in Fig. 2.3. It is acknowledged that the use of these particular regression relations additionally constrain the bottom model to remain within the “sand” regime (which still covers the broad range of P-wave velocities seen in this dissertation) [27].

This analysis focuses on the range-independent problem, so that the ocean bottom is considered to be only changing over the depth dimension. However, the same process described in this paper for 1D profiles can in theory be adapted for analyses of two- or three-dimensional ocean bottom models (in practice there may be more work in analyzing the need for additional regularization and so on). When using the 1D inversion code on real data, one must be careful to justify such modeling of horizontal homogeneity, such that the range variation of the actual bottom is within the resolution at which the 1D solution is estimated.

2.3 Acoustic data

In this work, synthetic pressure timeseries are computed using the OASES software package, which computes the full wavefield (not a ray-based approximation) by combining wavenumber integration and “direct global matrix” techniques [63, 64, 34]. Like other wavenumber integration codes, the synthetic pressure timeseries component of OASES takes two main steps. The first computes the Green’s functions describing the response of the medium between source and each receiver in the given geometry. The second step convolves those Green’s functions with the source signal to produce the predicted pressure timeseries at each receiver. That second step allows great flexibility in specifying the form of source signal; the pulse-based source signal in this analysis is a half-period sine wave pulse enveloping a four-cycle sinusoidal carrier of $f_c = 100\text{Hz}$, according to the expression:

$$f(t) = \frac{1}{2} \sin(\omega_c t) (1 - \cos(\frac{1}{4} \omega_c t)), \quad 0 \leq t \leq T = 4/f_c \quad (2.1)$$

At $f_c=100\text{Hz}$ this signal has a frequency range of approximately 50-150Hz, as seen in Fig. 2.4. This limited bandwidth of the source signal means that the Green’s function only needs to be evaluated inside that frequency range, improving computational efficiency.

This work focuses on synthetic data rather than actual real-world data in an experiment. The synthetic data are produced by adding various levels of independent and identically distributed Gaussian noise to the output of a forward problem run, based on the chosen “true” ocean bottom model. Real-world ambient noise from distant shipping (the chief component in this frequency band) has a somewhat more skewed distribution [1], but this is neglected here. As shown in the spectra in Fig. 2.5, the noise levels range from a standard deviation of 0.05 to 0.89, which correspond to a signal-to-noise ratio (SNR) of 28dB to 3dB. The range of these noise levels was based on the wide range of noise seen in real experiments cited in the literature [20, 18, 48, 73]. As pointed out in previous authors’ work, this SNR could reflect not only the explicit noise in the measurements, but also theory error [19].

2.4 Derivatives of the forward problem

The local linearization based inversion method used in this dissertation relies on Jacobian matrices of the problem at a given operating point, or choice of bottom model. The inversion

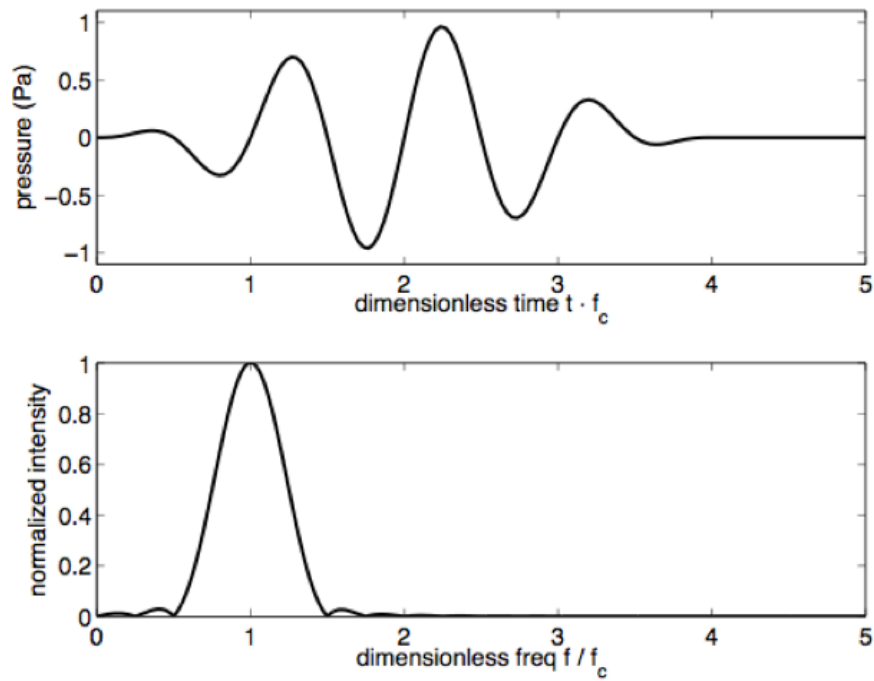


Figure 2.4: Time and frequency representation of source pulse used in the forward problem, one of the pulse-type possibilities in the OASES acoustic propagation software. In this work the center frequency $f_c = 100\text{Hz}$. This representation is mathematically defined in Eqn. 2.1.

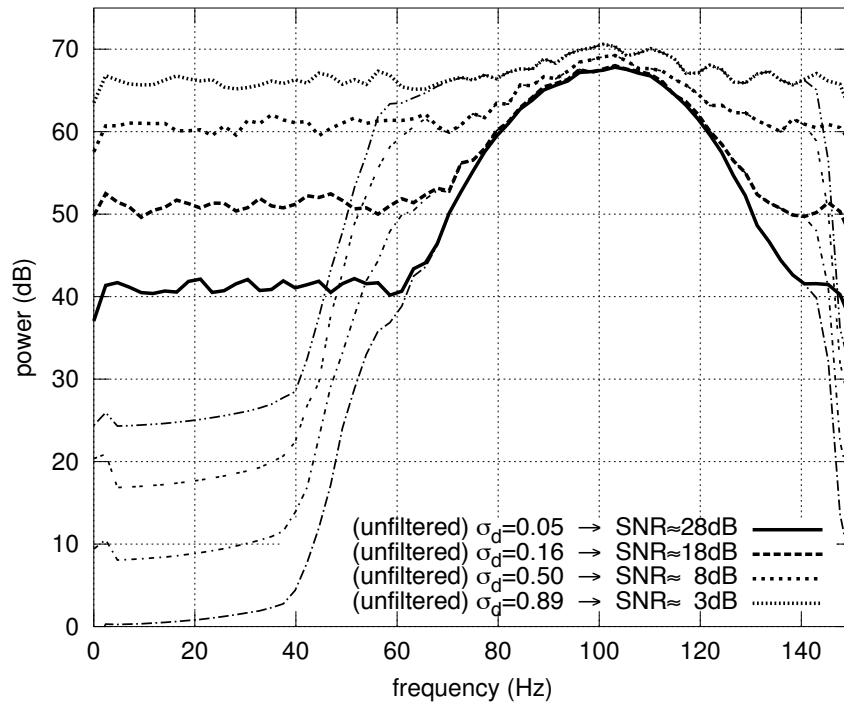


Figure 2.5: Spectra of unfiltered and filtered received signal with various noise levels. These noise levels are based on a range of noise levels in experimental work as cited in the literature (see text). In the interest of improving the signal-to-noise ratio (SNR), the noisy signal is filtered to match the frequency band of the source signal, such that each curve for an unfiltered signal drops down to a much lower noise floor, as seen below 50Hz and a little bit as the signal approaches 150Hz.

iterates from a starting model choice, step by step through the model space to the solution model point, using the local Jacobian matrix to determine the direction and length of the next step. The Jacobian matrix holds the partial derivatives of the predicted data (pressure timeseries at each receiver) with respect to the model parameters (the seafloor physical properties over depth). It is required both for the solution method and for quantifying the uncertainty and resolution of the results.

The waveform inversion as formulated in this dissertation populates the Jacobian matrices G_{ij} with the partial derivatives at points $p(t_i)$ in the acoustic pressure timeseries with respect to the P-wave slowness $u_p(z_j)$ at a series of depths below the seafloor, as defined mathematically in Eqn. (2.2) below. Slowness (inverse velocity) was chosen to represent the velocities for computational efficiency as discussed in Section 4.1.

$$G_{ij} = \partial p(t_i) / \partial u_p(z_j) \quad (2.2)$$

The derivatives are computed for the forward problem by finite forward differences; these are less accurate than finite central differences but require half the forward problem calls, a huge effect in computation time in this problem. Analytical expressions for the Fréchet derivatives of seismo-acoustic forward problems based on the Green's function are in fact available in the literature [72, 71, 70, 41, 15], but for the fully elastic case they are quite involved, so the choice was made in this work to focus energies on the rest of the analysis instead of the numerical implementation of those Fréchet derivatives. With care put to the choice of the finite differences step sizes, the finite differences work quite well in this problem.

The Jacobian matrix of derivatives is a rich source of information about the problem. It contains the first-order sensitivities of the acoustic pressure values at each time, on each receiver, to the bottom P-wave slowness values at each depth. So these derivatives are time- and receiver- and depth-sensitive. Studying the Jacobian matrix contents can provide useful information but can be daunting given their multi-dimensional nature. Figure 2.6 breaks out the derivative information for just one small piece of the VLA problem as an interpretive example – this is from the VLA problem which will be the focus of Chapter 4.

The figure depicts the sensitivities of the acoustic pressures from 0.1-0.175sec on receiver #10 with respect to the P-wave slowness over all the model depths. Figure 2.6a shows the acoustic arrivals over time for each receiver in the top half of the VLA. Only a restricted timespan on receiver #10 is analyzed; this timespan and receiver are highlighted, with a grayscale gradation used to qualitatively relate the earlier and later ends of the 24-point timespan to the derivative profiles in Figure 2.6b. In Figure 2.6b, the left plot shows the model at which this Jacobian matrix was calculated (since it is model dependent). The middle plot shows 24 overlaid depth profiles of $\partial P_k(t_i)/\partial u_p(z)$, meaning the derivatives of acoustic pressure at each of the 24 times with respect to P-wave slowness over the whole depth span. The right plot shows the same information, slightly decimated in depth, this time as timeseries of derivative values at each of 11 model depths. (In that right plot the derivatives at all depths are scaled by a single arbitrary constant to display them in waterfall mode on the model depth axis). Features to note in these derivative plots are as follows.

In the predicted data in 2.6a, the most visible arrivals are the loud reflections (and their multiples on right half) from the seafloor interface. The data is gated “on” at left with the first bottom bounce arrival, and the highlighted portion of the data spans from the beginning of the bottom-surface arrival and reaches almost to the beginning of the fainter bottom-surface-bottom arrival. The arrivals from the deeper bottom structure come in the space between the louder seafloor interface multiples; one might expect to see some sort of depth progression in the derivative profiles in (b) as the time sweeps from the light gray to black end of the highlighted timespan.

While difficult to show without excessive plots, that is exactly what happens in the derivative profiles (center plot in 2.6b). First note there is an oscillatory nature to each individual derivative profile, and in spite of the depth progression of various features in those profiles, they all gradually dwindle at depth since less and less energy returns from deeper depths. At the very bottom of the profile one sees that the derivative amplitude does not in fact quite go to zero, and this causes minor artifacts in some results in Chapter 4 in which the bottom model only goes to 120m depth. But those minor artifacts do not change to overall analysis or conclusions, and for the more involved resolution analysis in Chapter 5 the model depth is increased to 240m.

Meanwhile the depth progression in those derivatives has the lighter gray profiles largest near the surface of the bottom model since those timepoints are in the seafloor interface returns in 2.6a. The bottom portion of the lighter gray derivative profiles is almost zero. As the timepoints sweep out toward darker gray, the “bulb” of stronger derivative amplitudes drops deeper, and one can see in the plot that the black profiles are close to zero in the upper portion of the profiles. Over the course of the sweeping amplitude strengths, more complicated patterns emerge with flares and fluctuations associated with the discontinuities and finer structure in the model.

Lastly, in the right plot of 2.6b, the same derivative information is displayed now along a time axis instead of a depth one. Note these are not the time-derivative of the timeseries highlighted in 2.6a; these are the derivatives of that timeseries with respect to the bottom slowness at the model depths that the derivative timeseries is plotted at. The spatial-temporal patterns in this plot shows two bottom sensitivity arcs that sweep diagonally down through depth and time – one due to the first bottom bounce in (a) which was not itself included in the highlighted data, and the other due to the bottom-surface bounce. Note the small-derivative times at right for shallow depths and at left for deep depths correspond to the small-derivative sections at top and bottom of the derivative profiles in the center plot.

These Jacobian matrices are key pieces of the estimation process laid out in the next chapter.

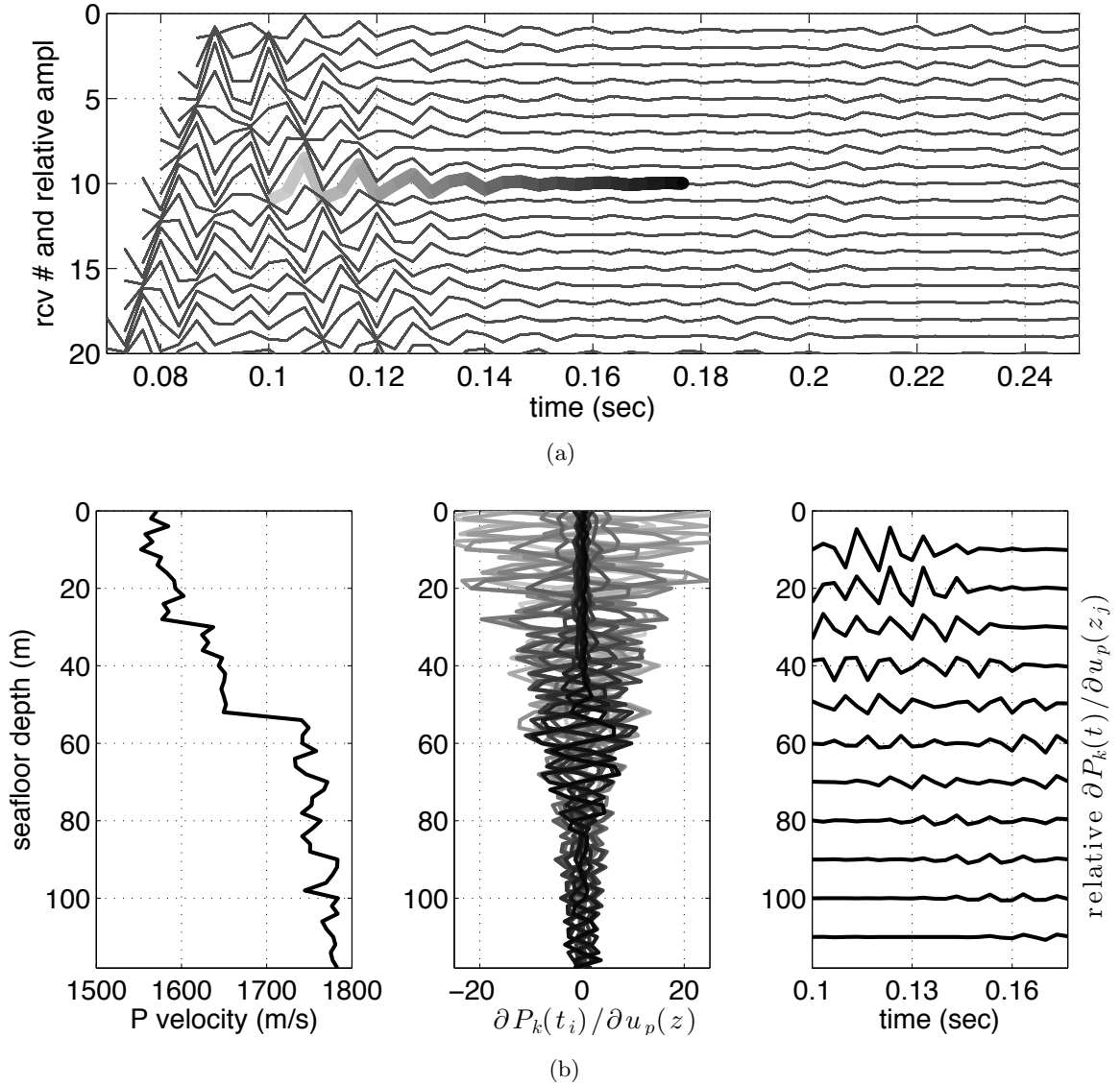


Figure 2.6: A multi-faceted view of a few derivatives in a Jacobian matrix – these are partial derivatives of the acoustic pressures $P_k(t_i)$ at 24 time points from $t = 0.1-0.175$ sec on receiver $k = 10$ with respect to the P-wave slowness $u_p(z)$ over all the model depths. A portion of the predicted data is shown in (a), associated with the “true” bottom model in left plot in (b). The highlighted portion of the timeseries in (a) is on receiver 10 and is the timespan of the derivatives shown in center and right plots in (b). Grayscale in that highlighted data corresponds to grayscale of the 24 derivative profiles in center plot in (b), not meant to be quantitative but just distinguishing ends of the timeseries. The right plot in (b) shows the same derivative information but in a timeseries $P_k(t)$ at 11 model depths z_j .

Chapter 3

MATHEMATICAL DESCRIPTION OF THE INVERSION METHOD

The mathematical formulation of the nonlinear inversions in this dissertation is that of locally-linearized frequentist inversion using 2nd order Tikhonov regularization, as described in more detail in the cited references [3, 46, 49] and reviewed in this chapter for convenience. The statistical framework for the inversion is explained, the iterative linearization method is spelled out in detail, the definition and relevance of the objective function are discussed, and quantifications of uncertainty and resolution of the estimated model solution are defined and discussed.

3.1 Overview

In contrast to the Bayesian estimation framework common in the underwater acoustics community, we solve this problem in the frequentist estimation framework. Unlike the Bayesian framework, the frequentist one is not *per se* a probabilistic approach – the frequentist solution is not a joint probability density function (PDF) of the ocean bottom model parameters. The cost at which the Bayesian framework is able to provide a joint PDF of the model parameters is to require a prior joint PDF of those model parameters, which is often not available, and the so-called “uninformative priors” that are sometimes used in Bayesian estimation can be inappropriate for the high-dimensional model space used in a continuous inverse problem [61].

The frequentist framework on the other hand does not require any prior probabilities (although certain bits of prior information about structure can still be incorporated) at the cost of “smearing out” the solution such that the model parameters are functionals of the continuum solution, limiting the resolution at which the true continuum can be estimated. Stated another way, in the discrete sense the parameters of the ocean bottom cannot be estimated themselves; one can only estimate weighted averages of those parameters.

The Bayesian framework treats the parameters of the ocean bottom as random variables, and estimates their joint PDF; the frequentist framework instead estimates a deterministic but unknown ocean bottom, propagating measurement noise through the problem to produce uncertainties on the functionals or weighted averages, and thus on the estimated continuum. The frequentist approach may be argued to be more or less appropriate than the Bayesian one for a given problem depending how much prior information is available and its form. Either framework could be used in a linearized version for continuous inversion; we use the frequentist one here.

3.2 Frequentist regularized Gauss-Newton inversion

There are multiple methods and frameworks even within frequentist geophysical inversion of a continuous model; we choose discrete inversion using second order Tikhonov regularization in order to obtain the smoothest ocean bottom model from all the models that equally fit the data to within the statistics of the measurement noise. In other words, we take an Occam’s Razor approach and wish to find the model with the fewest number of features that can explain the measured data.

The choice of parameterization of the continuous model is a fine discretization, where “fine” means finer than the resolution at which the inverse problem is solved. One assumes the level of discretization *a priori* (for example based on the wavelength of the acoustic signal used), solves the inverse problem and checks the resolution of the result, and verifies this against the choice of discretization level (redoing the parameterization if necessary). The continuous model is thus represented by a large number of parameters, possibly over-parameterizing the problem. The problem is not simply parameter estimation at this point however, as regularization is required due to the ill-posed nature of the problem to begin with, which is in addition to any rank deficiency caused by the over-parameterization. Frequentist regularization formulates the problem in terms of estimating a set of weighted averages of those parameters; the individual parameters themselves cannot generally be estimated independently, only the averages.

The measured acoustic data is already discrete by nature of being a digitally recorded measurement, and the values from all receivers are concatenated into one long data vector \mathbf{d} .

The measurement noise is estimated and its statistics are entered into the measurement noise covariance matrix (in this work, the pre-filtered covariance matrix was simply of the form $\sigma^2\mathbf{I}$, but the filtering spreads that out to be non-diagonal – actual measurement correlations themselves can be quite difficult to estimate; there has been work in estimating the data covariance along with the model parameters in a Bayesian framework [19]).

In the waveform inversions explored in this dissertation, the relationship between \mathbf{m} and \mathbf{d} is nonlinear and noisy, with the noise modeled as additive via random variable vector $\boldsymbol{\varepsilon}$:

$$\mathbf{d} = \mathbf{f}(\mathbf{m}) + \boldsymbol{\varepsilon}, \quad \boldsymbol{\varepsilon} \sim N(\mathbf{0}, \mathbf{C}_\varepsilon) \quad (3.1)$$

where the $N(\cdot, \cdot)$ notation describes $\boldsymbol{\varepsilon}$ as multivariate normally distributed with mean vector of zero and covariance matrix \mathbf{C}_ε .

If $\mathbf{f}(\mathbf{m})$ is weakly nonlinear enough (which can be a function of how close the starting model is to the solution), \mathbf{m} can be solved for via the iterative Gauss-Newton method by expanding $\mathbf{f}(\mathbf{m})$ in a Taylor series as:

$$\mathbf{f}(\mathbf{m}_{i+1}) = \mathbf{f}(\mathbf{m}_i) + \mathbf{G}(\mathbf{m}_i)\delta\mathbf{m}_i + \dots \quad (3.2)$$

in which the local Jacobian matrix \mathbf{G} is defined as:

$$\mathbf{G}(\mathbf{m}_i) = \frac{\partial \mathbf{f}(\mathbf{m}_i)}{\partial \mathbf{m}}, \quad \text{i.e., } G_{jk} = \frac{\partial f_j}{\partial m_k} \quad (3.3)$$

To first order one can express the residuals $\delta\mathbf{d}_i$ between the measured data and the data predicted from model estimate \mathbf{m}_i as linearly related to the model perturbations $\delta\mathbf{m}_i$ about \mathbf{m}_i . Thus Eq. (3.2) is truncated after the linear term to set:

$$\delta\mathbf{d}_i = \mathbf{f}(\mathbf{m}_{i+1}) - \mathbf{f}(\mathbf{m}_i) \quad (3.4)$$

so that:

$$\delta\mathbf{d}_i = \mathbf{G}(\mathbf{m}_i)\delta\mathbf{m}_i \quad (3.5)$$

The estimate \mathbf{m}_i can be iterated from a starting value \mathbf{m}_0 until it converges, but there are some additional details that allow this to take place.

First, Eq. (3.5) is pre-whitened, or normalized by the covariance of the data noise, in order to obtain a new local Jacobian matrix $\hat{\mathbf{G}}(\mathbf{m}_i)$ and a new vector of data residuals $\delta\hat{\mathbf{d}}$

which are normally distributed as $N(\mathbf{0}, \mathbf{I})$. This step correctly scales the equation for the estimation according to the statistics of the problem. The normalized equation and the substitutions are as follows:

$$\delta \hat{\mathbf{d}}_i = \hat{\mathbf{G}}(\mathbf{m}_i) \delta \mathbf{m}_i \quad (3.6)$$

$$\delta \hat{\mathbf{d}}_i = \mathbf{C}_\varepsilon^{-1/2} \delta \mathbf{d}_i \quad (3.7)$$

$$\hat{\mathbf{G}}(\mathbf{m}_i) = \mathbf{C}_\varepsilon^{-1/2} \mathbf{G}(\mathbf{m}_i) \quad (3.8)$$

At each iteration one would ideally solve for $\delta \mathbf{m}_i$ via the normal equations, if the product $\hat{\mathbf{G}}^T \hat{\mathbf{G}}$ were invertible. But it is not generally invertible, due to the inherent ill-conditioning of the problem (as can be seen in the singular value decomposition of $\hat{\mathbf{G}}$) and possibly rank deficiency as well. The problem must be regularized by either modifying the estimator to compute averages of parameters, as in the frequentist framework, or prior probabilistic information must be added, as in Bayesian framework.

Taking the frequentist approach we regularize the problem with a higher-order Tikhonov formulation [49, 3, 46], by inserting additional rows to the data residuals vector and Jacobian matrix:

$$\begin{bmatrix} \delta \hat{\mathbf{d}}_i \\ -\alpha \mathbf{L} \mathbf{m}_i \end{bmatrix} = \begin{bmatrix} \hat{\mathbf{G}}(\mathbf{m}_i) \\ \alpha \mathbf{L} \end{bmatrix} \delta \mathbf{m}_i \quad (3.9)$$

The scalar tuning parameter α controls the level of regularization and is discussed below. In the second-order Tikhonov formulation used here, the matrix \mathbf{L} is a second-order finite difference operator, which when multiplied by \mathbf{m} approximates the second derivative with respect to \mathbf{m} , providing a constraint on the curvature of \mathbf{m} . So the approach essentially asks, from all the infinite model perturbation solutions that equally fit the data to within the noise, which model perturbation solution do we want? Without more information, we choose the smoothest, i.e. the simplest, solution – the one with the fewest number of features needed to explain the data. In the case of discontinuities (layer boundaries) that are known *a priori*, this information can be incorporated to break the smoothness at those locations by adding a boundary at the respective location in the finite difference operator \mathbf{L} .

To obtain a maximally likely estimate $\widetilde{\delta\mathbf{m}_i}$ of the model perturbation $\delta\mathbf{m}_i$ in Eq. (3.9), that equation is rewritten as:

$$\mathbb{D} = \mathbb{G} \delta\mathbf{m}_i \quad (3.10)$$

and from there one can solve the associated normal equations:

$$\begin{aligned} \widetilde{\delta\mathbf{m}_i} &= (\mathbb{G}^T \mathbb{G})^{-1} \mathbb{G}^T \mathbb{D} \\ &= (\hat{\mathbf{G}}^T \hat{\mathbf{G}} + \alpha^2 \mathbf{L}^T \mathbf{L})^{-1} (\hat{\mathbf{G}}^T \delta \hat{\mathbf{d}}_i - \alpha^2 \mathbf{L}^T \mathbf{L} \mathbf{m}_i) \end{aligned} \quad (3.11)$$

Finally the model estimate is updated such that:

$$\mathbf{m}_{i+1} = \mathbf{m}_i + \widetilde{\delta\mathbf{m}_i} \quad (3.12)$$

and $i = i + 1$. The iterations continue until $\widetilde{\delta\mathbf{m}_i}$ is smaller than a tolerance value based on the precision of the forward problem. “Smaller” is defined in terms of the L_2 norm of the model perturbation profile $\widetilde{\delta\mathbf{m}_i}$. The tolerance is dependent upon the relative accuracy ε_r of the forward problem such that convergence is defined when the following condition is met [3, 24]:

$$\|\widetilde{\delta\mathbf{m}_i}\|_2 < \sqrt{\varepsilon_r} (1 + \|\mathbf{m}_{i+1}\|_2) \quad (3.13)$$

The scalar parameter α in Eqs. (3.9) and (3.11) governs the level of regularization, and thus the tradeoff between variance and resolution of the solution model. It is held constant over the iterations to keep the problem in Gauss-Newton form, but there is some effort in choosing its value. One runs many sequences of inversion iterations, each with a different α value, and choose the optimal α value after analyzing the results of all the sequences. As a guide in choosing a suite of α values to use, we use as a central α_0 value the ratio between the matrix norms of $\hat{\mathbf{G}}$ and \mathbf{L} (i.e. the square root of the ratio of the largest eigenvalues of $\hat{\mathbf{G}}^T \hat{\mathbf{G}}$ and $\mathbf{L}^T \mathbf{L}$):

$$\alpha_0 = \|\hat{\mathbf{G}}\|_2 / \|\mathbf{L}\|_2 \quad (3.14)$$

The other α values are logarithmically spread between two or three orders of magnitude greater than α_0 and less than α_0 . After the many sequences of inversions are run (one for each α), the squared data misfit norm $\|\delta \hat{\mathbf{d}}\|_2^2$ is plotted against the log of the model roughness norm $\|\mathbf{Lm}\|_2$ to form a tradeoff curve, which has a characteristic L-shape. For

this reason this plot is often called the ‘‘L-curve’’. Depending how fast the forward problem runs, one might fit a cubic spline curve to this sequence of points and choose one last new α corresponding to the knee, or location of greatest curvature, on that L-shaped spline curve [30] and rerun the inversion at that α for the final solution. Or for forward problems that take much longer to run, one might simply choose, from among the range of L-curve points computed, the point closest to the knee of the curve. In any case, at this optimal knee point one finds the smallest roughness (smoothest solution) balanced with the smallest data misfit. This knee has been shown [30] to be close to the point at which $\|\delta\hat{\mathbf{d}}\|_2^2 = N - M$. That is, the maximally likely solution for \mathbf{m} corresponds to the mean of the chi-squared-distributed data misfit $\|\delta\hat{\mathbf{d}}\|_2^2$, which equals the number of degrees of freedom (the number of data points N minus the number of model parameters M). In practice however, \mathbf{C}_ε is not well known so the location of the knee is then used as a guide when choosing the tradeoff value.

3.3 Objective function

The problem solved by the Gauss-Newton method in the previous section, with regularized locally-linear subproblems defined by Eq. (3.9), can be rewritten as the following damped least squares problem [3]:

$$\min \left\| \begin{array}{c} \hat{\mathbf{d}} - \hat{\mathbf{G}}(\mathbf{m}) \\ \alpha \mathbf{Lm} \end{array} \right\|_2^2 \quad (3.15)$$

where $\hat{\mathbf{d}}$ and $\hat{\mathbf{G}}(\mathbf{m})$ are the pre-whitened versions of \mathbf{d} and $\mathbf{G}(\mathbf{m})$ (i.e. normalized by the root data noise covariance matrix $\mathbf{C}_\varepsilon^{-1/2}$), completely analogously to Eqs. (3.16) and 3.17:

$$\hat{\mathbf{d}} = \mathbf{C}_\varepsilon^{-1/2} \mathbf{d} \quad (3.16)$$

$$\hat{\mathbf{G}}(\mathbf{m}) = \mathbf{C}_\varepsilon^{-1/2} \mathbf{G}(\mathbf{m}) \quad (3.17)$$

Since $\|\mathbf{x}\|_2^2 = \mathbf{x}^T \mathbf{x}$, the expression in (3.15) is equivalent to

$$\min \left\| \hat{\mathbf{d}} - \hat{\mathbf{G}}(\mathbf{m}) \right\|_2^2 + \alpha^2 \left\| \mathbf{Lm} \right\|_2^2 \quad (3.18)$$

which can be thought of in terms of minimizing quantity \mathcal{L} in the equation

$$\mathcal{L} = \left\| \hat{\mathbf{d}} - \hat{\mathbf{G}}(\mathbf{m}) \right\|_2^2 + \alpha^2 \left\| \mathbf{Lm} \right\|_2^2 \quad (3.19)$$

The quantity \mathcal{L} is called the “objective value”; the function $\mathcal{L}(\mathbf{m})$ is thus the “objective function” and the variable \mathbf{m} is the “objective variable”.

In (3.18) and (4.3), the first term is the norm of the data residuals and the second term is the norm of the model. Given normally-distributed data noise and the pre-whitening in $\hat{\mathbf{d}}$ and $\hat{\mathbf{G}}(\mathbf{m})$ such that the residuals all have unit standard deviations, the first term has a χ^2 distribution. In the L-curve plots described above for analyzing the choice of regularization parameter α to use in the problem, the first term in (3.18) and (4.3) – the data misfit term – is plotted on the y-axis, and the second term – the model roughness term – is plotted on the x-axis. So the optimal choice of α is a balance between this first and second term in $\mathcal{L}(\mathbf{m})$, and that is the point which lands somewhere in the knee of the L shape.

The shape of the objective function surface is precisely proportional to the uncertainty of the estimated model parameters [72], whether the problem is linear with a paraboloidal objective function or the problem is nonlinear with multiple minima dipping in the objective function. In nonlinear problems that use iterative linearization methods such as in this work, the estimation begins from a starting model guess somewhere on this objective function surface and steps to the bottom of the solution minimum. However, with such methods then it is important that the starting model is already somewhere within the correct minimum to begin with, since it will step downhill. The relevance of this issue to the waveform inversion in this work will be discussed in the next chapter, with regards to choosing appropriate starting models.

Lastly, in typical continuous inverse problems the model is highly parameterized, making the objective function a high-dimensional surface. So analyzing objective function issues is not so simple as just looking at a single 2D plot over an appropriate range of the parameters, which would correspond to only two model parameters. One might look at many such 2D plots, slices of the highly dimensional objective function through many pairs of model parameters. However, even that is limited, for it ignores parameter correlations (e.g. in the classic case of a diagonal error ellipsoid, vertical and horizontal slices through the middle of the ellipsoid will blatantly miss the true extent of the error ellipsoid’s length). Ideally one might look at a number of 2D plots that are projections of the high-dimensional function onto planes of two parameters (as for 2D marginal distributions of a high-dimensional

probability density function), but that requires integrating the high-dimensional function over all the other parameters. Whether talking about the 2D slices or the 2D projections, typical geophysical inverse problems have forward problems that take some time to calculate, meaning that not only does the inversion take a potentially long time to run, but that to compute such views into the objective function can quickly become prohibitive. This of course is the reason that inversion methods exist.

3.4 *Uncertainty and resolution*

This section describes calculating first order approximations to the uncertainty and resolution of the inversion solution (the validity and limits of this approximation in waveform inversion is found in the problem-specific discussion in the next chapter). Once the solution model vector has been found, the uncertainty and resolution of that estimate are calculated at that solution point.

There is not enough information in the data to uniquely recover all the individual model parameters themselves – to address this, the regularization remaps the problem to instead estimate linear combinations of the model parameters (in effect linear functionals of the continuous model function). Each parameter of the solution model is a weighted average of parameters in the true model, generally the neighboring parameters in some range, yielding an interpretation of limited resolution of the solution model. The coefficients of the linear combination are given in the *model resolution matrix* \mathbf{R} . The *model covariance matrix* \mathbf{C}_m describes the variability of the parameters of the solution model, that is, that variability of the linear combinations, not of the true model parameters themselves. In other words, in frequentist inversion one can only estimate the uncertainty of an average velocity within a given averaging volume (or given depth span in this 1D case). Note this is in contrast to the Bayesian inversion framework, which gets around this problem at the cost of requiring *a priori* knowledge of the model being estimated.

The resolution of weakly nonlinear problems is often approximated well by the model resolution matrix, which is a linear tool, while the evaluation of resolution of strongly nonlinear problems is still an active area of research. (For example, Snieder [68, 67] extended the traditional Backus and Gilbert method [4, 3] to higher order, yielding higher dimensional

equivalents of resolution matrices. In the Bayesian framework, Mosegaard and Tarantola [47] have shown one way that Markov Chain Monte Carlo sampling of the posterior probabilities of the model parameters can allow for a numerical analysis of nonlinear resolution by studying features in samples of the estimated continuous function.) This issue of weak nonlinearity is of interest when examining results from a linearized method applied to full-waveform inversion – just as a Gaussian approximation of the model uncertainties are only valid within some neighborhood of the solution, the linear description of model resolution is only valid with this neighborhood as well. We shall return to this topic when we examine results of the resolution analysis in Chapter 5.

The model covariance matrix estimated in these problems describes uncertainty in the estimates of those weighted averages, not of the parameters themselves. That is, one estimates a smoothed version of the true model. This complicates the interpretation of the inverse problem solution with respect to the physical reality, but without prior probabilities of the model being estimated, that is the best one can do.

The frequentist model resolution matrix and model covariance matrix are computed as follows. Eq. (3.11) can be expressed in terms of $\hat{\mathbf{G}}^\dagger$, the generalized inverse of $\hat{\mathbf{G}}$, plus a constant term :

$$\widetilde{\delta\mathbf{m}}_i = \hat{\mathbf{G}}^\dagger \delta\hat{\mathbf{d}}_i + \mathbf{c} \quad (3.20)$$

where

$$\hat{\mathbf{G}}^\dagger = (\hat{\mathbf{G}}^T \hat{\mathbf{G}} + \alpha^2 \mathbf{L}^T \mathbf{L})^{-1} \hat{\mathbf{G}}^T \quad (3.21)$$

Once the inversion has reached its solution point however, for the purposes of calculating the first-order covariance and resolution matrices the constant term \mathbf{c} can be neglected, because now $\widetilde{\delta\mathbf{m}}_i \approx 0$ and the problem can be considered as a one-step linear inversion from the final model [26]. At this stage the focus is only on the model perturbation sensitivities to the data, i.e. the contents of $\hat{\mathbf{G}}^\dagger$.

Thus the model covariance matrix \mathbf{C}_m and model resolution matrix \mathbf{R} are computed directly from the generalized inverse $\hat{\mathbf{G}}^\dagger$ in this nonlinear problem using the same expressions as they are in a linear inverse problem, with the exception here that they are approximations

[3] rather than exact representations of the covariance and resolution:

$$\mathbf{C}_m = \hat{\mathbf{G}}^\dagger \hat{\mathbf{G}}^{\dagger T} \quad (3.22)$$

$$\mathbf{R} = \hat{\mathbf{G}}^\dagger \hat{\mathbf{G}} \quad (3.23)$$

The elements of the smoothed version of the true model vector \mathbf{m}_{smooth} , which is the quantity being estimated by the inversion, are linear combinations of the elements of the true model vector \mathbf{m}_{true} . The weights of the linear combinations are contained in the resolution matrix. That is, they are related via:

$$\mathbf{m}_{smooth} = \mathbf{R}\mathbf{m}_{true} \quad (3.24)$$

If \mathbf{R} equals the identity matrix, then $\mathbf{m}_{smooth} = \mathbf{m}_{true}$; in other words the inverse problem has perfect resolution. Usually that is not the case however – typically there is a non-zero region around the diagonal of \mathbf{R} which varies in width at different locations along the diagonal. As the non-zero region around the diagonal spreads out, the value of the diagonal element decreases. If $\mathbf{L} = \mathbf{I}$ (a formulation sometimes described as “zeroth-order Tikhonov regularization” or “ridge regression”), then \mathbf{R} is symmetric, but in the general case including the 2nd-order Tikhonov formulation used in this paper, \mathbf{R} is not symmetric. The off-diagonal elements are not necessarily positive in either case. But in many 2nd-order Tikhonov problems, including the ones in this paper, the resolution matrices still have mostly positive elements and are roughly symmetric in most cases. The columns of \mathbf{R} are the parameters of the *averaging kernels* (or in the case of discrete inversion, they simply are the averaging kernels). The averaging kernel for a given model parameter is the impulse response of the inversion to a delta function in \mathbf{m}_{true} at that parameter. That is, the averaging kernel corresponding to a model parameter is the (limited resolution) inversion of noise-free data that was produced by a delta function.

Note that the geophysical use of the term *model resolution matrix* as used here, which contains the weights of the averages and hence the resolution limits of the inversion, is different from the similar term *resolution matrix* occasionally seen elsewhere in the underwater acoustics literature [62], which is the inverse of the Fisher information matrix. (In the context of this dissertation, the $\hat{\mathbf{G}}^T \hat{\mathbf{G}}$ term in Eq. (3.21) is the Fisher information

matrix.) The conceptual difference between the two cases serves to briefly highlight here the distinction between definitions of resolution in frequentist vs. both Bayesian and unregularized inversions. In the material in this chapter, the frequentist regularization remaps the problem such that it estimates weighted averages of the model parameters because there is not enough information in the data to uniquely recover the parameters themselves. The weights are contained in the geophysical model resolution matrix which is distinct from the model covariance matrix of the weighted averages of parameters; i.e. there can be covariances (correlations) between the weighted model parameters in addition to what the model resolution matrix describes. In contrast, in both Bayesian and unregularized estimations there is no separate matrix of weights – the parameters are estimated directly, and resolution (to first order) is defined there only in terms of the model parameter covariances.

Chapter 4

INVERSION OF THE FULL-WAVE GEOACOUSTIC PROBLEM

While the previous chapter described the general mathematical framework for the inversion method used in this dissertation, this chapter focuses on specific aspects of how that framework is implemented on our geoacoustic inverse problem. It is demonstrated that the waveform geoacoustic inverse problem of interest in this dissertation is amenable to a linearized inversion method used on a continuous (or piece-wise continuous) model. This will open up the problem to convenient tools such as the pre-experiment resolution analysis which is the focus of the following chapter.

Topics in the present chapter include: how slices of the objective function are used to constrain the starting model needed for the inversion; data pre-processing steps which admittedly make little difference in the synthetic inversions but are expected to be important when these methods are applied to real-world experiment data; various example results in inverting the geoacoustic forward problem defined in Chapter 2, including the effects of specifying layer discontinuities of the bottom model in the regularization; and discussion of the effects that errors in the forward problem and in the model have on the inversion.

4.1 Objective function and choices of starting models

The objective function for this geoacoustic inverse problem was defined mathematically in Section 3.3; here it is used to investigate issues of nonlinearity and choice of starting model for the iterative inversion.

There are two aspects of nonlinearity to address, and both can be visualized in terms of the objective function. One is the issue of cycle-skipping that was raised earlier – the concern that the measured and predicted waveforms being matched up have significant periodic components to them. There are many minima on the objective surface which correspond to when those waveforms fall in and out of phase (even if the waveforms do

not match perfectly). If locally-linearized inversion is started from a model that produces predicted data that is more than a half period away from the measured data, then the inversion will converge to the wrong local minimum. So choosing a starting model that keeps the problem in the correct local minimum is one issue.

The other issue is the shape of the objective function even within that local minimum. A linear inverse problem has a paraboloidal objective function; the point at the minimum of the paraboloid is the solution. A nonlinear inversion does not have a paraboloidal objective function, but if one focuses the problem within one local minimum, an iteratively-linearized approach can typically handle objective function shapes that are not too wildly removed from the paraboloid. This means that one wishes to know if the objective function contains undesirable features such as saddle points, discontinuities, and singularities, and to check that it is monotonically decreasing within the local minimum.

In a nonlinear problem such as waveform inversion, it often may not be feasible to definitively answer all these concerns. The forward problem can be slow to run, and must be run a great many times in order to map even small portions of the high-dimensional objective function surface. This heavily limits the number of slices in the objective function, and the resolution of the parameter gridding in those slices, that can be calculated. If features of concern such as saddles or singularities are narrower than that grid or confined to a narrow range of model parameters then the features can be missed in the plots. But between using one's familiarity with the physics of the problem and analysis of those slices of the objective function that can be calculated, one can certainly improve the chance of avoiding pitfalls in the nonlinear inversion.

To help ameliorate the local nonlinearity and improve efficiency it is solved in the model space of P-wave slowness (inverse-velocity) instead of P-wave velocity. In travel-time inversion, the travel-time is a path integral through a slowness field rather than a velocity field. In the one-dimensional case the relationship between travel-time and slowness is linear, the objective function described in Section 3.3 is a paraboloid with its minimum at the solution point, and that solution can be found in just a single step. In contrast, even in that simple one-dimensional case the relationship between travel-time and velocity is not linear. As long as the velocities are constrained to be positive in the inversion, the

poles at zero velocities are avoided and the objective function is monotonically decreasing toward the solution point. The problem is still tractable and solvable, but not in one quick step like the linear slowness case – perhaps by some iterative procedure instead. Figure 4.1 illustrates the difference in form of the velocity and slowness objective functions in just one dimension; the generic shapes seen in this figure will be seen in close approximation in actual objective function slices shortly.

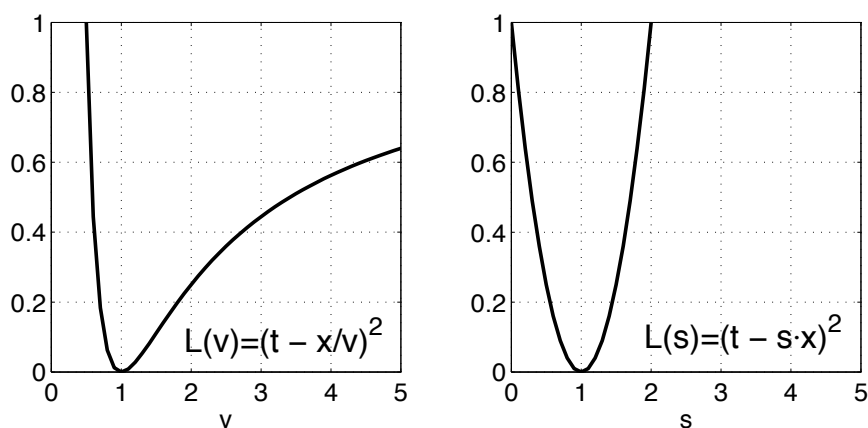


Figure 4.1: Comparison of velocity and slowness forms of least-squares-based objective functions. (In these simple curves $t = 1$ and $x = 1$.) The same general forms can be seen in the actual objective functions plotted in Figure 4.2. The expressions in this figure are linear relationships, but the weakly nonlinear (within solution neighborhood, that is) waveform problem of this chapter has approximately the same shape, with the paraboloidal form in slowness motivating the use of a slowness model space.

Once the source/receiver geometry of the travel-time problem broadens to more than one dimension, the wave energy can refract so that it no longer follows straight paths, and the estimation is no longer linear. But the slowness version of this problem can be expressed as sequence of linear subproblems (as is developed in Section 3.3). As will be seen momentarily in actual objective function slices, the slowness version of the nonlinear problem still looks rather paraboloidal within the local minimum, so the sequence of linear subproblems is quite short. In contrast, the velocity problem, while it still can be solved by the same method, takes many more iterations to converge to the solution.

The discussion so far has been about travel-time inversion, whereas this dissertation concerns waveform inversion, but the same ideas are still relevant. In waveform inversion, the predicted and measured pressure waveforms are matched up via their time-varying pressure values rather than the times of individual phase arrivals. But as long as cycle-skipping is avoided by keeping the predicted and measured waveforms within a half period of each other, the pressure matching ultimately translates to phase perturbations [15, 41, 74], so all the same motivation still applies.

Figure 4.2 shows three slices of the high-dimensional objective function for the first geoacoustic inversion example in this chapter; the same three slices are shown in velocity space (top) and slowness space (bottom) for comparison. The slowness plots cover the same span of velocities as the velocity plots; that is why the origins are not in the middle of the slowness plots. The three slices are for: (a & d) the first and second parameters, i.e. the model at 2m and 4m depth, (b & e) the second and 11th parameters, i.e. the model at 4m and 22m depth, and (c & f) the 20th and 50th parameters, i.e. the model at 40m and 100m depth. The objective function is calculated at the bottom model shown in Figures 2.2, 2.3, and 2.6 in Chapter 2, which will be the bottom model used ground truth for the synthetic problem explored in this chapter (other bottom models are considered in Chapter 5).

These are slices through the solution point, as opposed to projections of the entire N -D objective function onto the plane, so the caveats discussed in Section 3.3 about limited views into the objective function still apply here. Aside from only showing a few slices (they are very expensive to compute), even if all 2D slices were shown one misses the parameter correlations that projections of the whole high-dimensional function onto 2D planes would show. But such projections would require computing the grid of perturbations in all N dimensions; $N = 60$ in these problems and note this N is an exponent when calculating the number of grid cells – infeasible even for a fast forward problem. Still, we take advantage of these few plots of objective function slices to learn what we can about the problem.

Some features to note in Figure 4.2 are the following. The multi-modal (multiple minimum) aspect of the model space appears to be mainly constrained near the surface of the bottom model. In other words, the arrival times of the strongest components in the waveforms are most sensitive to the more surficial values of the model, and it is these

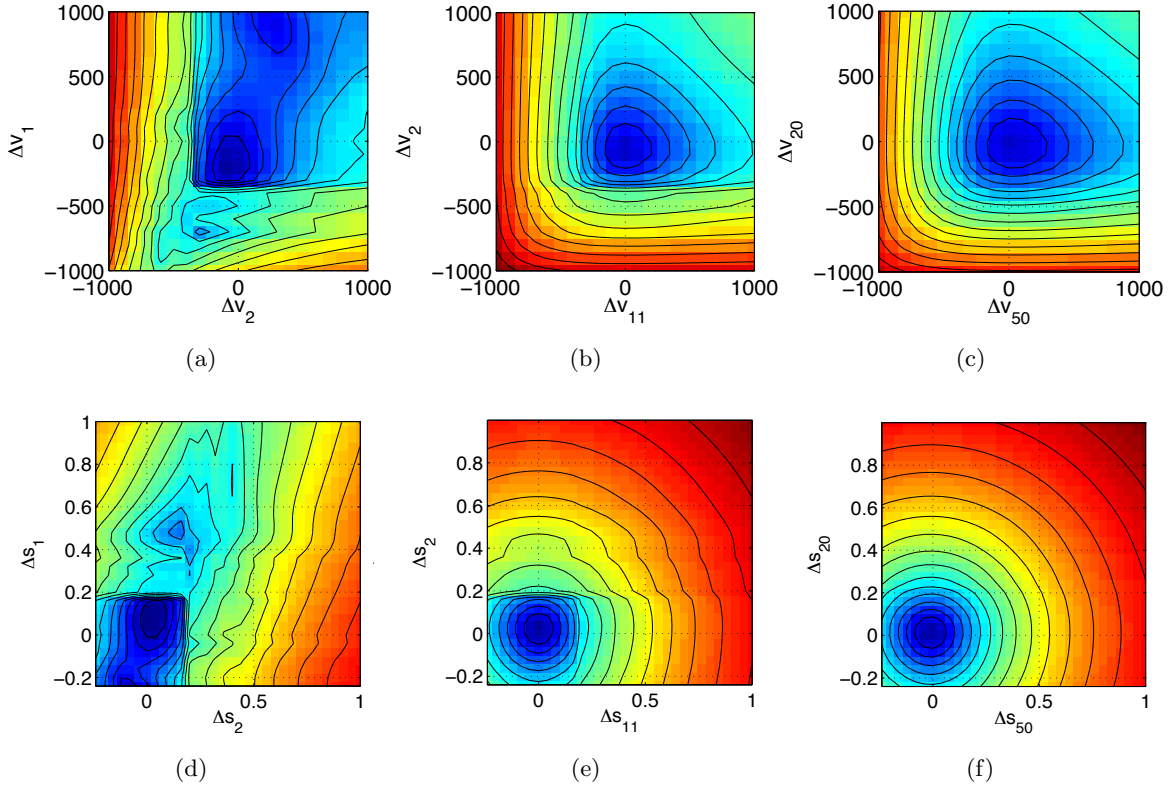


Figure 4.2: Three 2D slices through the high-dimensional geoaoustic objective function in both velocity and slowness perturbations (Δv and Δs respectively) for the first geoaoustic inversion example problem in this chapter. (a & d) the slice at parameters 1 & 2, i.e. model perturbations at 2m and 4m depth, (b & e) slice at parameters 2 & 11, i.e. model perturbations at 4m and 22m depth, and (c & f) slice at parameters 20 & 50, i.e. model perturbations at 40m and 100m depth. The objective function shown here is the quantity in Eqn. (4.3) and is calculated at the bottom model shown in Figure 2.6. Noise is included on the measured data (SNR=8dB) used in the objective function calculation.

portions of the model that can push the arrival times farther than a half period and cause cycle-skipping with the least change in the model values. So the starting model must be closer to the true model at the upper portion than in the deeper portions; still, based on these plots the starting model near-surface velocity only needs to be within $\pm 200 - 300$ m/s of the true model, and the deeper velocities have far more leeway than that. This is due to the low frequency of the waveform with respect to the size of the experimental layout, i.e. sound path lengths. What that means in this problem is that we may get away with

using a somewhat arbitrarily chosen (within these constraints) starting model rather than solving for a starting model in a pre-problem using for example travel-times, as seen in other waveform inversion papers [41, 74]. It is also evident in this figure that the slowness versions of the objective function are much closer to paraboloidal in shape and thus are expected to allow the iterations to converge faster. These objective function slices were computed for the same geoacoustic problem that will be explored in the rest of this chapter.

4.2 *Data pre-processing*

The analyses in this paper focus on synthetic inversions, but they are meant to apply to real-world problems. The following data pre-processing steps do not have a strong effect on the synthetic problem since it is perfectly forward-modeled with perfectly Gaussian noise, but these steps are expected to be important for real-world data which do not match these theoretical ideals, so they are described here from that viewpoint. Noise outside the source band is filtered out to improve signal-to-noise ratio, and reflections from the seafloor interface are downweighted to sensitize the problem to the subbottom response. In cases with a much broader bandwidth source signal, it may also help to deconvolve that source signal from the receptions to reduce the modality of the objective function (number of local minima); then the deconvolved data would approximate the Green's function. But in this problem the source bandwidth is fairly narrow, activating only a narrow band of the Green's function spectrum, so deconvolving the source signal does very little to help.

4.2.1 *Bandpass filtering the noisy data*

As discussed in Sec. 2.3 and depicted in Fig. 2.5, the source signal has a limited bandwidth between 50 and 150 Hz. Noise in frequencies outside this window is easy to filter out and otherwise decreases the signal-to-noise ratio (SNR) of the data. In perfect modeling of the synthetic inverse problem that decreased signal-to-noise ratio has little effect, but in a real experiment where the forward modeling is not perfect and noise is not perfectly Gaussian, one expects this simple step to be important in improving the fit in the inversion.

Using a sixth-order Butterworth filter (the order was somewhat arbitrarily chosen, just high to make the cutoff steep), frequencies outside the source window are removed from the

data. For real experiment data, one would first filter the data and then estimate the standard deviations of its noise, that is, neglecting off-diagonal elements of the data covariance matrix (at this initial stage; although note that estimating these off-diagonal elements has been done in Bayesian-framed geoacoustic problems [19]). For the simple noise statistics and the filter window specified in this paper, these standard deviations of the filtered data are 0.75 of the original independent standard deviations of the synthetic data. The spectra after filtering are seen for the four noise levels in Fig. 2.5.

4.2.2 Down-weighting seafloor reflections in the data

As seen in Fig. 4.3a, by far the strongest component in the data is the reflection from the seafloor. The multiples of these reflections are not as strong as the first reflections, but still stronger than the data content due to sub-bottom structure, which is between the multiples. In a perfectly forward-modeled problem, this does not affect the fit of predicted to measured data as they can match up perfectly for the right choice of bottom model. But a real-world problem is never perfectly forward-modeled – the bottom model may be less than 3D, and there may be certain physics or environmental features neglected or unknown, causing inherent additional error in the predicted data. The predicted data is most sensitive to the geometric errors of the experiment such as for instrument positions or bathymetry (discussed more fully in Section 4.5), and the seafloor reflections are where those errors show up most strongly. Leaving such data as it is emphasizes the misfit between unmodeled data features and modeled ones in the inversion, when one wishes to focus on the true bottom inversion. Down-weighting that portion of the data, without removing it completely, de-emphasizes that region of concern in the estimation process while still allowing it to contribute to the fit. The procedure is described in this section for use in the real-world problem, without being explored further in this thesis which is based on the synthetic problem.

De-emphasizing those seafloor reflections is done by multiplying both the measured and predicted data by a weighting function, contained in diagonal matrix \mathbf{W} which pre-multiplies the data vectors. Conveniently, the coding of the problem is little affected – this augmentation is easily implemented by simply pre- and post-multiplying the inverse

data covariance matrix by the weighting matrix, to produce a new effective data covariance matrix for the problem. The inverse of the effective covariance matrix is what is ultimately used:

$$\hat{\mathbf{C}}_{\varepsilon}^{-1} = \mathbf{W}^{-1}\mathbf{C}_{\varepsilon}^{-1}\mathbf{W}^{-T} \quad (4.1)$$

The down-weighting can be interpreted in two ways – either as specifying a greater noise variance at the reflections, loosening the fit tolerance there, or as evening out the sensitivities of the model parameters to the reflection and non-reflection portions of the data by scaling the derivative matrices. The scaling happens because the inverse effective data covariance matrix is used to scale Jacobian matrices in the estimation, as in Eqs. (3.16) and (3.17).

Two paradigms are considered in the following for how the noise on the real data may be distributed vs. how the statistical results should be calculated. If the noise is independently and identically distributed (i.i.d.) across the data points (as for example in constant ambient noise from distant shipping), which is the case in the synthetic problems in this dissertation, then the weighting described above will cause the effective data noise to become heteroskedastic, to have different variances at different data points. If alternately the noise depends on the magnitude of the received signal, then the original data noise would be heteroskedastic and applying the weighting can remove that heteroskedasticity in the effective data noise.

Data with heteroskedastic noise will not cause the inversion using the Gauss-Newton method described in Chapter 3 to produce a biased model estimate for each given tradeoff parameter α ; that part will still work alright. But it *will* bias the statistics calculated at that estimate (i.e. both the data misfit reported on the tradeoff curve and the covariance matrix of the solution model), because i.i.d. statistics of the data are required for that. So for the case of i.i.d. data noise (as from distant shipping), in a problem in which the down-weighting is applied, the calculations are divided into two steps: 1.) Use the weighted covariance matrix $\hat{\mathbf{C}}_{\varepsilon}^{-1}$ is used in place of the original $\mathbf{C}_{\varepsilon}^{-1}$ for the iterated perturbation calculations of the inversion. 2.) Once the model solution is found, then switch back to the original $\mathbf{C}_{\varepsilon}^{-1}$ for computing the correct statistics in the data misfit, model resolution

matrix, and model covariance matrix. In the alternate case where the noise depends on the magnitude of the received signal, the weighted data covariance matrix is used throughout.

The choice of weights $w(t_i)$, i.e. the elements of the diagonal matrix \mathbf{W} , is somewhat arbitrary, just with the goal of emphasizing the data features due to bottom interactions with respect to data features due to the strong seafloor reflection. The weights used in this work are a normalization of the magnitude of the timeseries data, produced by computing predicted data for the problem corresponding to a halfspace ocean bottom (such that reflections off the seafloor interface are the only bottom interactions in this predicted data – these are the features we wish to de-emphasize). This predicted dataseries is then demodulated via absolute value of the Hilbert transform to produce its envelope $d_{\text{halfspace_demod}}(t_i)$, which is inverted and scaled by a tolerance tol via:

$$w(t_i) = \frac{tol}{d_{\text{halfspace_demod}}(t_i) + tol} \quad (4.2)$$

where tol is chosen to produce weights $w(t_i)$ which range between say 0.05 and unity. When the data is premultiplied by \mathbf{W} , one can see responses to various deeper model structure that were previously hidden by the loud seafloor reflections. An example weighted dataseries is shown in Fig. 4.3.

4.3 Inverting a continuous bottom model with smoothing regularization

In this section results are presented from implementing the inversion method detailed in Chapter 3 on the VLA-based geoacoustic problem with synthetic data, without specifying anything additional about the model structure (such as known discontinuities). In this section the whole model profile is treated as continuous; the next section will deal with handling layer discontinuities in the model.

The 1D bottom profile is discretized in two-meter increments from 0 to 120m. The iterated nonlinear inversion is begun from an arbitrarily chosen, simple linear model m_{init} which goes from 1550 m/s at the surface to 2000 m/s at the deepest depth of 120m.

Four realistic data noise levels were described in Chapter 2; the data used in the example problem in this chapter has the 8dB SNR. That is not the highest level of noise in Chapter 2, but is enough to demonstrate the success of the methods with appreciable noise. In

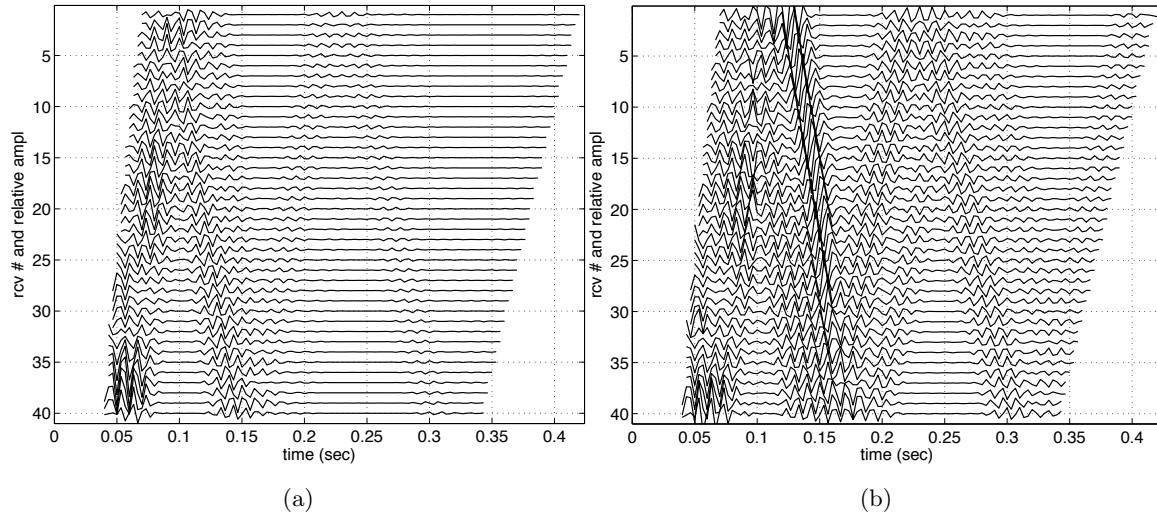


Figure 4.3: The time domain dataset before and after de-weighting of the seafloor interface reflections and multiples: Part (a) shows the data predicted by the solution of the inversion in this chapter, before de-weighting. Timeseries from all 40 hydrophones in the array are shown here in depth order, as compared to every fifth hydrophone shown in Figure 4.12 to view data fit. Part (b) shows the same predicted data after de-weighting (multiplying by the weighting matrix \mathbf{W}). Responses to various deeper model structure are brought out in the signals, most obviously that from the strongest subbottom reflector at 52m below seafloor.

Subsection 4.4.4, effects of all four noise levels on the structure of the inverted bottom model will be shown.

4.3.1 Solving for the solution model

As described in the previous chapter, for each tradeoff parameter value α the inversion is run till convergence, resulting in a collection of model solutions covering a range of model roughness and data misfit. These roughness and misfit values trace out a tradeoff curve as shown in Figure 4.4. Two views of that tradeoff curve are shown in that figure; one (4.4a) with a linear roughness axis to present the classic L-shape of the curve, the other (4.4b) with a logarithmic axis to better separate the points. The x-axis is the model roughness norm, and the y-axis is the data misfit norm, both defined in Chapter 3.

The rougher models have more structure so they fit the noisy data better, with lower data misfit. But some of the structure in the data is noise, which should not be fit. As the bottom model profiles get smoother for points along the L-curve, they converge to a straight line. So while the smoother models have less structure and fit the data worse, they ultimately converge to a maximum data misfit as seen in the plots. At the knee of the L-curve is the appropriate tradeoff where there is the smoothest model that fits the data to within the statistics of the noise. That phrase “to within the statistics of the noise” can be made very specific if the noise is purely Gaussian – the data misfit is the two-norm of pre-whitened Gaussian residuals, as shown for example in Eq. (4.3); the misfit follows a χ^2 distribution with k degrees of freedom, where k is the number of data points minus the number of model parameters. The expected value of the χ_k^2 distributed misfit is that number of degrees of freedom k . The dashed line in the plots in Figure 4.4 is set at the number of degrees of freedom (this line is much easier to see in 4.4b than in 4.4a), and of the runs computed, model #10 was the smoothest one that fit the data to this level; this one is chosen as the solution to the inverse problem.

Typically in an inversion of real data, the character of the noise is not well known, and it also includes modeling inaccuracies, so that simply looking for this expected χ^2 level may not be a good choice, or even an option. Papers in the geoacoustic community have addressed estimating the data variances and covariances as part of the inversion [19, 32]. Exploring the shape of the tradeoff curve in an example run is one of a number of ways that analyzing the problem beforehand like this can be useful – we see that the knee of the tradeoff curve lines up well with the expected χ^2 value in this idealized case, suggesting the problem is programmed correctly and that we might rely on that knee when we cannot rely so much on the expected χ^2 value due to poorly known noise level.

The misfit and roughness of the “true” model (which was used to calculate the synthetic data) are also plotted as the star in Figure 4.4, although one never knows this point in inversions of real-world data. Note the misfit for the data predicted by the true model falls on the degrees-of-freedom (DOF) line, because these residuals are identically the Gaussian noise that was originally added to make the synthetic data. Also notice that the true model is as a rule rougher than what the inversion can justifiably resolve (which is the solution at

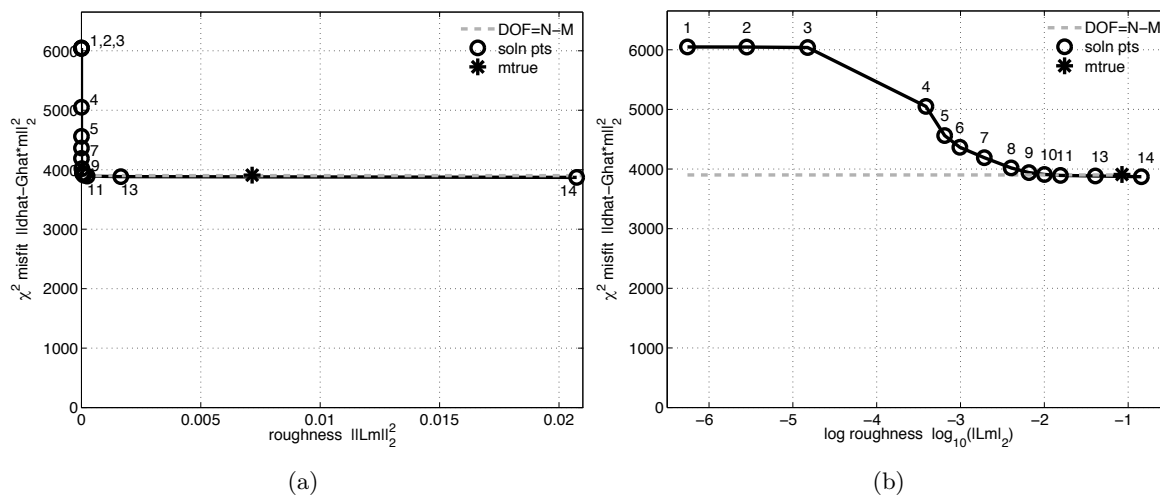


Figure 4.4: Two depictions of the same tradeoff curve for inversions of synthetic data with noise $\sigma_d = 0.50$ using smoothing regularization. In (a) the model roughness norm is presented on a linear axis so that the classic L-shape of the curve is evident; in (b) it has a logarithmic axis and shows a better separation of the points. Note the misfit and roughness of the “true” model (not known in a real experiment) is added onto the plot for comparison, but the inversion generally cannot recover the roughness of the true model. The best solution of this problem was determined to be #10, located in the knee of the L-curve. The numbers on these plots correspond to those in the other figures in this section.

the knee of the L-curve). This will be evident momentarily in the plots of model solutions at each of the points on the L-curve.

In the iteration steps for each of the points on the L-curve, the model perturbations step the problem from the initial model to the solution model, and then the perturbations converge to zero in size as the inversion settles on each answer. The numbering of the curves in Figure 4.5 corresponds to the numbering of the points on the L-curves in Figure 4.4. The pattern to note here is that the smoother the model solution, the more quickly it converges, i.e. more model structure requires more iterations to fit. The curves on the plot can be seen to reach a value close to zero after some number of iterations except for one model, #13, which had not completely converged enough by the time this computation was terminated. Since it was by that time determined via the L-curve to be a rougher solution than the optimal solution of model #10, it was decided to simply not spend the extra calculations

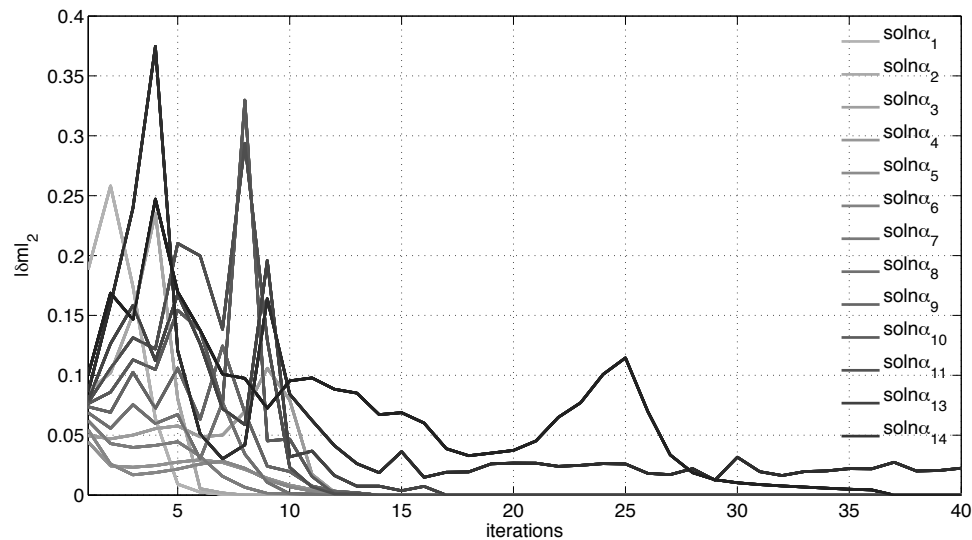


Figure 4.5: Change in norm of model perturbation as a function of iteration number for each point on the Lcurve, to show convergence.

to complete that solution to convergence. A consequence of this early termination shall be seen in the comparison of the model profiles next.

Figure 4.6 presents a selection of the solution models at points on the L-curve in Figure 4.4, covering the range of model roughnesses. The jagged gray models in the background are the same “true” model used to produce the synthetic data for the inversion. This true model is much rougher than most of the inverted models (except for #14, which corresponds with the L-curve points). The smoothest inverted model, #3, is essentially a straight line – it does not fit over the whole true model like a regression fit because the inversion is far more sensitive to the surficial portion of the model; the other inverted models can more broadly fit the shape of the true model because they are not constrained as straight lines. As the models progress toward more roughness, they show the main discontinuity better but still smooth across it – this issue shall be addressed in the next section. Inverted model #13 was the one mentioned above which did not finish converging; note it is the bottom-most, least-sensitive part of the model which has not converged yet as seen in its solution curve. Just as model #3 was extremely smooth, model #14 is extremely rough – these are the endpoints of the L-curve. As discussed a moment ago, model #10 was determined to be the

solution of the inversion, and its point on the L-curve falls in the knee. (Note model #11 is very close to #10 on the L-curve and has a very similar inverted profile.)

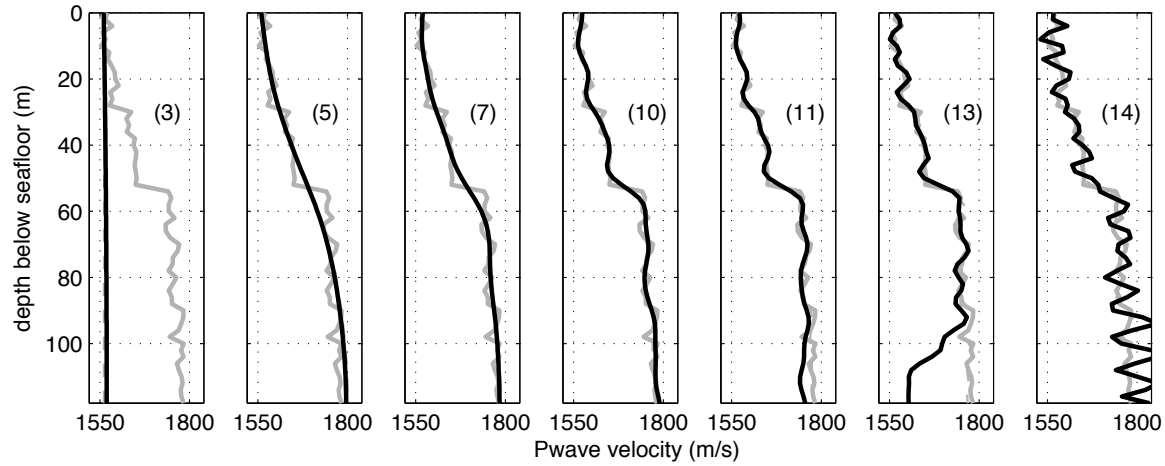


Figure 4.6: A selection of inverted models corresponding to points on the L-curve in Figure 4.4. The jagged gray line in the backgrounds is the “true” model used to produce the synthetic data for the inversion; note it is much rougher than most of the inverted models (except for #14, which also corresponds with the L-curve points). Inverted model #10 in the middle is the one determined to be the solution to the inverse problem (as discussed in text), and is the inverted model that further figures in this section correspond to.

4.3.2 Resolution and uncertainty of the solution model

The variation in resolution of the inverted models in Figure 4.6 was evident, from straight line to something reminiscent of shark teeth. The tool introduced in Section 3.4 allow us to quantify to first order the depth-dependent resolution of each of those models, via the model resolution matrix. The model resolution matrices for three of the models on the L-curve in Figure 4.4, centered about the model (#10) determined to be the solution to the whole inverse problem, are shown in Figure 4.7. The closer these matrices are to an identity matrix, the higher the resolution of the model is. The weights in these matrices impose a correlation between model parameters, typically but not always in the form of a correlation length scale between model values over depth. While the three resolution matrices in Figure 4.7 appear largely symmetric, they are not fully and need not be in 2nd order Tikhonov

regularized problems. The extra shaded bands at the bottom of the α_7 matrix tell that there is commingling of some of the deep portions of the bottom model with the shallower ones when the resolution is that low.

The dark smudge at the bottom right of the α_{10} matrix in Figure 4.7 has a different cause. To model a (possibly piecewise) continuous bottom profile, the profile was finely discretized down to a depth beyond which any returning acoustic energy would be negligible. The diminished derivatives at depth seen in Figure 2.6 in Chapter 2 were part of this determination. Below those many fine “microlayers” specified in the forward problem propagation code was a basement halfspace which is in fact interacting more than expected with the acoustic returns, causing an artifact at the bottom of the resolution matrix there. While the resolution of the inverted models in Figure 4.6 is greater than the discretization in all cases, this artifact shows that the layers should in fact be specified to a greater depth. Since the effect is localized at the bottom of the profile, the rest of the investigations in the present chapter shall continue with the 120m-deep bottom models, but the bottom models in the next chapter regarding the resolution analysis for experiment design shall be finely layered down to 240m instead.

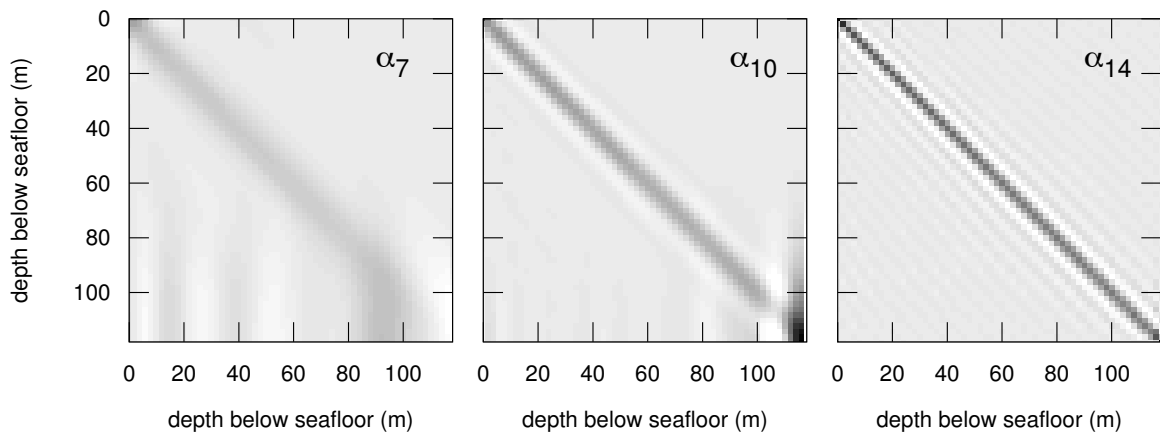


Figure 4.7: Model resolution matrices for the 7th, 10th, and 14th inverted models on the L-curve in Fig. 4.4.

However, it is difficult to elicit much quantitative information out of the color/shading in the matrices of Figure 4.7. The columns of the model resolution matrix yield the “averaging

kernels” showing more quantitatively the depth-dependent resolution of the inverted model, depth by depth. (In the case here in which the parameterization of the continuous model was a fine discretization, the columns of the resolution matrix are the averaging kernels themselves. In the case of other model parameterizations, the columns of the resolution matrix are used in calculating the continuous averaging kernels, as shown for example in Parker [49].) The averaging kernels are a set impulse responses of the inversion (to first order) for each model parameter – if the true model had a spike function at one model depth and the data produced from it was inverted, the solution model would be smeared out around that depth as represented by the corresponding averaging kernel. Figure 4.8 shows averaging kernels for the solution model #10 every 20m in depth. The resolution of the inverted solution is finer very near the seafloor surface, fairly consistent over much of the model depth (comparable to the acoustic wavelength), and degrades at the very bottom of the model where there is minimal sensitivity to the data. It was also discussed extensively in Chapter 3 that in the frequentist inversion does not estimate the full-resolution true model; rather the regularization changes the problem by instead estimating a smoothed version of the true model. The smoothing operator (to first order) is the model resolution matrix itself – see Eqn. (3.24) in Section 3.4 for details. The bottom half of Figure 4.8 shows a comparison between the original true model and the smoothed version of it being estimated by the inversion. These averaging kernels will be used extensively in the resolution analysis in Chapter 5 and are discussed further there.

In addition to limited depth resolution in the inverted model, there is also uncertainty in its velocity values. This is quantified to first order by the model covariance matrix detailed in Section 3.4 in the last chapter. As described there, this model covariance matrix is not the covariance of the model parameters themselves, but of the weighted averages of them (as determined by the weights in the model resolution matrix). Figure 4.9 shows the standard deviations and covariances for the solution, model #10. The standard deviations of the velocity solution as plotted with the solution itself are taken from the diagonal of the covariance matrix on the right. The uncertainty is quite small down to the large discontinuity at 52m. This is in part due to the fact that it is the smoothed version of the true model that is being estimated, and even more due to the data in this synthetic problem

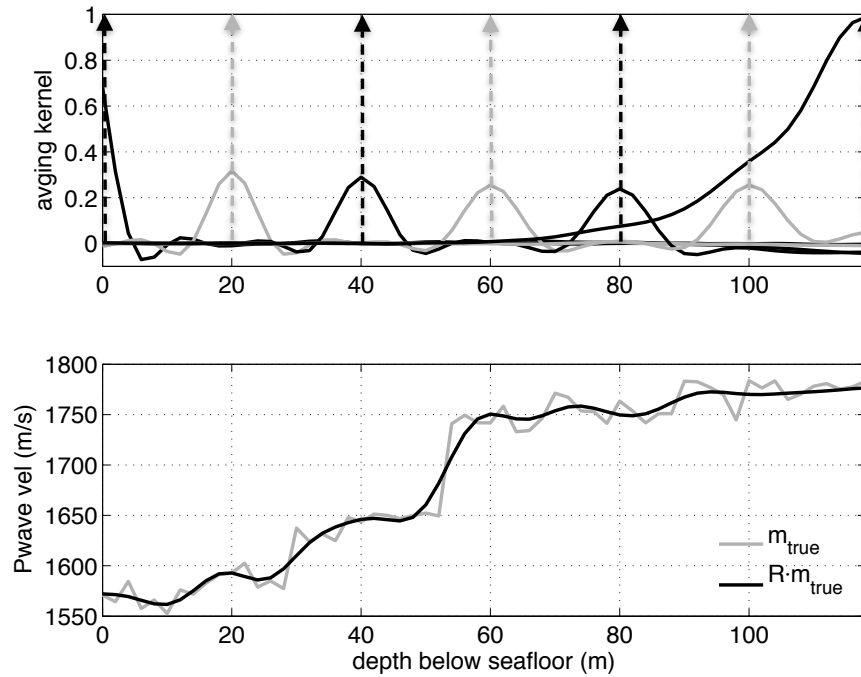


Figure 4.8: Model resolution kernels and smoothed true model for 10th model result on the tradeoff curve in Figure 4.4. These resolution kernels are the impulse responses of the inversion to delta functions in the model at the depths shown by the dashed arrows in (a). The first-order depth resolution of the inversion is the width of the kernel, which in this plot is narrower very near the seafloor surface, consistent over the model depth, and gets large at the very bottom of the model where there is little sensitivity to the data. The same quantity that defines these resolution kernels also defines the relationship between the “true” bottom model and the smoothed version of it (b) that is being estimated in the inversion.

being produced directly from the forward problem. That is, the forward modeling in this problem is perfect, which is of course never the case in real life. Still, the broad correlations at the base of the model as seen in the covariance matrix tell us that the standard deviations at those depths will underestimate the uncertainty.

Figure 4.10 shows the tradeoff between uncertainty and resolution in solutions to this geoaoustic problem. This figure shows both the standard deviations and resolution kernels for five of the inversion solutions in Figure 4.6, i.e. different points on the L-curve. As one sweeps from the smooth end to the rough end of the L-curve (from solution 5 to 13), the resolution improves from coarse to fine (humps get narrower and longer) but the standard

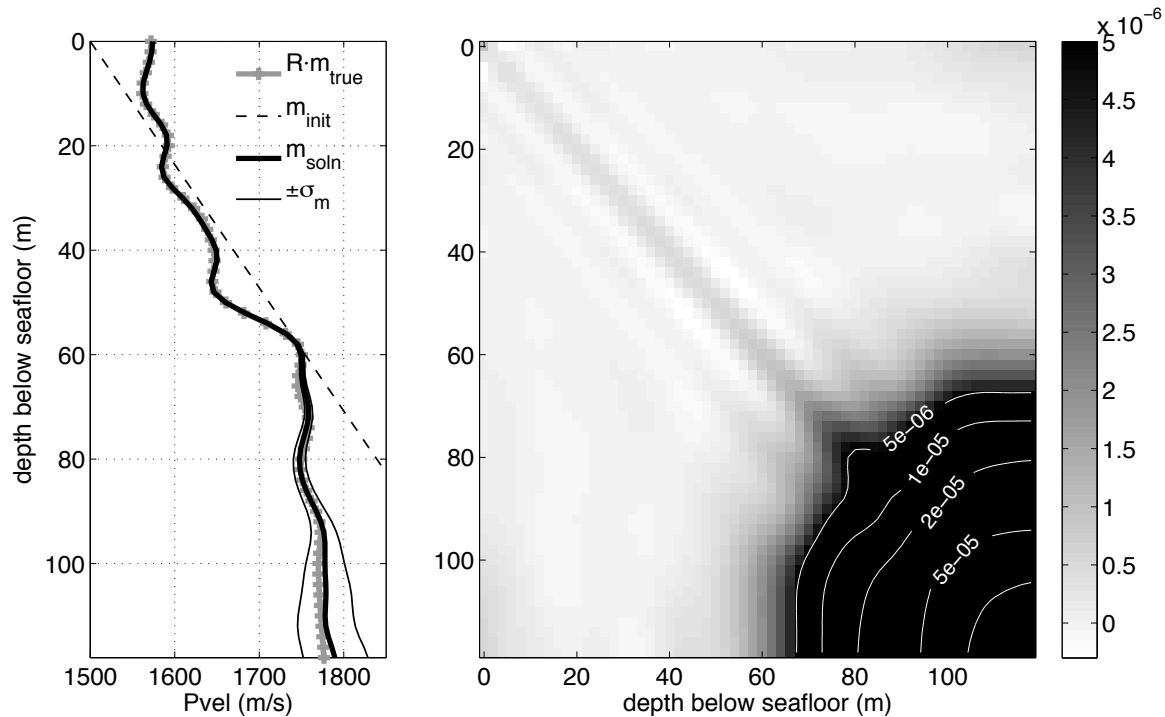


Figure 4.9: Model solution uncertainties to first order for smoothing regularization without specifying layer discontinuities. On left, model solution (thick black line) and standard deviations (thin black lines) for the inverse problem in Section 4.3 – this is inverted model #10 on the L-curve in Figure 4.4. The solution closely follows the smoothed true model (gray line); the dashed line is the initial model. On right, the model covariance matrix for the solution – the standard deviations in the plot at left are taken from the diagonals of the covariance matrix at right. To cover the dynamic range of the covariance matrix, grayscale shading shows the lower-valued features but tops out at $5e-6$, and logarithmically spaced contour lines show the remainder. Note that the standard deviations down where there are broad depth correlations underestimate the velocity uncertainty at those depths. The small uncertainties in the rest of this profile estimate are due to fitting a smoothed true model as well as having a synthetic problem with perfect forward modeling.

deviations also increase, particularly where there is very low sensitivity of the model to the data, at the bottom of the model profile. This is the tradeoff – there is a finite amount of information about the model in the data, and that information simply gets repartitioned between improving the uncertainty and improving the resolution of the model.

Section 4.1 discussed the objective function and its relevance to the choice of starting model for this problem. It was discussed that while a comprehensive analysis of the objective

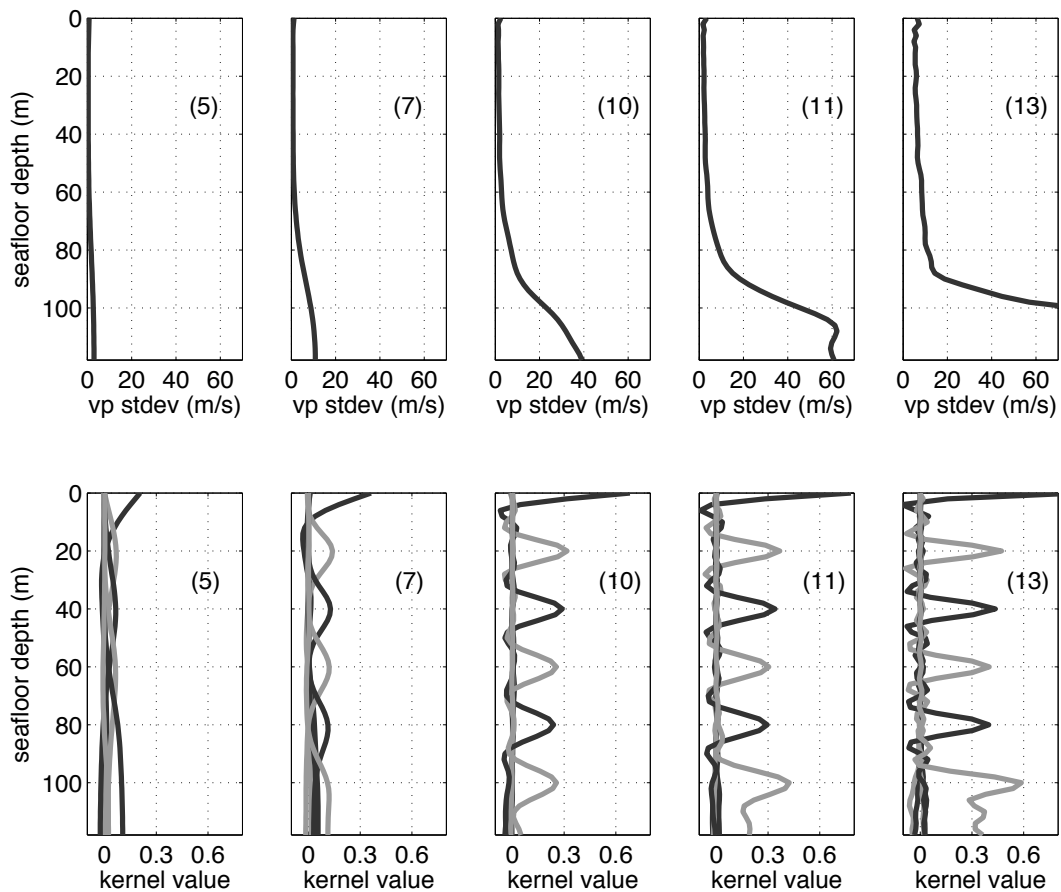


Figure 4.10: Tradeoff between uncertainty and resolution in solutions to the geoaoustic problem studied in this chapter. The numbers in parentheses correspond to the same numbers marking the model solutions of varying roughness in Figure 4.6, i.e. different points on the Lcurve. The top row here shows model solution standard deviations mapped into P-wave velocity (i.e. model space for the inversion is slowness in s/km, but these plots depict $vp_stdev = 1000 / (m_soln - m_stdev) - 1000 / m_soln$ where m_soln is the model solution in s/km and m_stdev is the model solution standard deviation in s/km). The bottom row shows model resolution, rotating the resolution kernels plot of Figure 4.8 by 90 degrees. Note that as resolution improves (humps get narrower and longer), the standard deviations also increase, particularly where there is very low sensitivity of the model to the data.

function is not feasible (if it were there would be no need for the rest of the inversion machinery), the slices calculated suggested this low frequency and narrow band problem would allow broad flexibility in the choice of starting model. Figure 4.11 shows the inversion recalculated for three choices of starting model (the first of which is the one seen previously

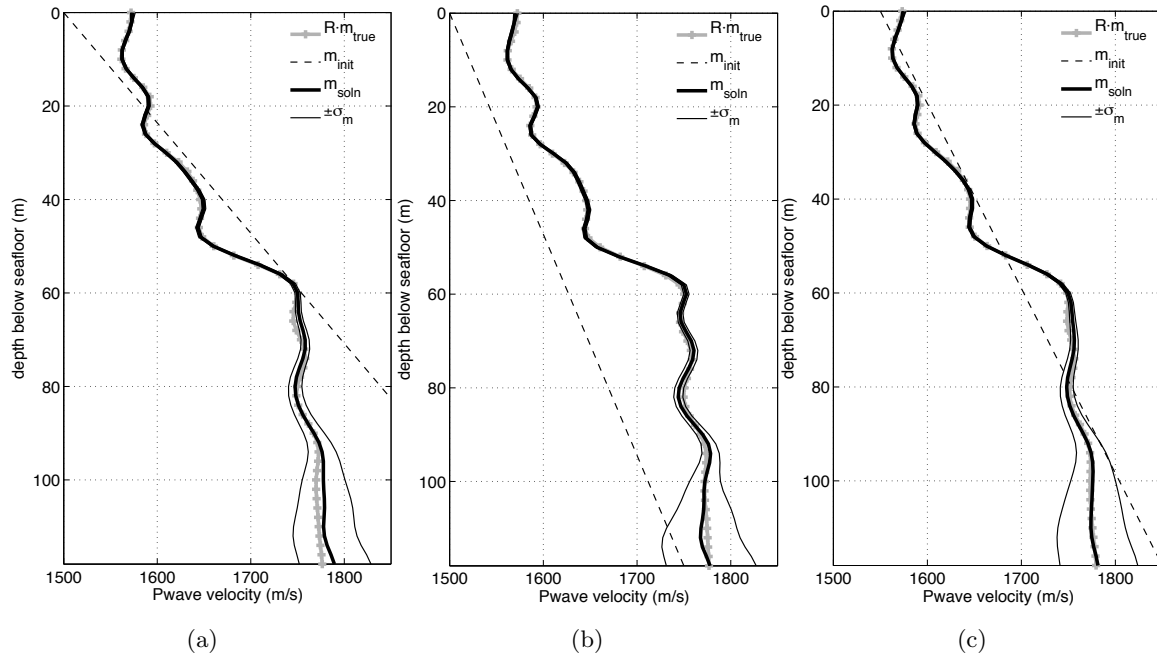


Figure 4.11: Model solutions for the same problem from several different starting models; the dashed line is the starting model in each case, and the solution, standard deviations, and smoothed true models are as in Figure 4.9. The result in (a) is a repeat of that plotted in that Figure.

in Figure 4.9). The three solutions are virtually the same. If one looks closely at that figure one will see the three solutions do appear to vary slightly – this is attributed to the practical limitation that to accommodate the slow-running inversion, a somewhat limited number of points were solved for on the respective L-curves, such that the solution points chosen closest to the knees of the L-curves did not have precisely the same model norm.

The measured and predicted data are shown in Figure 4.12a and their residuals in Figure 4.12b. The superimposed measurements and predictions are virtually indecipherable if all receivers are left in as in Figure 4.3a; so in 4.12a every tenth receiver is shown so that the differences between the two sets of waveforms may be seen. The residuals in 4.12b do include all receivers – the point is to show their normally-distributed nature. That is, there are not obvious mismodeled features of the data that show up in the residuals, as happens for example for the too-smooth models.

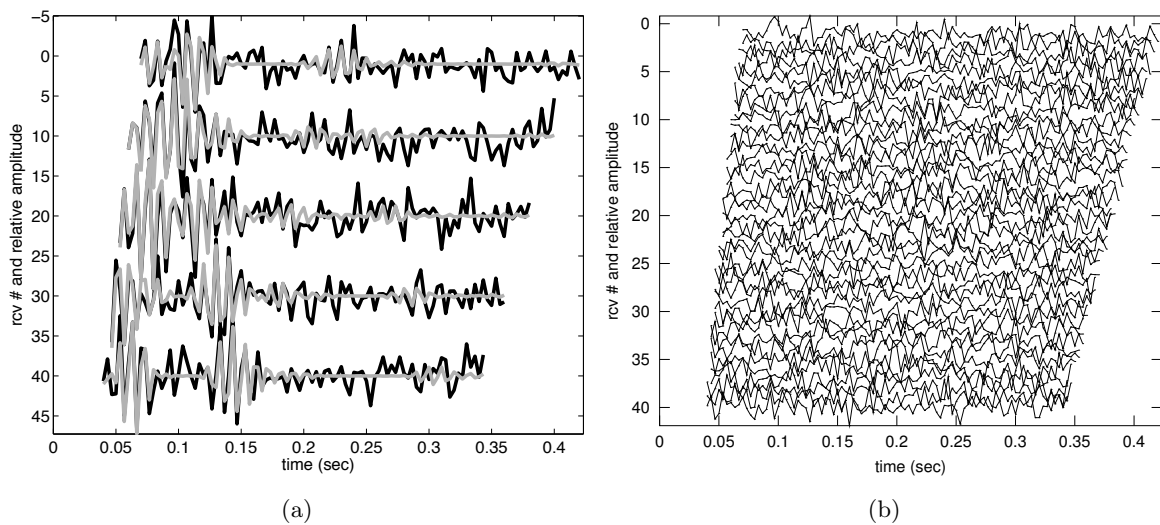


Figure 4.12: (a) Superposition of noisy “measured” (black) data with noise $\sigma=0.50$ (the 8dB SNR signal in the spectra in Fig. 2.5), and predicted (gray) data for solution 10. Only five of the receivers are shown in order to view the timeseries themselves – the receivers from top to bottom are at 20m, 56m, 96m, 136m, & 176m depth in water. (b) Residuals between the measured and predicted data for the same case, but with all 40 receivers shown from 20-176m depth in water. The plot of residuals shows their normally distributed and stationary (over both time and receiver depth) character as produced for this synthetic inverse problem.

4.3.3 Analyzing nonlinear aspects of model resolution and uncertainty via Monte Carlo

The model resolution depicted in Figures 4.7 and 4.8, and the model uncertainty depicted in Figure 4.9, are based on a linear approximation to the nonlinear problem. In order to consider the effects and appropriateness of this approximation, Figure 4.13 shows Monte Carlo results ($N=186$) of the same inverse problem, rerun for N instantiations of random noise on the data. As with the original single solution to this inverse problem, the mean of the Monte Carlo solutions shows little bias with respect to the smoothed true model. Note there is always inherent bias with respect to the original jagged true model due to the nature of the smoothing regularization. The standard deviations of the actual model uncertainty (not linearly approximated) are estimated from the Monte Carlo results with $N = 186$ samples, and they are seen to be consistent with the linear approximation of the model uncertainty at the majority of the Monte Carlo solutions (as demonstrated by the two examples in the figure). Since this is a nonlinear problem, the smoothed true model is actually solution-dependent as well, and this Monte Carlo analysis can also give an idea of how consistent this quantity is which is being estimated. Figure 4.14a shows that the span of smoothed true models ($\mathbf{Rm}_{\text{true}}$) is quite narrow, which is good because this means the various Monte Carlo solutions are all essentially estimating the same thing.

The similarity of the standard deviations between the Monte Carlo and linear approximation of the uncertainty, and the very narrow span of the smoothed true model profiles, suggest that the problem is behaving almost linearly. Figure 4.14b shows averaging kernels for different Monte Carlo runs and can be interpreted in this context as well. The averaging kernels plot in Figure 4.14b (which is like Figure 4.8 turned on its side) is the superposition of the averaging kernels from all 186 Monte Carlo runs of this problem. The kernels down through 80m (only six kernels – six humps – are shown in this plot for clarity) are all virtually on top of each other, meaning the problem is behaving very linearly in that depth span. Below about 80m, the averaging kernels between Monte Carlo runs start to spread out – they do not completely overlap anymore – but it turns out the vast majority of them are still closely bunched together to show an averaging kernel approximately as wide as the others in this plot (about 20m at base). The relatively small number of averaging kernels

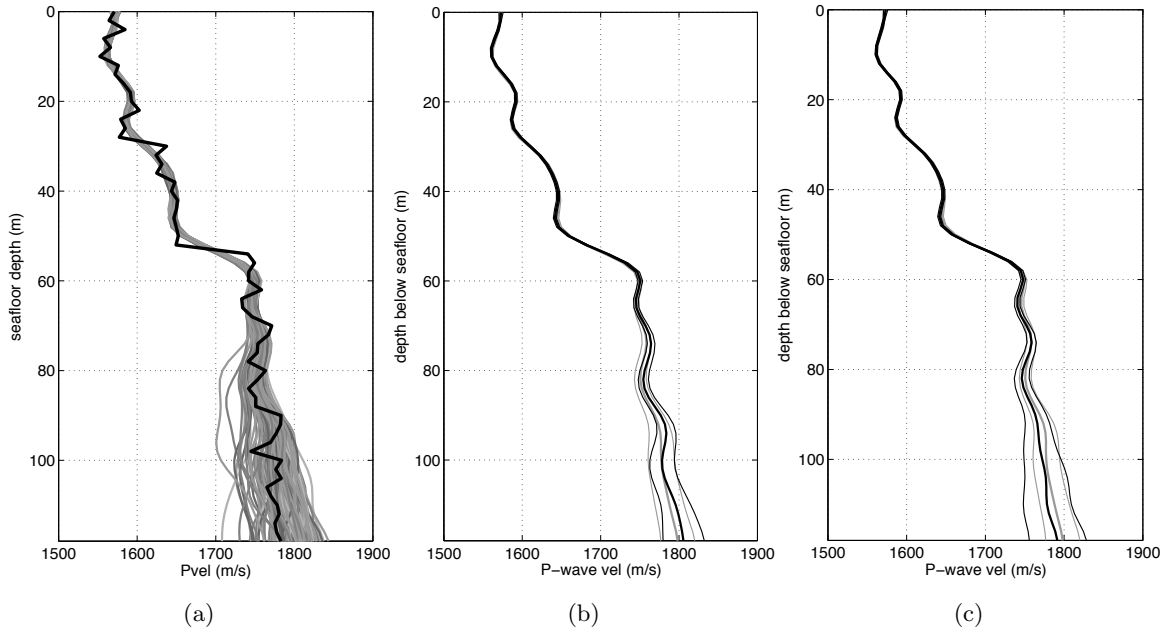


Figure 4.13: Monte Carlo solutions ($N=186$) of the Chapter 4 VLA problem given new random instantiations of data noise. In (a), all Monte Carlo solutions superimposed. While somewhat difficult to see in the figure, a small number of these Monte Carlo solutions have significant low velocity zones (LVZs) in the lowest 20-40m of the profile, which relates to resolution features seen in Figure 4.14b. In (b) and (c), comparisons of mean and standard deviations of MC results (gray) to two of the MC solutions and their linearly estimated standard deviations about those solutions (black), showing approximate agreement between the MC and the linearized standard deviations.

that are far from that bunch (e.g. the kernels > 0.4 at $z > 100\text{m}$ or the kernels < -0.1 near $z = 90\text{m}$) correspond to the Monte Carlo solutions that had low velocity zones at those depths, such that essentially no acoustical energy from those depths was returning to the receivers.

4.4 *Inverting a piece-wise continuous bottom model: specifying layer discontinuities in the inversion*

Whether solved for in a simpler, layered pre-problem, or strongly hinted by a confined steep gradient like the one at 52m depth in Figure 4.9, or known already by other data (e.g. sub-bottom profiler, seismic imaging, cores, etc.), the presence of a discontinuity in the velocity

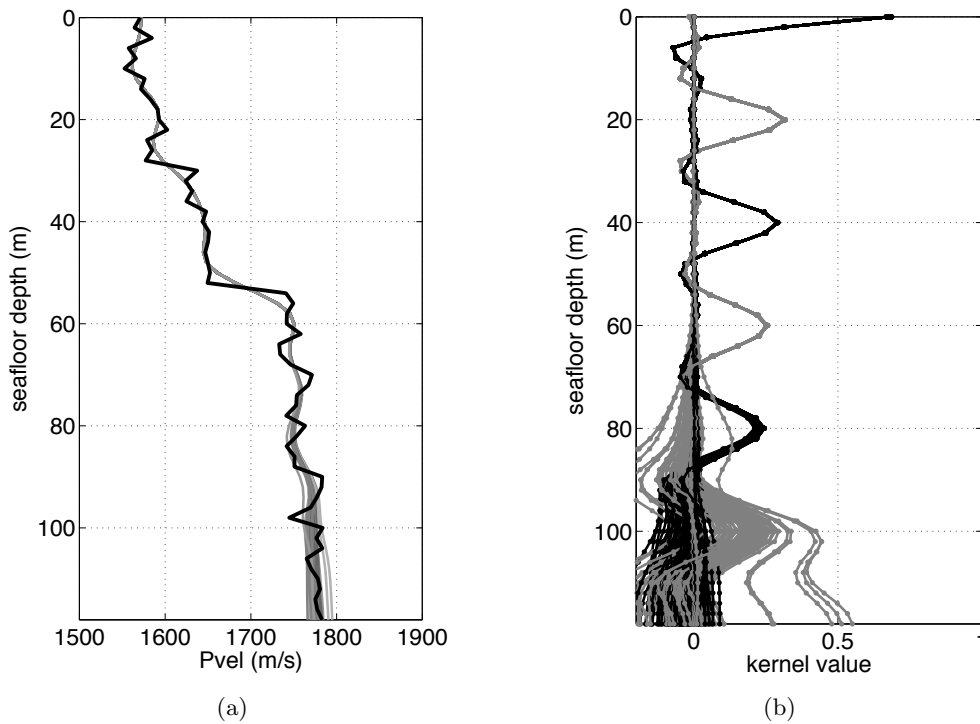


Figure 4.14: Monte Carlo estimates of (a) smoothed true models $\mathbf{Rm}_{\text{true}}$ and (b) averaging kernels for the VLA problem with source depth 5m and range 1.5km, corresponding to the 186 Monte Carlo solutions shown in Figure 4.13. While the averaging kernels do spread out at the bottom of the model in (b), the bulk of those kernels (say for the 100m depth kernel) still cluster around a 20m wide kernel comparable to the kernels at the other depths. The few kernels showing especially poor resolution in (b) (on left around 90m and on right below 100m) correspond to the Monte Carlo solutions with LVZs described in Figure 4.13a.

model can be accounted for in this continuous inversion. By including discontinuities while still inverting for a (piece-wise) continuous bottom model, one allows for the data to show structure potentially varying within seabed layers between the discontinuities. As will be seen, the SNR of the measured data will affect how much of this structure can be resolved. But by including this aspect of the problem one lets the data rather than the scientist's preconceptions determine the structure within the layers of the seabed.

4.4.1 Knowledge of discontinuity locations

Three approaches are summarized here for finding model discontinuity depths. One is via a more general estimation procedure from the one described in this dissertation, such that the layer locations are estimated simultaneously to the rest of the model structure. The two other approaches use the same estimation procedure as this dissertation after first solving a “pre-problem” which estimates either just the properties of a few layers (including thicknesses), or a continuous model from which one might pick out likely discontinuities based on steep gradients. Whichever of the three ways is used, after the discontinuity locations are known then they are added to the problem by modifying the regularization matrix \mathbf{L} whose original form is described in Section 3.2; this modification will be described in the next subsection.

First, that more general estimation procedure uses the same objective function as the one in this dissertation, but with an additional N model parameters (corresponding to N discontinuities) which parameterize the regularization matrix \mathbf{L} . This new parameterization of \mathbf{L} prevents one from using the estimation machinery in Section 3.2 but in theory one could still use some other off-the-shelf optimization program to step from a starting model to the local minimum of the objective function. This objective function looks almost identical to that in Eqn. (4.3) but for the parameterized \mathbf{L} matrix and the augmented version \mathbf{m}' of the model parameter vector which now includes the layer depth(s) $z_1 \dots z_N$:

$$\mathcal{L}(\mathbf{m}') = \left\| \hat{\mathbf{d}} - \hat{\mathbf{G}}(\mathbf{m}') \right\|_2^2 + \alpha^2 \left\| \mathbf{L}(\mathbf{m}') \mathbf{m}' \right\|_2^2, \quad \mathbf{m}' = \left[\mathbf{m}^T \ z_1 \ \dots \ z_N \right]^T \quad (4.3)$$

The problem is still run as many times as there are α s, with α held constant each time and an L-curve produced to gauge the balance between data misfit and model roughness. Note that the parameterized \mathbf{L} matrix would need zeros in the columns corresponding to the $z_1 \dots z_N$ parameters so that those layer depth values do not get smoothed with the rest of the piece-wise continuous profile. Once the solution point is found by the optimizer, the problem can be linearized once more and the uncertainties and resolution information could be computed just as in the approach described in Section 3.4. With these extra few layer depth parameters in the covariance matrix, one may expect to see correlations between these layer depths and the model velocities.

Alternately, one could run a pre-problem to solve for the fully continuous (no discontinuities) model profile and look for depths of steep gradients in that solution to manually pick out candidate discontinuities to specify. The result in the previous section is an example of this – looking at the suite of models of different resolutions in Figure 4.6, one sees the steep, localized model gradient at 52m and perhaps even one at 28m as well in models #10, #11, #13, and #14. From these one could specify model discontinuities at the centers of these gradients. The effects of errors in the chosen discontinuity depths are examined shortly in Subsection 4.4.3. Similarly, if one computes a travel-time-based pre-problem to obtain a starting model for the waveform inversion as mentioned in Section 4.1, steep gradients in that result could suggest model discontinuities to specify in the full waveform inversion.

A more repeatable and objective version of this pre-problem to choose discontinuity depths would be to solve for the average velocities and depths of N layers (so $2N - 1$ parameters) in a parameter estimation. These layered average velocities could be used as the starting model for the continuous inversion, and the discontinuity depths from that estimation can be used in the regularization, again as described in the next section. The average velocities and layer depths can be estimated from the measured data a number of different ways; this parameter estimation problem has been the focus of a large portion of the geoacoustic literature, with some key examples cited in the references [62, 23, 17, 18, 10, 22, 32, 35, 16]. Since this layer parameter estimation problem has been so thoroughly explored in the literature it is not followed further here, instead leaving it as one possible pre-problem to apply on real-world data before running the piece-wise continuous problem described in the present work. In this section about specifying layer discontinuities then, the discontinuity depths are taken as known, either perfectly or approximately, with the resulting effects are seen for each case.

4.4.2 Inversion using discontinuity locations

Discontinuities are specified in the inversion by modifying the regularization matrix \mathbf{L} . Since \mathbf{L} is a second-order finite difference operator as described in Section 3.2, discontinuities

can be allowed for by placing breaks in \mathbf{L} so that the smoothing is not computed across discontinuities.

The distinction between the original and this new \mathbf{L} with the breaks is depicted in Figure 4.15. A gap is left in the second-order finite difference calculation of the model roughness. In the example problem focused on so far, the discontinuities at 28m and 52m depth which were smoothed over with steep gradients in the continuous model in Figure 4.9 are now made explicit in the problem.

Figure 4.16 shows the solution with discontinuities specified in this way for two runs of the same example problem. Two starting models were tried and the same solution was found in each case, to demonstrate that it is the specification of the discontinuities in the regularization, not the starting model, which causes the layered structure of the solution. Upon closely comparing the piece-wise continuous solution in Figure 4.16 to the continuous one in Figure 4.9, the reader may notice that the solution in Figure 4.16 has less variability in the smoothed regions between layers than the one in Figure 4.9. It is smoother overall (if one discounts those discontinuities). This is due to using a model norm that constrains overall roughness for the whole model, and there are strong features in the data caused by those discontinuities in the true model. In order to match those features, the continuous model must be rough enough to produce those steep gradients which mimic the discontinuities. The piece-wise continuous model does not need to contain those steep gradients, and without those there is not the justification under this model norm for retaining the level of roughness elsewhere. This is a function of data noise level – as will be seen shortly in Subsection 4.4.4, with less noise on the data than the 8dB SNR used here, more of that structure is present in the solution.

4.4.3 Effects of error in discontinuity locations

Earlier it was suggested that the discontinuity locations could be solved for in a pre-problem, whether explicitly as parameters or implicitly via looking at strong gradients in continuous model solutions, or chosen based on independent data such as cores. There is error present in those approaches, and here the effect of such errors in the discontinuity locations upon

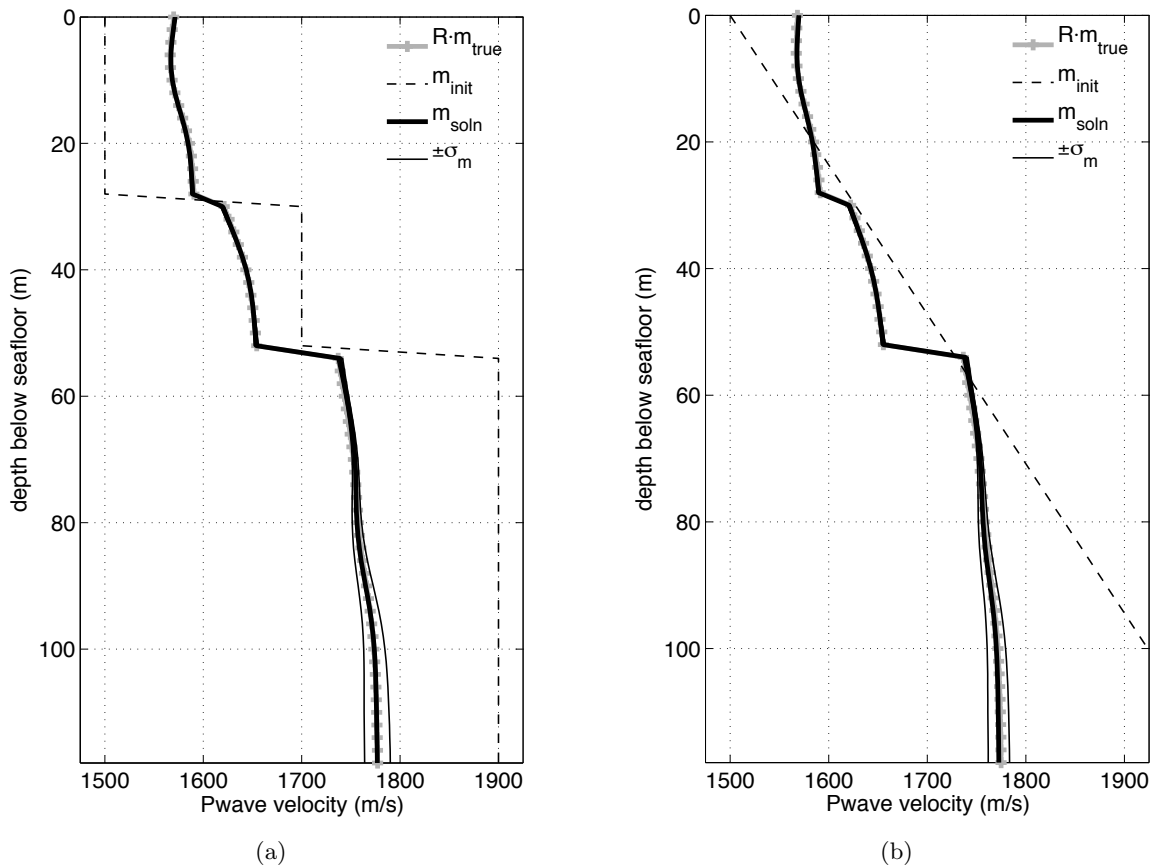


Figure 4.16: Piece-wise continuous inversion result for two different starting models, on the same problem as in earlier sections.

at 18m rather than the true 28m, and at 60m rather than the true 52m). While the problem was seen (e.g. in Figure 4.16) to be not sensitive to choice of starting model (within reason, as discussed in Section 4.1) and the discontinuity information comes instead from the regularization matrix, plotting the layered starting model is a convenient way to display the choice of erroneous discontinuity locations. These figures 4.18a and 4.18b compare the inversion solution to the true model and the erroneous discontinuity locations (via starting model m_{init}). In both cases it is evident the choice of discontinuity location was incorrect, as one can see artifacts such as a smoothed strong gradient next to the 52m discontinuity, and points in the profile without a discontinuity appearing in the solution

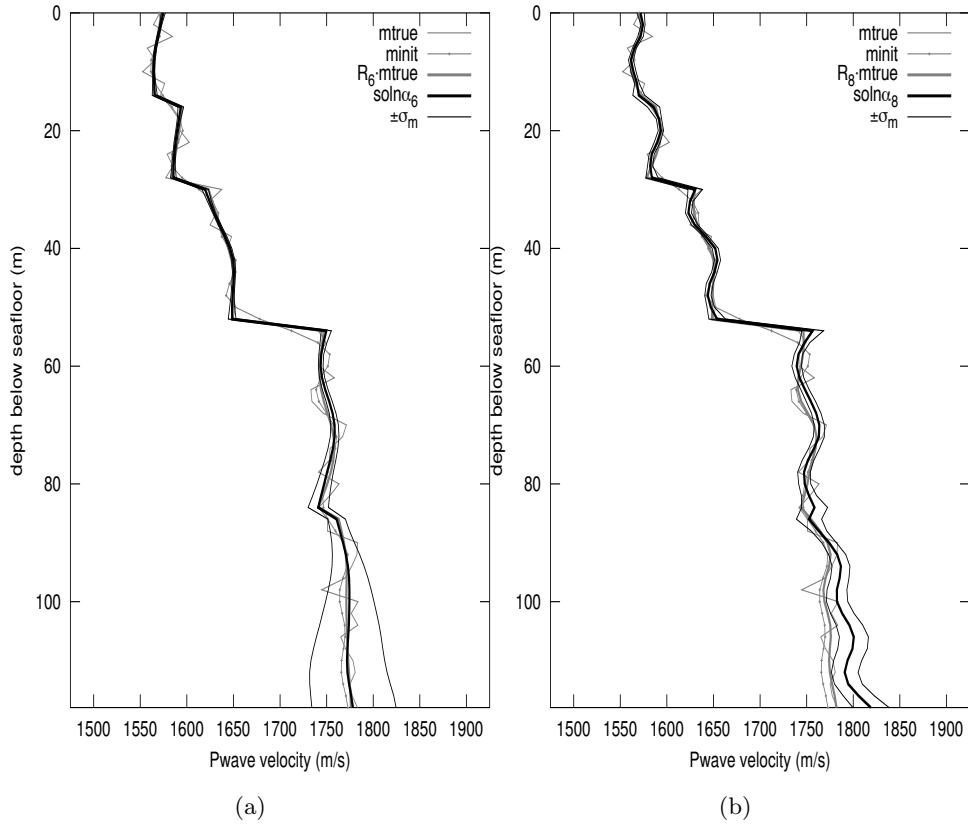


Figure 4.17: Smoother (a) and rougher (b) solutions for four discontinuities specified in the regularization (including the two real ones at 28mbsf and 52mbsf).

near the 28 discontinuity. Once again in each the user has hints in the solution to redo the inversion, perhaps a few times trying different variations in the discontinuity locations – at the correct discontinuity locations the solution jumps to a simpler state matching that in Figures 4.16 and 4.17b.

4.4.4 Effects of data noise on level of structure between discontinuities

It matches intuition that the more noise in the received acoustic signal, i.e. the lower the SNR, the less information content about the model can be retrieved from the data. This can be especially evident in the piece-wise continuous inversion, in which at some point there is enough noise that the smoothly-varying layers between discontinuities simply become

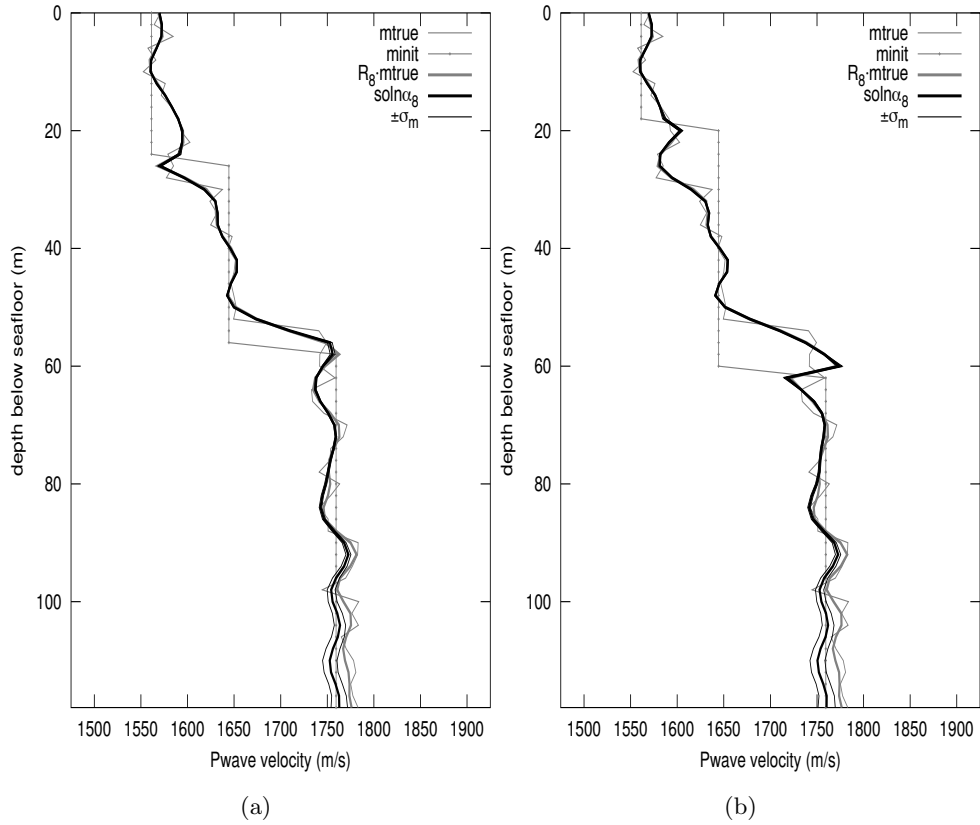


Figure 4.18: Solutions given errors in discontinuity locations supplied to the regularization, discontinuities at 4m (a) and 10m (b) away from the true ones. The true discontinuity locations are seen in the true models m_{true} used to make the data. While the solutions are not sensitive to the choice of starting model this close to the solution, the starting model m_{init} is a convenient way of displaying the choice of erroneous discontinuity locations which were also fed into the regularization.

homogeneous or constant-gradient layers in the inversion solution. In Figure 4.19 the four SNRs discussed in Section 2.3 are compared in synthetic inversion results to see how this decrease in resolution progresses across these noise levels based on real-world experiments.

The results in Figure 4.19 show the inversion solutions (the statistically justified ones at the knees of the L-curves) with increasing noise, with the standard deviations of the model on either side of the solution curve. While difficult to see in these figures, in the background are gray curves representing the smoothed version of the true model (as in Figure 4.16) –

they are difficult to see because the solutions fit the true model so well. One sees that the structure present in the solutions for SNRs of 28dB and 18dB is similar, then there is a noticeable drop-off in structure for the 8dB solution, and essentially only constant gradients in the solution for 3dB SNR.

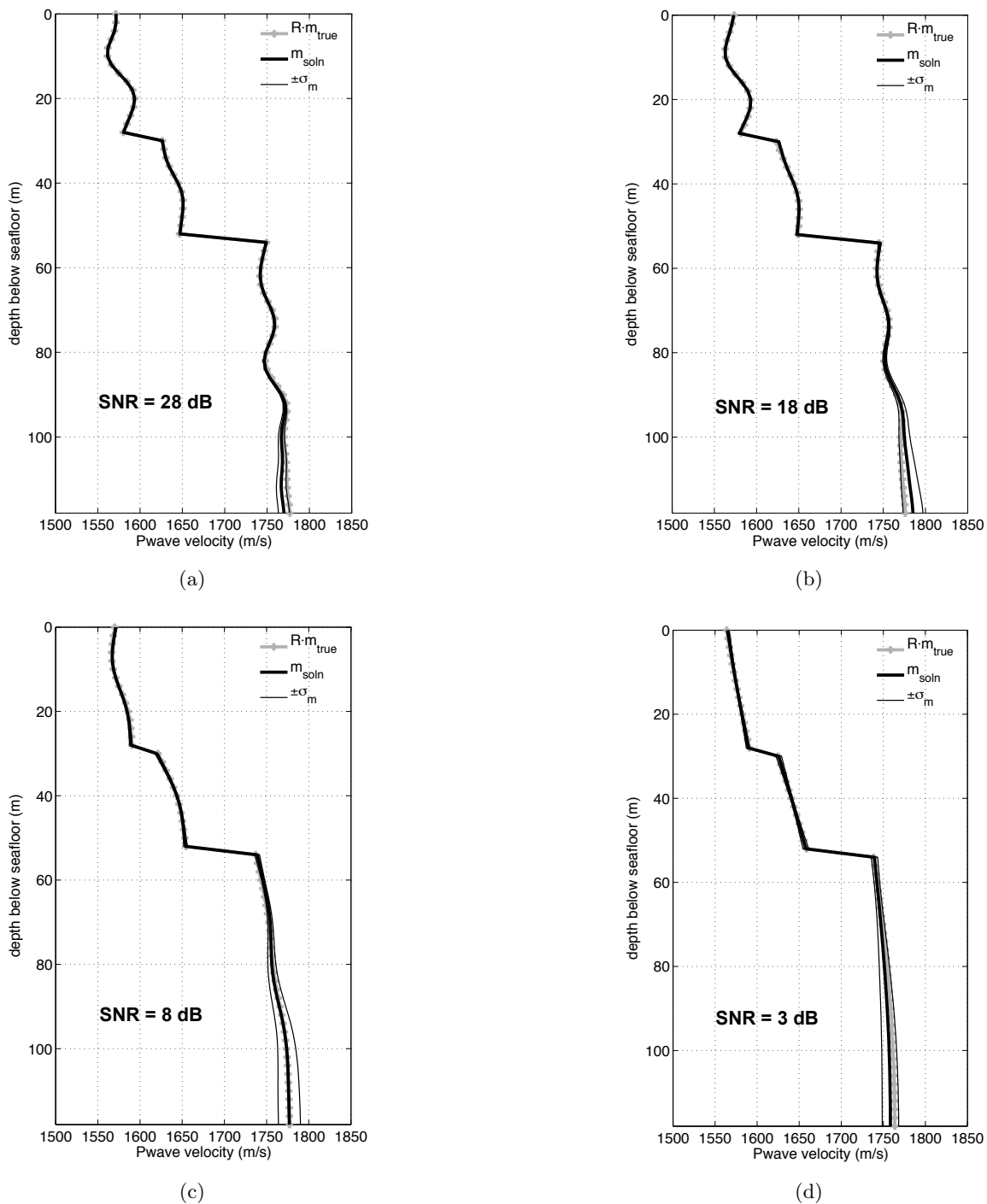


Figure 4.19: Comparing structure in piece-wise continuous inversion solutions over increasing noise. The noise level on the data is described via its SNR, labeled on the plots.

4.5 *Effects of errors in the forward problem and in the model*

An important difference between the synthetic inversion examples earlier in this paper and inversion of real-world data from an experiment is that in these synthetic inversions, the forward modeling was perfect. The statistical form of the data was assumed to be perfectly known and there was zero error in modeling the environment. Of course one generally does not have these luxuries in real experiments.

In the approach described in this dissertation, the bottom P-wave velocity model is inverted from the acoustic data, with a set of empirical regression fits to pin the shear speed, density, and compressional and shear attenuations to the P-wave wave speed, rather than try to estimate those quantities concurrently (as described in Section 2.2).

Additionally the forward problem uses a 1D (range independent) profile description of the ocean and ocean bottom structure, so no bathymetry or range variability of the ocean (such as internal waves or the sea-surface roughness) are included in the modeling; lateral variability of the subfloor structure is prevented. There is no wave propagation considered out of the vertical source-receiver plane. The uncertainties in the positions of the source and receivers, which could sway a bit in the water column, are neglected.

One must consider the criteria under which these various assumptions in the forward problem are valid enough to do the inversion, and their effects on the uncertainties in the results. As long as cycle-skipping is still avoided, with these additional issues in the real-world data the inversion can still find the correct minimum, but the uncertainty of the solution is increased, for the modeling error maps through the problem along with the noise.

The following sections discuss each of the above errors in the forward problem and in the bottom model. Each topic has an entire literature of its own associated with it; none is a minor subject. Here we simply endeavor to summarize the respective issues and reference related work in the literature.

4.5.1 *Data noise vs. modeling error*

There are errors in the data and there are errors in the modeling, i.e. there is a difference between ambient or instrument noise vs. the failure to perfectly model the environment in

the bottom model and forward problem. However, the two issues are notoriously difficult to separate and both contribute errors in the data space that propagate through the inversion into errors in the estimated model. A simple first approach is to combine estimates of the two effects together approximately via summed standard errors (which of course requires such standard errors in the first place). But in reality the data noise and the modeling error do not generally have the same probably densities, are typically not normally distributed, and indeed some components of the modeling error are deterministic rather than random. Others have taken a more rigorous approach to combining the data noise and modeling error in non-continuous geoacoustic problems; for example Dosso et al. [19] demonstrate probabilistic estimation of the data covariance for the two effects combined together, emphasizing the importance of correlations in the data to estimating uncertainties in the estimated model. Considering the data noise entirely separately, McDonald et al. [44] and Andrew et al [1] offer comprehensive analyses and reviews of ambient oceanic noise in the frequency ranges of this paper, largely dominated by shipping noise.

4.5.2 Using empirical fits to relate physical properties

In the forward problem, the profiles of shear velocity, density, and compressional and shear attenuations are produced via Hamilton’s [28, 29] regression fits (for sand-silt) to the compressional velocity profile. These regression fits have uncertainty to them (which were not supplied in their references) – aside from local variations in the sediments contributing to that uncertainty, the data used for the regressions come from many sites around the world. They are used together in that work because there just is not that much of the data. But by looking at the relative sensitivities of this problem to these various parameters, it can be shown that these regression uncertainties do not significantly alter the solution inverted for the compressional wavespeed profile in this problem. This is demonstrated two ways here, one by a singular value decomposition (SVD) analysis, the other via data misfit perturbations from regression fit perturbations.

To calculate the Jacobian matrices calculated at the “true” model (the same one as in the rest of this chapter), the corresponding “true” profiles of the other properties are

produced from the true P-wavespeed profile via the regressions. Then the derivatives of the pressure timeseries at each receiver with respect to these profiles are calculated by finite differences. Five Jacobian matrices are computed – derivatives of the pressure timeseries waveform with respect to profiles of each of the five bottom properties. The Jacobian matrix definitions and largest singular values of these matrices are listed in Table 4.1; the singular values and vectors themselves are plotted in Figure 4.20. These are used in comparisons of the problem’s sensitivity to the respective bottom model variables.

name	definition	w.r.t. variable	largest singular value	expected domain of variable
\mathbf{G}_{u_p}	$G_{u_p}^{ij} = \partial p(t^i) / \partial u_p(z^j)$	P-wave slowness in s/km	1361.0	0.50—0.66
\mathbf{G}_ρ	$G_\rho^{ij} = \partial p(t^i) / \partial \rho(z^j)$	density in g/cc	44.7	1.5—2.0
\mathbf{G}_{α_p}	$G_{\alpha_p}^{ij} = \partial p(t^i) / \partial \alpha_p(z^j)$	P-wave attenuation in dB/ λ	15.4	0—1
\mathbf{G}_{u_s}	$G_{u_s}^{ij} = \partial p(t^i) / \partial u_s(z^j)$	S-wave slowness in s/km	4.5	0.1—1.0
\mathbf{G}_{α_s}	$G_{\alpha_s}^{ij} = \partial p(t^i) / \partial \alpha_s(z^j)$	P-wave attenuation in dB/ λ	0.3	0—2

Table 4.1: Comparison of largest singular values of Jacobian matrices w.r.t. problem parameters, computed at the true ocean bottom P-wave velocity profile used in this chapter’s examples. These are the singular values at index #1 in Figure 4.20a. While the units vary between these quantities, note they are all scaled to order unity so the relative scales of their singular values is still relevant.

As seen in Table 4.1 and Figure 4.20a, the largest singular value of \mathbf{G}_{u_p} is about 30 times larger than that of the next more sensitive Jacobian matrix which is \mathbf{G}_ρ . The largest singular value of \mathbf{G}_{u_p} is about 90 times larger than that of \mathbf{G}_{α_p} , 300 times larger than that of \mathbf{G}_{u_s} , and 4500 times larger than that of \mathbf{G}_{α_s} . The P-wave slowness is by far the most sensitive quantity in the problem, and these results support the idea that the empirical regression fit to obtain the other variables from the P-wave slowness has little effect on the P-wave slowness estimation itself. Relative depth dependence of the sensitivities is seen in the singular vectors corresponding to index #1 in Figure 4.20b, in which most of

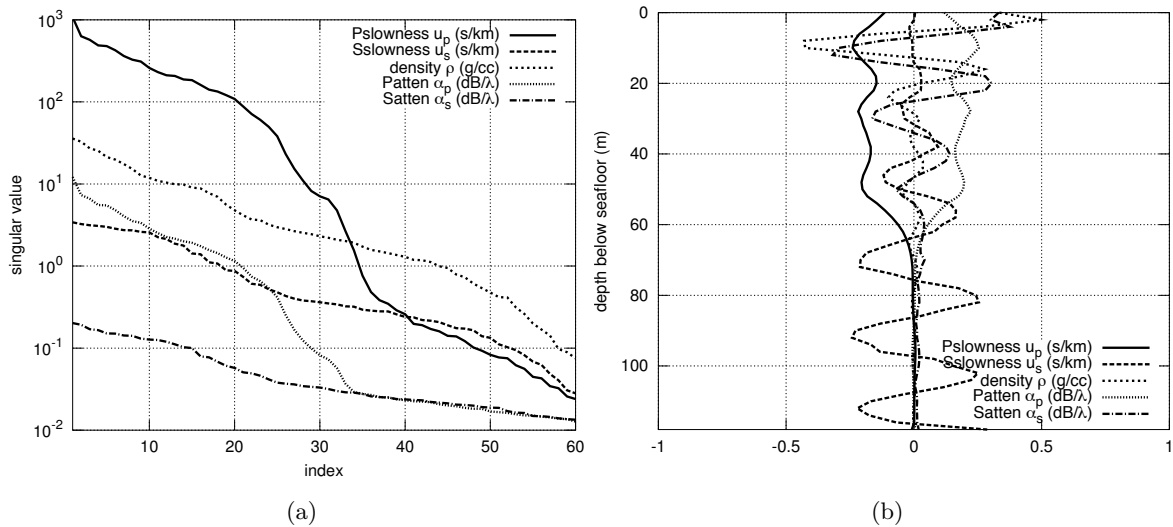


Figure 4.20: Singular values (a) and first singular vectors (for index #1) (b) of the Jacobian matrices of derivatives with respect to P-wave slowness, S-wave slowness, density, and P- and S-wave attenuations. The empirical regression relationships between the quantities is not used in this calculation beyond simply the choice of bottom at which the derivatives were computed (which was the true model for this chapter).

the sensitivities drop off below the large discontinuity at 52m depth. Although the shear velocity sensitivity in that plot does not follow this pattern, its corresponding singular value for that vector is orders of magnitude smaller than that for the P-wave velocity. Note that the low sensitivity to elastic properties in this problem is due to the use of the Hamilton regression which keeps the quantities pinned in the “sand” regime (which still covers a broad range of P-wave velocities) – there is not one regression relationship for all ocean bottom types. In an expanded problem, either all five properties could be estimated simultaneously from the start, or the P-wave velocity solution could provide a refined starting model for the inversion of the five properties.

Lastly, an alternate way of seeing the sensitivity of the inverse problem itself to the uncertainties of the bottom-property regression relationships used is shown in Figure 4.21. Perturbations in the data misfit term of the objective function are plotted as a function of the perturbations in regressions from P-wave velocity to S-wave velocity and to density

which caused them. (Note the model norm term of the objective function is not sensitive to the regression fit used in calculating predicted data, so was left out here; see Section 3.3.) These two plots show that for both shear velocity and density, even $\pm 10\%$ variations from nominal regression values used for those quantities in the forward problem only cause tiny variations in the data misfit value – in the L-curve plots seen earlier in this chapter the data misfit spans values of 1000s.

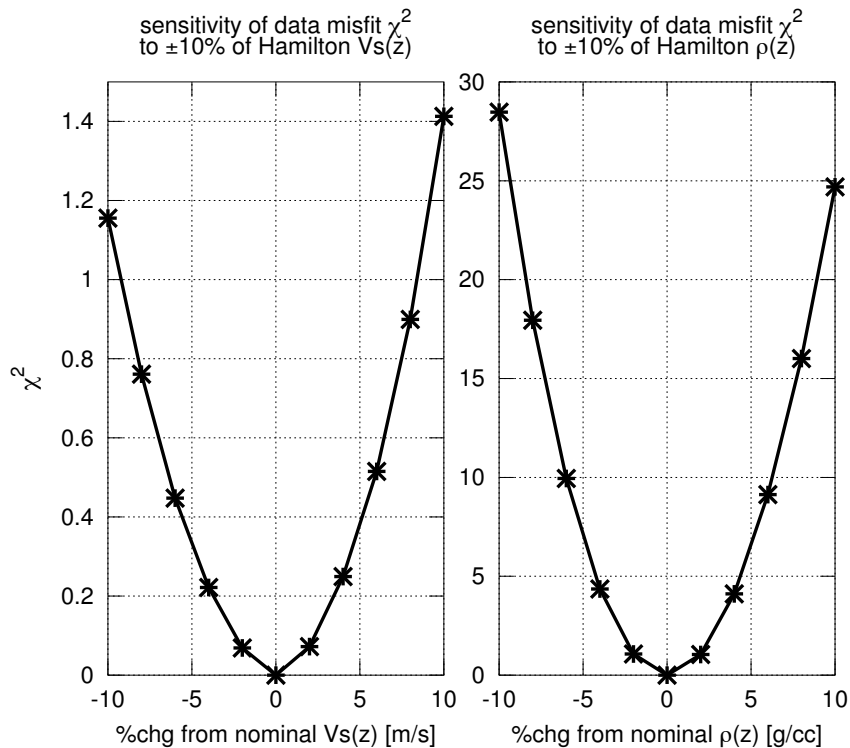


Figure 4.21: Sensitivity of the data misfit χ^2 to perturbations in V_s and ρ with respect to the nominal values given by the Hamilton regressions.

4.5.3 Source and receiver positioning errors

Experiment geometry errors – that is, errors in the measured positioning of experiment components – are strong factors in the waveform prediction error.

In this dissertation source and receiver positions have been assumed to be perfectly known; this may not be a good assumption in all cases. Rajan's [56] waveform inversion paper briefly pointed out the strong sensitivity of his geoacoustic problem to errors in the source and receiver positions. There are two main approaches seen in the literature to dealing with these errors. The errors in the positions of source(s) and receiver(s) may be estimated along with other quantities being estimated, parameterized for example in terms of unknown offsets from nominal positions [20, 17]. This allows one to include the effects of these position uncertainties on the other estimated values; as might be expected, the estimates of the position offsets are typically correlated with the estimates of the other quantities. In modern, longer-range and deeper-ocean tomography and propagation experiments, the requirements in signal timing are such that great effort goes into tracking the (ship-suspended) source and (VLA) receivers using acoustic transponders and high-resolution GPS, and separately solving for their positions as a function of time during the experiment [2]. Such effort may not be necessary in a shallow water experiment because geometrically the suspended/moored instruments simply do not sway nearly so far as in the deep-water case.

A couple quick and very simple manual calculations can give some feel for the magnitude of these errors in this problem. Timing errors less than half a period of the waveform increase the uncertainty in the model solution due to the mismatch, but timing errors greater than half the period break the local linearization based inversion.

The first estimates the travel-time perturbations in the strong early arrivals of the first bottom bounce due to horizontal perturbations in the true source or receiver position. The problem geometry in this chapter has the source at $z_s=5\text{m}$ in an ocean $z_D=200\text{m}$ deep, a first bottom bounce approximately in the middle of the range domain, and the reception $R=1\text{km}$ away on a hydrophone at $z_r=50\text{-}176\text{m}$ depth. The soundspeed profile in this problem is approximately isovelocity at $c=1500\text{m/s}$, so the travel-time perturbation

due to a perturbation ΔR in source-receiver range is:

$$t(r) = \sqrt{(z_D - z_r)^2 + (r - x)^2}/c + \sqrt{(z_D - z_r)^2 + r^2}/c \quad (4.4)$$

$$x = r(z_D - z_s)/(2z_D - z_s - z_r) \quad (4.5)$$

$$\Delta t = t(R) - t(R + \Delta R) \quad (4.6)$$

Plugging in the numbers, one obtains up to a half period (i.e. $\pm 5\text{ms}$) travel-time perturbation for either a receiver range perturbation of $\pm 8\text{m}$ (not strongly dependent on which receiver in the array) with no source perturbation, or simultaneous source and receiver range perturbations up $\pm 4\text{m}$ each.

The second quick calculation estimates the travel-time perturbations in sub-bottom arrivals. The ray parameter p relates the bottom velocity down at a ray turning point to the range ΔX and travel-time ΔT of the ray:

$$p = \frac{\Delta T}{\Delta X} = \frac{\sin i}{v} = \frac{1}{v_{\text{turn}}} \quad (4.7)$$

As seen in e.g. Figures 4.6 and 4.11, the bottom velocities in this problem span from approximately 1550-1800 m/s. Plugging these in for v_{turn} and ΔR in for ΔX , we find a very similar answer as above, that a half-period (5ms) travel-time perturbation corresponds to a perturbation in source-receiver range of 7.75-9m.

4.5.4 *Unmodeled bathymetry*

Mis modeling or neglecting the bathymetry will also have a strong effect and will be most apparent in the arrival times of the strongest features in the waveform, the seafloor interface bounces.

One consideration in the bathymetry effects is as in the previous section about the source and receiver positioning – at what RMS heights of random bathymetry will a 1D assumption cause cycle-skipping? In other words, at what RMS heights will the 1D assumption cause a phase error of half a period of the predicted waveform with respect to the measured one?

Figure 4.22 shows the result of a simple calculation that explores this question for the problem in this chapter. This plot was not created using the forward problem. Since the

ocean soundspeed profile was approximately isovelocity, a constant 1500m/s ocean sound speed and straight rays were used to approximate the travel-times of single-bottom-bounce paths of the random bathymetry (Huygens' principle allows one to simply do that to first order using the bathymetry heights, as opposed to worrying about the local bathymetry angle). This was done for each of 100 random instantiations of bathymetry, each scaled to cover a span of RMS heights; straight paths were computed from the source to the bottom to each of the 40 receivers in the VLA. One random instance of the bathymetry and the travel-time perturbations as a function of RMS height and receiver number is shown on the left-side plots in Figure 4.22. For each random instance, the maximum time perturbation magnitude as a function of RMS height was collected and plotted on the right side. From this right-side plot one may conclude that for smoothed random bathymetry like this, an RMS height of about 3.5m gives as much as a half period (5ms) phase error in the predicted travel-time – enough to cause cycle-skipping – when using the 1D assumption for bathymetry.

It is worth noting that the experiment region's bathymetry is at least readily measured by multi-beam side-scan sonar, so that one can in fact gauge such considerations against the actual experiment environment.

For the medium discontinuities that are internal to the ocean sub-bottom, the results in the model resolution matrix aid consideration of these questions, but the ocean seafloor interface is not included in the model resolution matrix.

Few papers in the ocean geoacoustic literature address the effects of bathymetry errors on inversion results, a notable exception being Li et al. [39] in which it was a small component of a much broader analysis. Dosso [21] et al. jointly invert the bathymetry with a very simply parameterized seabed velocity model. Although solution uncertainties were not explicitly part of that work, in theory the covariances between those joint solution uncertainties would be informative about the sensitivity of the inverted velocity model to the bathymetry variations.

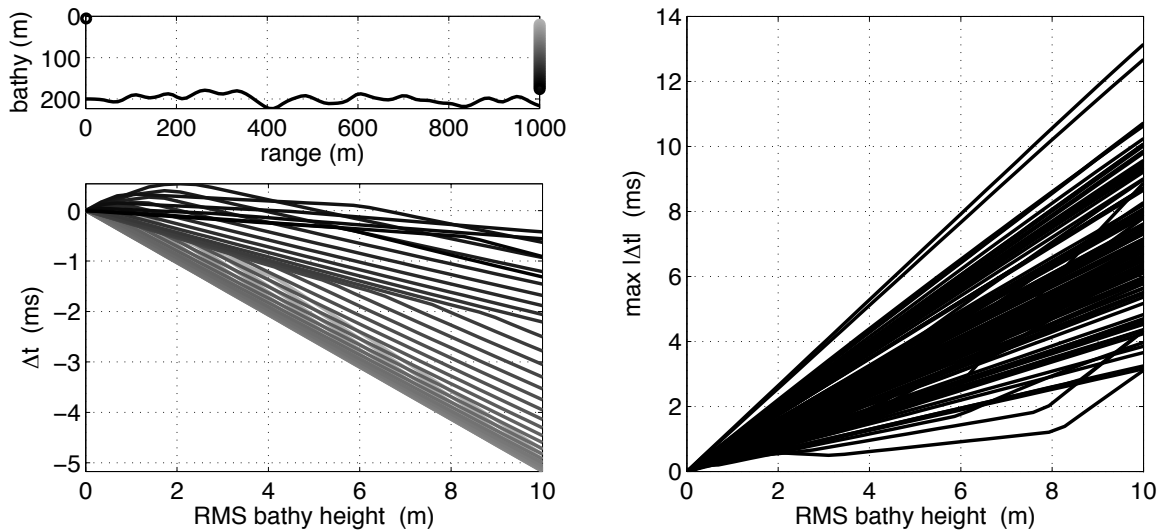


Figure 4.22: The relationship between RMS bathymetry height and the change in travel-time of the first bottom reflection for each receiver. The two plots at left show a single instance of the random bathymetry (top) and travel-time perturbations (bottom) due to that random bathymetry. The bathymetry is a smoothed sequence of independent Gaussian samples scaled with respect to the RMS value. Those travel-time perturbations are a function of receiver number so the grayscale curves coincide with the grayscale of the receivers in the VLA at top. The plot at right shows the maximum time perturbation magnitude as a function of RMS height for 100 random bathymetry instances. From this plot at right one can conclude that an RMS height of about 3.5m can give up to a half period (5ms) phase perturbation.

4.5.5 Internal wave variability in the water

Like the bathymetry, internal waves in the water column are another type of spatial (as well as temporal) variation in the real world that is not modeled in the 1D forward problem used here. The water column is accessible by oceanographic instruments such as conductivity-temperature-depth (CTD) probes, both in vertical casts of a single device as well as in a deep tow of many sensors along a vertical seacable; the data from these devices can provide direct soundspeed measurements of that real-world variation. But the extent of such measurements is always very limited in comparison to the variation of soundspeed in both space and time in the ocean.

The examples in this dissertation attempt to avoid the issue by keeping to a nearly isovelocity ocean soundspeed profile (see Figure 2.2); internal waves would be minimal with the lack of an appreciable density gradient in the water (as suggested by the lack of appreciable soundspeed gradient). Other authors have analyzed the question of internal wave effects on geoacoustic inversion, although not for waveform inversion per se. Lin et al. [40] analyzed internal wave effects on results of continuous-model, linearized geoacoustic inversions of acoustic modal wavenumbers taken over range, but we note that the water soundspeed profiles in their work had considerable gradients for generating internal waves, in comparison to the case in this dissertation. Becker and Frisk [7], Huang et al. [33], and Jiang and Chapman [36] considered the question in estimations of just one, two, or three bottom layers (respectively). The latter two focused on estimating EOFs of the water soundspeed field without considering internal waves specifically; the former two focused on reduction of internal-wave-induced error by averaging out the lateral variation in measured water soundspeed profiles (over 20km range in the first and over 5 hours time in the second). Siderius et al. [65] and Snellen et al. [66] focused on internal wave effects on estimating two sediment layers, but without the mapping of data noise to model uncertainties.

To check whether internal waves cause concern for cycle-skipping in this problem, one can refer to results from a shallow water acoustics experiment of comparable geometry (a portion of the “Shallow Water ’06” experiment) [31]. In this portion of the experiment, the water depth was 80m and the source-receiver range was 1km. Figure 4.23 is a reprint of Figure 4 from reference [31], showing variations due to tidal components (like the 6hr period seen in arrivals 5 and 6), large nonlinear internal waves (the 10min period features from geotime 16.5-17.5hrs), and linear internal waves (the “noisy” scale features) of underwater acoustic receptions over five hours in that experiment. The advantage of considering this data is that it corresponds to a rather extreme case of internal waves in shallow water – the density profile of that water had a very strong gradient (seen in the soundspeed in that paper’s Figure 3), producing unusually large internal waves. As seen in Figure 4.23, even the largest variations in arrival times were only of order of a few milliseconds. While that is for a slightly smaller geometry than that of this dissertation, it is only by a factor of about

two, so the timing variations due to the water variability are still much less than the 50 millisecond limit for cycle skipping.

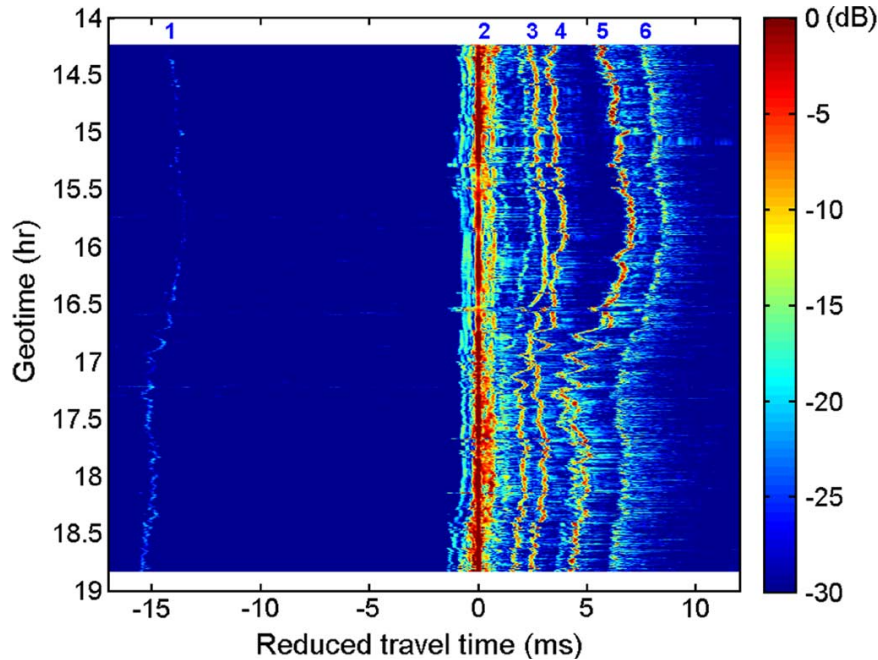


Figure 4.23: Acoustic arrival time variations due to water column variability over five hours, from SW06 experiment (reprinted from reference #[31]). The color scale is acoustic intensity relative to the peak intensity observed during the times shown. Water depth was 80m and source-receiver range was 1km; source depth was 30m and receiver depth was 25m. The six arrivals labeled at top of figure are: #1 a faint arrival that propagated through the surface mixed layer, #2 direct arrival (with which reducing time defined), #3 bottom bounce + subsequent top downturn, #4 top downturn + subsequent bottom bounce, #5 top downturn + bottom bounce + top downturn, and #6 surface bounce + bottom bounce + surface bounce. Three types of water variability are seen at three timescales over the five hours shown in this figure: a tidal component (the 6hr period seen most prominently in arrivals 5 and 6), large nonlinear internal waves (the 10min period features from geotime 16.5-17.5hrs), and linear internal waves (the “noisy” scale features).

4.5.6 Location/time-varying sea-surface roughness

The work in this dissertation neglects the time- and space-varying topography of the sea surface; such an assumption requires calm seas during an experiment. One might address the problem by time-averaging a number of acoustic measurements to average out the

effects of the variable sea surface. Rajan [56, 55] time-gated the measurements to avoid sea-surface returns altogether; a negative side to that approach is neglecting the information in the reflection multiples from the sea-bottom. The geoacoustic literature has few papers specifically regarding the effects of the time-varying rough sea surface upon the uncertainties of geoacoustic inversion results. Zhou et al [76] estimate an “effective bottom loss” that includes rough sea-surface effects and changes with sea-state, noting the changes are small for frequencies below 500Hz. Means and Siderius [45] analyze sea-surface effects on their passive fathometer results and use a normalization on their estimated bottom reflection loss designed to minimize effects of wind speed and sea state. Rouseff and Ewart [59] model time-evolving sea-surface roughness effects in the acoustic propagation itself. This dissertation assumes calm seas, remains at low frequencies, and leaves the effects of sea-surface roughness upon geoacoustic inversion for future work.

4.6 Summary and conclusions

This chapter has explored the application of the linearized inversion machinery described in Chapter 3 to the geoacoustic waveform inverse problem, demonstrated its use in inverting both continuous and piece-wise continuous bottom models, and explored uncertainty and resolution of the solution to one problem at one geometry. The material will be used further to analyze many problems at many geometries in the next chapter.

A limited number of slices of the high-dimensional objective surface of the problem were calculated to try to gauge the multi-modality of the nonlinear problem and how close starting models would need to be to the solution (or true model). Due to the low frequency of the source, results suggested that where the cycle-skipping bounds were tightest, which was near the surface of the model, the starting models merely needed to be within ± 200 - 300 m/s of the solution. Deeper these bounds appeared to be considerably broader – at least ± 1000 m/s in the results investigated. These findings were consistent with the success of the inversion from the several starting models in Section 4.3. Within the local minimum of the solution, objective slices were compared as a function of velocity and of slowness and showed that the shape of the minima were more paraboloidal with respect to slowness, explaining the fewer iterations when the inversions are run in slowness space.

Model averaging kernels showed the inverted solution for the problem explored in this chapter had a depth resolution of about 5m at the surface, and a relatively consistent depth resolution of 15m until the very bottom of the profile where the resolution broadened by a factor of four or more. The consistency of the resolution over most of the profile is attributed to the VLA receivers being situated near the bulk of the returning acoustic energy as shown in Figure 2.2. The next chapter will see the effects upon the averaging kernels of receivers being outside that dense region of returning acoustic energy.

Monte Carlo analysis showed the locally linear approximation of uncertainty and resolution to be a good one down to about 80m depth in this 120m deep model, for the particular choice of true bottom and experiment geometry used in this chapter. Below 80m, the model solution was still essentially unbiased and the variation in the smoothed true model was still minimal, but the variability in the averaging kernels quantifying the resolution increased, showing the resolution was somewhat worse than the linear approximation reported. However, it was also seen that the resolution results have a strong sensitivity to LVZs that appeared in the Monte Carlo solutions, i.e. if no acoustic energy returns to the receivers from a particular model depth span (as due to an LVZ), then the data have no information about that depth span and the resolution results are poor there. A similar Monte Carlo analysis at a different geometry and model depth in the next chapter will provide an interesting comparison to this one.

The adding of discontinuities (solved for in a pre-problem) into the otherwise-continuous inversion to allow for seabed layer interfaces was demonstrated and was robust to errors in the discontinuity depths. It was seen that the component of model structure defined by those discontinuities has a strong effect on the predicted data but is not counted in the model norm, and thus these piece-wise continuous models were smoother between the discontinuities than their fully-continuous counterparts for the same data and configuration. The decrease in resolution of these piece-wise continuous models for increasing noise (decreasing SNR) was shown to progressively reduce the smooth structure between discontinuities to constant gradients for high noise (SNR=3dB).

Chapter 5

**RESOLUTION ANALYSIS OF THE GEOACOUSTIC PROBLEM FOR
EXPERIMENT DESIGN**

The forward problem, method and details of solving the inverse problem, and quantification of resolution and uncertainty to first order have been defined in the previous chapters. Now these shall be used together in a pre-experiment *resolution analysis*, in which the effects of different experiment geometries and array configurations on the problem are investigated without experimental data, with the goal of better understanding the consequences of given geometries on the inversion of the experiment's data. The same approach could also be used to analyze the problem with respect to other experimental parameters such as spectral content or choice of formulation of the model or the data, but we focus here on geometry.

Perhaps the quickest way to get a general feel for which experiment geometries and configurations are better would be to calculate rays, as shown in Figure 5.1 for the shallow water scenario investigated here. From these rays one could see that probably the best placement of a receiver array for a geoaoustic experiment would be one intersecting the bulk of those rays – maybe a vertical line array (VLA) with hydrophones spaced out over the water column at ranges 1.25km, 1.0km, and 0.75km respectively for source depths 5, 100, and 195m, or maybe a horizontal line array (HLA) a kilometer or more long, towed over those same ray-filled regions. But this is a highly qualitative picture. What is missing is more quantitative information, such as: at what specific resolution will the geoaoustic inversion actually resolve the bottom properties at different depths for the experimental setup one chooses? How will the regularization inherent in virtually all (continuous) geophysical inversions affect the choice of experiment setup? Will an HLA or a VLA be better in a particular scenario to intersect those rays? How should the hydrophones in these arrays be

spread out? Questions like these are not answered by looking at the rays, but are precisely what this resolution analysis addresses.

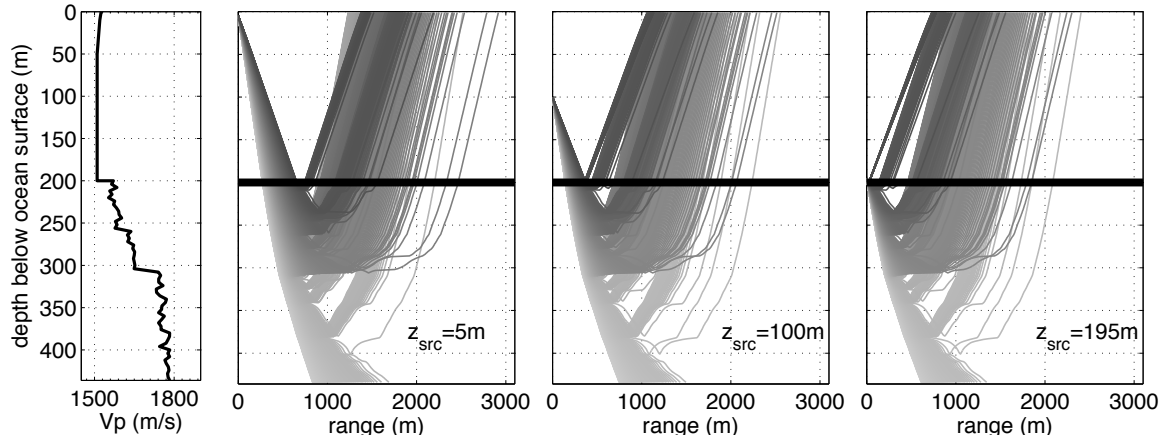


Figure 5.1: Rays for the experiment geometries and one of the bottom model profiles used in the analysis (btm#1), with source depths of 5m, 100m, and 195m. To keep the plots readable, shallower angles of rays were left off since they fall below the critical angle and totally reflect back upwards, and steeper angles of rays were left off since they do not return to the water column at the ranges shown here.

The nonlinearity of this geoacoustic inverse problem is of fundamental importance to this entire work, for the solution and pre-experiment analysis of a linear inverse problem is essentially trivial (to the inverse theoretician at least). The nonlinearity throws the reliability, consistency, and familiarity of the behavior expected in linear problems out the window and causes the behavior to be different in every new problem. There is a range of strengths of nonlinearity however, and the focus of this work is to look at the application and limits of linear tools in pre-experiment analysis, seeing where they are still useful on this nonlinear problem and where they break down.

The resolution and uncertainty of the inverse problem are based on the model's sensitivities to the data, and these sensitivities can vary for two main reasons: 1.) The bottom model sensitivities are directly dependent on varying experiment geometries due to the acoustic field coverage, even for the same model profile. 2.) Also, this is a nonlinear problem so the model sensitivities vary with choice of bottom model profile, and for different problem geometries the inversion will converge to different solution model profiles. For

example, bottom model solutions may be smoother at geometries with less information in the data. In addition to those two issues, the linear tools used to analyze resolution and uncertainty assume that all of the model's sensitivities to the data are contained in the Jacobian matrix of the data with respect to the bottom model, but that is only the first-order description of the sensitivities (which is complete for linear problems). So resolution and uncertainty calculated for a nonlinear problem based on the linear tools may be accurate enough to be useful in some cases but not others. This chapter considers all these issues.

The first three sections of this chapter delve deeply into what the linear tools *can* tell about this nonlinear problem. Using the methods described in previous chapters, the synthetic inverse problem is solved for each combination in a set of source-receiver ranges, source depths, and array configurations. Inherent in those solutions is the quantification of the solution resolution, again focusing on the first-order description of the resolution in this nonlinear problem, as previously defined in Section 3.4 and discussed further in Section 4.5. In the last chapter, results for four different noise levels on the data were compared; in this chapter to keep the discussion focused only one of those noise levels is used for all examples, the one corresponding to a fairly high SNR of 18dB. In Section 5.1 of this chapter, the first-order resolution results are expressed at three different levels of summarization which have different uses. Section 5.2 analyzes resolution dependence on experiment geometry and receiver array type and configuration in these problems. The patterns seen in the resolution variations over experiment geometries in that section is then explored more deeply in Section 5.3 by investigating changes in the singular value spectra and singular vectors of the (locally linearized) problem.

The fourth and fifth sections of this chapter concern issues and limits in using linear tools to analyze uncertainty and resolution in this nonlinear problem. Section 5.4 looks at the linear tools' limits in terms of an individual inversion, using Monte Carlo methods. Even aside from the immediate dependence of the uncertainty and resolution on the bottom model, the first-order information in the covariance matrix and resolution matrix is not all of the uncertainty and resolution information in the nonlinear problem, so it is important to explore where the higher-order information becomes important and where it does not. Section 5.5 looks at the linear tools' limits in terms of patterns in the many inversions used

in the resolution analysis with a range of “true” bottom models. Since this is a nonlinear inverse problem, the uncertainty and resolution results are dependent on the bottom model, so resolution results are compared for the different “true” models to see if some useful patterns and conclusions still remain across all of them in this problem. That section also considers whether and when a suite of complete synthetic inversions are necessary as opposed to relying on a single bottom model for the whole analysis, a significant savings in computation.

5.1 *Three levels of resolution summarization*

The complete first-order description of the model resolution is contained in the model resolution matrix as shown for example in Figure 4.7; it has dimensions equal to the number of model parameters squared. Quantitatively comparing resolution results between different geometries is very difficult using these matrices, motivating other ways of displaying and analyzing their contents. The three levels of summarization discussed here trade off spatial averaging of the information in one way or another with the dimension of the resulting statistic. The higher dimensional views are likely more useful to a human observer when only a few objective variables are considered, such as source depth and source-receiver range. More condensed summaries may be useful in certain situations when trying to automate an experiment optimization based on this information, or when more objective variables are used. However, with increasing level of summarization, information content is lost; this section describes the advantages and disadvantages with each level.

5.1.1 Averaging kernels

This level can potentially encompass all the information in the model resolution matrices at once, although pragmatically one often chooses to plot a subset for readability as in the figures shown here. Grayscale images or waterfall plots of a series of model resolution matrices themselves (as in Figure 4.7) may be useful on a qualitative level, but are difficult to compare visually; the plots described in this section can present a far more quantitative picture of the same information.

The elements of the model resolution matrix are the weights relating the smoothed version of the model being estimated to the rough true one; that is, these weights parameterize the transfer function relating the estimated and true continuous models. In our case the model parameter vector is a fine discretization of the continuous model, so the columns of the resolution matrix are the impulse responses for each model parameter as it is mapped through the inversion. If the true model perturbation were simply a unity spike function at a given depth, the inversion smears out that spike (typically broadening it around the spike depth) such that only the smeared version can be recovered, as quantified to first order by the impulse response in the model resolution matrix. A common term for these impulse responses in the geophysical inverse community is “averaging kernels”, from Backus and Gilbert’s original paper on the subject [4].

Figure 5.2 shows a suite of these averaging kernel plots together, based on a similar inverse problem as in the previous chapter but here using a 1km long horizontal line array (HLA) with 40 hydrophones, towed at 10m depth over varying range with a near-bottom source at 195m. The averaging kernels in well-behaved cases such as this one look like humps that are of height between zero and one (but technically they are not bounded by zero and one), typically centered at the spike function location and surrounded by fluctuations close to zero away from the hump. The hump narrows and approaches a height of one as the resolution improves, just as the resolution matrix approaches an identity matrix as the resolution improves. To display the averaging kernels for every single parameter superimposed at once in this plot would be difficult to decipher, so six of the averaging kernels are superimposed to show changes of resolution at a set of depths (via differing hump heights and widths). These are then laid out over the set of source-receiver ranges and source depths considered in the analysis. The strength of these plots is that the hump widths directly present the actual depth resolution of the inversion as a function of geometry and model depth before the experiment is even done. The spacing on the x-axis is normalized such that an averaging kernel’s hump height of zero is at the tick-mark of that kernel’s source-receiver range, and a hump height of one (i.e. perfect resolution in a narrow hump) is at the next range’s tick-mark. Note that the closest source-receiver range of 0.1km in this plot is shown at the zero-range location in order to correctly show that 0-1 span of

the averaging kernels for that range. Other features seen in Figure 5.2 include a decrease in resolution (widening and shortening humps) with depth, and to a lesser extent with range, and a particularly high resolution next to the seafloor interface. The resolution in the shallower half of the profile improves as range decreases, but at depth it suddenly drops off quickly at close range. At the shortest ranges the averaging kernels lose their “hump” form at deepest depths, showing that the resolution is particularly poor in that location. Averaging kernel plots in upcoming sections will show even more disfigured averaging kernels in those short-range regions for array configurations that cannot adequately resolve the bottom model profile in those locations.

Many of the results later in Section 5.2 will be discussed with the use of this form of plot. This is the most quantitative display of the resolution results, but it is a lot of information, and these plots are for only two objective variables (source depth and range). When trying to overlay such plots for different scenarios (for example for different bottom model profiles) one ends up with an unreadably dense spider-web, so may benefit from a somewhat more summarized version of this information.

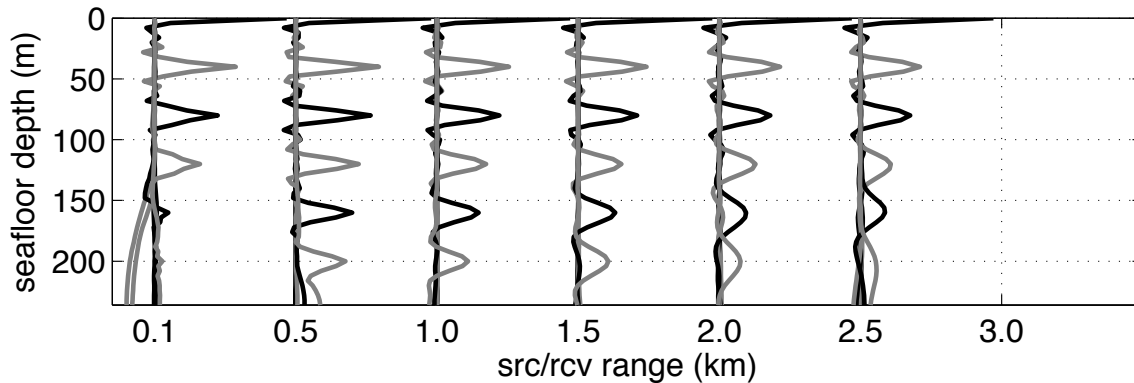


Figure 5.2: Averaging kernels as a function of model depth and source-receiver range, computed from complete synthetic inversions with a 1km, 40-hydrophone HLA towed at 10m depth. The arrays extend from the source-receiver range shown on the x-axis to that range plus 1km. The “true” bottom model is btm#1 (Figure 5.15); the source depth was 195m in a 200m ocean. For clarity, only six of the sixty averaging kernels (every tenth parameter) are shown superimposed, and alternating kernels are shown in black or gray to aid the eye.

5.1.2 *Diagonals of the model resolution matrices*

The next level of summarization, which reduces the information by a dimension, is the diagonal of the model resolution matrix. There are caveats for when this is appropriate to rely on and when it is not, but this shall be explained below.

The diagonal elements of the resolution matrix are equal to one where there is perfect resolution, since the model resolution matrix becomes an identity matrix at perfect resolution. The diagonal value decreases with decreasing resolution, just as the humps in the averaging kernels (the center of which is typically the diagonal value) decrease in height and broaden with decreasing resolution. The value along the resolution matrix diagonal is presented in the plots such that a value of zero is at the tick-mark of that resolution diagonal's source-receiver range, and a value of one is at the next range tick-mark. Also as with the averaging kernel plot in Figure 5.2, the resolution diagonal for range 0.1km is shown at the zero-range location in order to correctly show the same zero-to-one span at that range.

Figure 5.3 shows a suite of the resolution matrix diagonal plots together, based on the same inverse problem as in Figure 5.2 and corresponding to the averaging kernels in that plot. The diagonals show the same features in the resolution given by the averaging kernels, at all the depths rather than just six: One sees the particularly high resolution next to the seafloor interface, the decrease in resolution (decreasing resolution diagonal value) with depth, and on close inspection the more subtle decrease in resolution with range at a given depth. Some additional features that were not seen in the averaging kernel plots in Figure 5.2, since not all averaging kernels could pragmatically be shown there, are: the drop in resolution under the biggest bottom model profile discontinuity at approximately 100m depth (see the model plotted in Figure 5.1 or in larger format in Figure 2.6 back in Chapter 2) becoming gradually more apparent with range, and the artifact at the very bottom of the profile due to the effect of the half-space basement placed below the many finely discretized layers by the forward problem code. The latter shows that the model's microlayers should be defined to a bit deeper depth so that the sensitivity at the basement depth is more negligible, but this issue does not otherwise affect any of the conclusions or demonstrations

shown in this dissertation. Lastly, the increasingly varying features at the bottom of the resolution diagonals from 1.0km down to 0.1km reflect the poor resolution that was also seen in those locations in the averaging kernels, leading to the following caveat to be aware of in the use of the resolution diagonal plots.

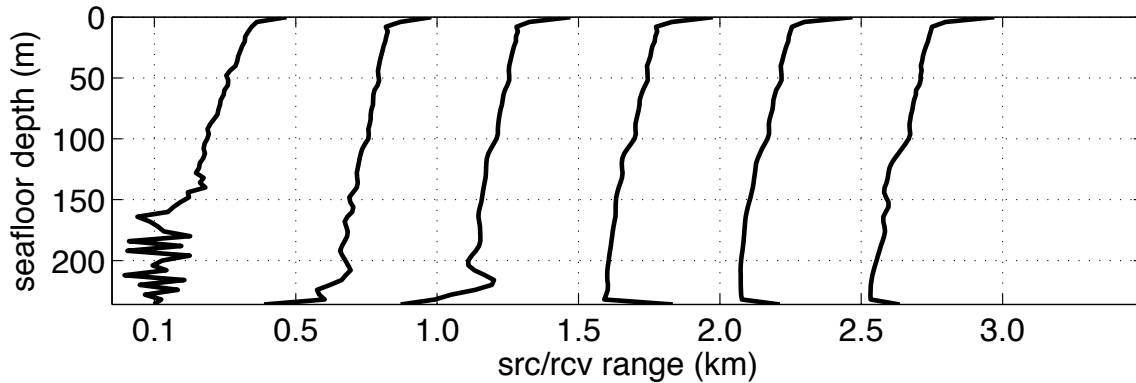


Figure 5.3: Resolution matrix diagonals as a function of model depth and source-receiver range, computed from complete synthetic inversions with a 1km, 40-hydrophone HLA towed at 10m depth. The “true” bottom model was btm#1, shown in Figure 5.15; the source depth was 195m in a 200m ocean.

Figure 5.4 shows resolution results from a much shorter 200m HLA towed at the same depth in the same problem. When there is enough information in the data to resolve the bottom model profile (right side of the figure, farther ranges), the resolution diagonals precisely follow the peaks of the averaging kernels and thus provide information about the peak widths since the two are related. However, this 200m HLA is too short to resolve the bottom model profile at short ranges. Behind the wildly messy resolution diagonal curves (left side of figure, shorter ranges), the non-peaked nature of the corresponding averaging kernels can be seen for those short ranges, and the resolution diagonals essentially give no useful information in those minimal-resolution cases. The next section in this chapter will show how those poor resolution areas can be improved by altering the array configuration, and additionally the behavior of the averaging kernels in this sense could be checked first separately in averaging kernel plots before overlaying them for example.

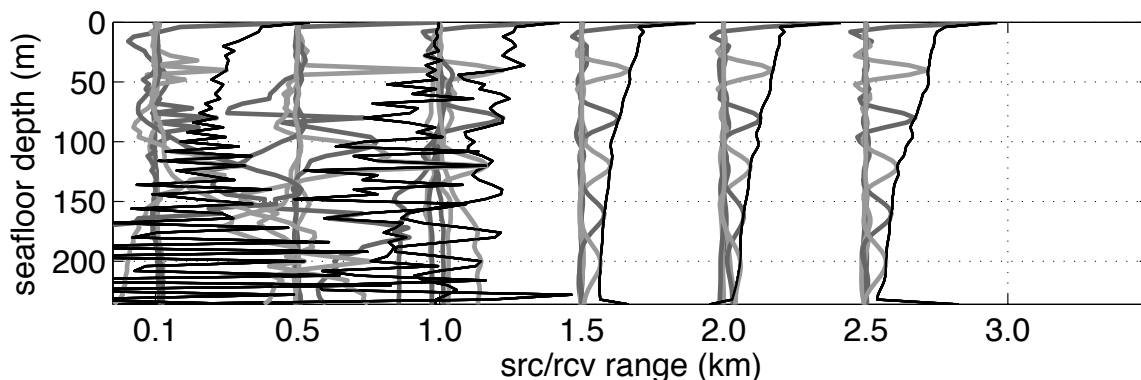


Figure 5.4: Resolution results from a shorter 200m (but still 40-hydrophone) HLA towed at 10m depth are used to demonstrate the relation between the resolution matrix diagonals and averaging kernels. The “true” bottom model was btm#1, shown in Figure 5.15; the source depth was 100m in a 200m ocean. The resolution diagonals are the black lines and the corresponding averaging kernels are the gray ones. This case was specifically chosen to describe and compare the regimes in which the resolution diagonals are well-behaved (right side, farther range) and poorly-behaved (left side, shorter range), as discussed in the text.

5.1.3 Trace of the resolution matrix

The above two types of plots present a great deal of information to the human viewer. But a further level of summarization may be of interest when either:

1. more objective parameters are of interest in the resolution analysis than just a few like source depth and source-receiver range and array length, confounding the presentation of higher dimensional information in the previous type of plots.
2. some sort of automated analysis is of interest such as an optimization, which requires a scalar parameter to optimize over.

The summary quantity discussed in this section is the trace of the model resolution matrix. This quantity not only reduces the resolution information to a single average value (for each objective point in our source depth and source-receiver range space), but in addition, the trace of the resolution matrix will be mathematically shown to represent the number of model parameters resolved by the inversion. This was demonstrated by

Tarantola [72] for the related but different case of Bayesian inversion, but here it is shown that a similar interpretation can be derived for frequentist inversion which is the framework used in this work.

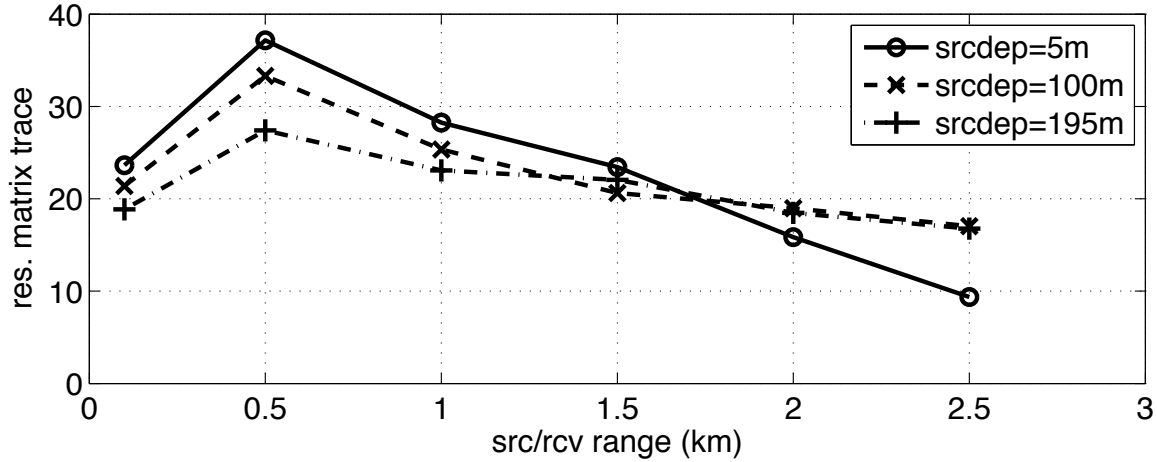


Figure 5.5: Resolution matrix traces as a function of model depth, source depth, and source-receiver range, computed from complete synthetic inversions with a 1km, 40-hydrophone HLA towed at 10m depth. The “true” bottom model was btm#1, shown in Figure 5.15; the source depth was 195m in a 200m ocean.

To show that the trace of the resolution matrix can be interpreted the same way in the frequentist framework, the resolution matrix \mathbf{R} defined in Eqs. (3.21) and (3.23) is now re-expressed using the generalized singular value decomposition (GSVD) [25] as shown in Aster et al [3]. The mathematical definition of the GSVD and derivation of the model resolution matrix in terms of it are found in Appendices A.1 and A.2 respectively.

Using the material in Appendix A.2, the resolution matrix defined in Eq. (3.23) is rewritten in terms of its GSVD components as:

$$\mathbf{R} = \mathbf{X} \begin{bmatrix} \mathbf{F} & \mathbf{0} \\ \mathbf{0} & \mathbf{I}_{n-q} \end{bmatrix} \mathbf{X}^{-1} \quad (5.1)$$

where \mathbf{X} , \mathbf{F} , and \mathbf{I}_{n-q} are all defined in Appendix A.1, and are based on the regularization matrix \mathbf{L} as laid out in that Appendix. In the special case where $\mathbf{L} = \mathbf{I}$, the GSVD reduces to the traditional SVD and Eq. (5.1) here simplifies to the SVD expression for the resolution

matrix. From Eq. (5.1) for the resolution matrix one can write the following identity:

$$\mathbf{R} - \mathbf{I} = \mathbf{X} \begin{bmatrix} \mathbf{F} & \mathbf{0} \\ \mathbf{0} & \mathbf{I}_{n-q} \end{bmatrix} \mathbf{X}^{-1} - \mathbf{X}\mathbf{X}^{-1} \quad (5.2)$$

This equation is easiest to interpret in the special case in which the filter factors in \mathbf{F} (defined in Appendix A.2) are either zeros or ones, as in the “truncated generalized singular value decomposition” or TGSVD method of inversion[3]. In that case, \mathbf{F} ’s diagonal elements are either zero or one so that on the RHS of Eq. (5.2), the trace of the diagonal matrix in the first term is some positive integer that is less than the number of model parameters; it is the number of model parameters resolved by the measured data. The trace of the implied identity matrix in the second term of Eq. (5.2), in which $\mathbf{X}\mathbf{X}^{-1} = \mathbf{X}\mathbf{I}\mathbf{X}^{-1}$, is the total number of model parameters because that is the dimension of \mathbf{X} as defined in the Appendix. The difference between these two traces is thus the number of model parameters filled in by the regularization.

In the more general case beyond TGSVD, such as the Tikhonov regularization used in this work, the filter factors vary more smoothly than a simple stair-step between zero and one. In this case the trace in that first term on the RHS of Eq. (5.2) is not an integer as it was above, but the interpretation is the same.

If we define \mathbf{Y} as the negative of the RHS of Eq. (5.2):

$$\mathbf{Y} \equiv - \left(\mathbf{X} \begin{bmatrix} \mathbf{F} & \mathbf{0} \\ \mathbf{0} & \mathbf{I}_{n-q} \end{bmatrix} \mathbf{X}^{-1} - \mathbf{X}\mathbf{X}^{-1} \right) \quad (5.3)$$

and rearrange the terms in Eq. (5.2) then we can now see, in an expression directly analogous to Tarantola’s development [72], that:

$$tr(\mathbf{I}) = tr(\mathbf{R}) + tr(\mathbf{Y}) \quad (5.4)$$

where

$$tr(\mathbf{I}) = \begin{bmatrix} \text{total number of} \\ \text{model parameters} \end{bmatrix} \quad (5.5)$$

$$tr(\mathbf{R}) = \begin{bmatrix} \text{number of parameters} \\ \text{resolved by the measured data} \end{bmatrix} \quad (5.6)$$

$$tr(\mathbf{Y}) = \begin{bmatrix} \text{number of parameters} \\ \text{filled in by the regularization} \end{bmatrix} \quad (5.7)$$

Again, that “number of parameters” in Eqs. (5.6) and (5.7) is not an integer quantity in general (it only is in that TGSVD special case), but the interpretation is the same in the sense of how much of the model has been resolved.

In evaluating the resolution of inversion results based on just the trace of the model resolution matrix, the information about depth-variation in the resolution is lost into the average, but this high-level summary value, which can be used in plots or optimizations, has a specific relevant meaning – the number of parameters resolved by the inversion of the measured data. (It could equivalently be expressed as a percentage of the model resolved by the inversion as long as the parameterization is accounted for.) As such it can be considered a proxy for information content in the inversion solution that takes into account not only the data but also the form of regularization used in the inversion.

However, as with the resolution diagonals, there are practical caveats to note with its use. Relying solely on the percentage of the model that is resolved in the inversion can be misleading. In plotting this quantity as in Figure 5.5, one does not distinguish between effects that are due to the experiment geometry (or array configuration etc) and effects that are due to instabilities in the inversion, just as discussed above regarding the resolution diagonals. The result is accurate but requires additional analysis of the stability issue as discussed for the resolution diagonals in order to be particularly useful when used for either plotting over objective variables or used in an optimization routine.

5.2 Resolution over varying experiment geometries and array configurations

This section focuses on variations in resolution over range, depth, source depth, and array configuration. It will be seen that source depth is not as strong an influence as the other factors in the problem explored here, and that significant differences in resolution of the inversion result can be obtained by rearrangement of the same set of 40 hydrophones. Averaging kernel plots will be used to compare resolution results. To investigate the problem over the four geometry parameters mentioned above, two sets of three parameters will be analyzed at a time in this section: first different experiment geometries in terms of varying source depth and source-receiver range, and then different array configurations in terms of VLAs and HLAs of varying lengths and source-receiver range.

5.2.1 Results at different source depths for given array configurations

These results are generated from complete synthetic inversions at three different source depths and six or seven source-receiver ranges. Once the correct solution model profile is inverted for each geometry, the problem is linearized at that profile and the Jacobian matrix is used to produce the resolution matrix (as described in Section 3.4) from which the averaging kernels are displayed. The type of averaging kernel plot introduced in Figure 5.2 is shown in triplets in the next few figures, one panel for each of three source depths.

Figure 5.6 shows averaging kernels as a function of depth, source range, and three source depths, computed for a 1km long, 40-hydrophone HLA towed at 10m depth. The “true” bottom model used for the synthetic data was btm#1, shown in Figure 5.15; the ocean depth was 200m. Note that Figure 5.2 makes up the bottom panel of this figure, but that now one can look at the source depth dependence. Features to note in this figure include the following. As in Figure 5.2, there is an increase in resolution as the HLA gets closer to the source overall, but with a depth dependence such that the deep resolution drops off quickly at the closest range of 100m. In this high-SNR and perfectly forward-modeled problem with a single known bottom profile, the resolution appears somewhat better at farther ranges for the deeper source and somewhat better at closer ranges for the shallowest source. But

accounting for variability in the bottom profile and a real-world inversion that by definition is not perfectly modeled, these last differences are doubtfully significant.

Comparing this figure to the rays back in Figure 5.1 is useful as well – the resolution of the inversion is greatest when this 1km HLA covers the 0.5-2.0km range window (recall that the range marked on the plot refers to the closest element in the HLA), which corresponds to the densest region in the rays. At farther ranges the resolution gradually diminishes as the rays spread out, and at close range there is a change in the physics such that the propagation shifts from refraction receptions to reflection receptions – do note that the rays in Figure 5.1 only show refraction; no reflections are seen in those diagrams, but that is where the close-range arrivals come from.

The results in Figure 5.7 are analogous to the above but for a much shorter HLA of 200m. Problems at the short ranges in this plot are indicative of the information limits in the data due to the greatly reduced angular coverage caused by the short array length. These results show the difficulties raised earlier in Section 5.1.2 when discussing the caveats of the resolution diagonals and Figure 5.4 (in fact Figure 5.4 was based on the middle panel of Figure 5.7 here). The present choice of regularization is not enough to stabilize the problem in many of the geometry choices with this short array, resulting in those “messy” averaging kernels at ranges closer than 1.5km. Note the problems in some of the averaging kernels even at farther ranges – for example in the 5m source depth plot at top of the figure, not all kernels are unimodal, as seen via the overlapping bumps. Again as the range increases, the resolution decreases as the rays spread out, with deeper parts of the bottom model decreasing in resolution before shallower parts. In spite of the difficulties at close range, Figure 5.7 is still useful because it shows, for a set choice of the regularization and of the hydrophone array, which geometries will provide good resolution (and quantifying how good) and which will not. The regularization in this problem is the same as in the previous chapter – Tikhonov-based smoothing to discourage unjustified features, plus gradient minimization to discourage unjustified higher gradients and any reflections from the basement, which the forward code requires at very bottom of the model. Arbitrarily adding in more regularization (such as model value minimization by adding an identity matrix onto the regularization matrix, for example) does in fact stabilize the problem further so that the “messy” averaging

kernels at closer range will not appear in this resolution analysis, but it does not add any more information to the problem, and in particular does not add physically justifiable constraints as the first two could be argued. Instead the analysis in its present form has helpfully shown experiment geometries to avoid.

Figure 5.8 shows resolution results for a single VLA, moored at various ranges from the source, with the source at the same three possible depths. The resolution in these VLA results is comparable to those of the 1km HLA at mid-ranges in those plots, and perhaps even somewhat better than the 1km at longer range with a shallow source (although as above, when accounting for variability in the bottom profile and the real-world inversion this improvement is likely insignificant). Like the 200m HLA, the VLA is seen in these plots to perform poorly at ranges closer than 1.0 or 1.5km in this problem, whereas the 1km HLA has enough coverage to handle short as well as long ranges for all the source depths. In each of these cases, the similarities can be interpreted in terms of the arrays intersecting the same rays in the rays, whether the arrays are horizontal or vertical ones.

Overall then, these HLA and VLA results show that for this problem, at ranges of 1.5km or greater the results are comparable between the VLA and HLA configurations shown, with the same number of hydrophones in each case, while at shorter ranges the 1.0km HLA is clearly more successful than the VLA or short HLA. The results do not appear strongly dependent on the source depth; however, these analyses are based on a synthetic problem with perfect forward modeling. In a real world experiment the increase in SNR from using a deeper source may allow for better resolution results than a shallow source.

5.2.2 Results for different array configurations at a given source depth

Next, rather than results at three source depths for one array configuration, here are presented results for one source depth with multiple array configurations. Figures 5.9 and 5.10 focus on just one of the source depths – the 5m one – and show the improvement in resolution results in both the HLA and VLA context when arranging the same set of 40 hydrophones in different lengths of HLA or spread between different numbers of receiver moorings.

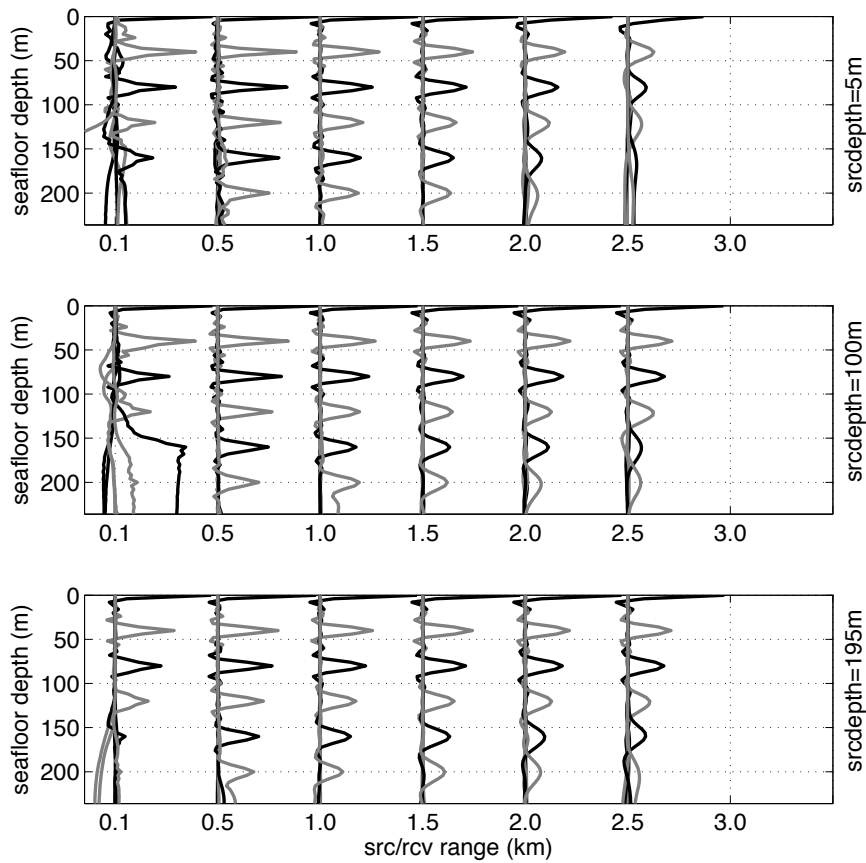


Figure 5.6: Averaging kernels as a function of depth, source range, and three source depths, computed from complete synthetic inversions with a 1km, 40-hydrophone HLA towed at 10m depth. The “true” bottom model was btm#1, shown in Figure 5.15; the ocean depth was 200m. Figure 5.2 makes up the bottom panel of this figure.

Unlike the previous three figures which were all computed from many complete synthetic inverse problems solved for each combination of geometry analyzed, here the results are computed from Jacobian matrices based on a single true bottom model profile. The difference between the results from the true model and those from the complete synthetic inversions corresponds to the difference between the true model and approximations to it of various smoothness. As will be seen later in Section 5.5, these differences between results from the synthetic inversions and those from the same true model are much smaller than those between inversions for different true bottoms, and in fact are small in general in this problem. In other words, the material in Section 5.5 justifies basing the resolution results

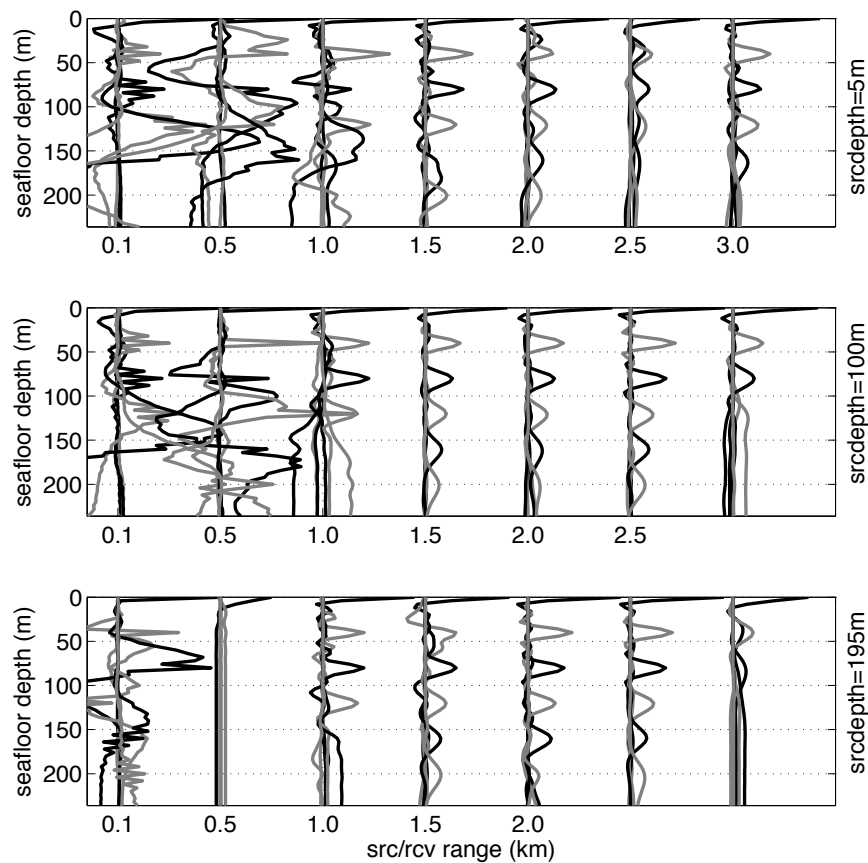


Figure 5.7: Averaging kernels as a function of depth, source range, and three source depths, computed from complete synthetic inversions with a 200m, 40-hydrophone HLA towed at 10m depth. The “true” bottom model was btm#1, shown in Figure 5.15; the ocean depth was 200m. Figure 5.4 is based on the middle panel of this figure.

in this section on the true model instead of on the inversion solutions. This is key, because the computation of the estimated derivatives in this problem is highly intensive.

The HLA results are shown in Figure 5.9. On the right side of the figure, the geometry of the receiver hydrophones and the source is shown for just the plot’s 0.5km results, to demonstrate the geometry used similarly for all the other ranges. The range on the x-axis of the averaging kernel plots is that of the closest hydrophone in the array in each case. So the top row shows the results for a 200m long array with 40 equally-spaced hydrophones, with the closest hydrophone at the x-axis value on the left. The spacing for the other three rows requires a little bit more explanation, as results for the three longer HLAs were created by

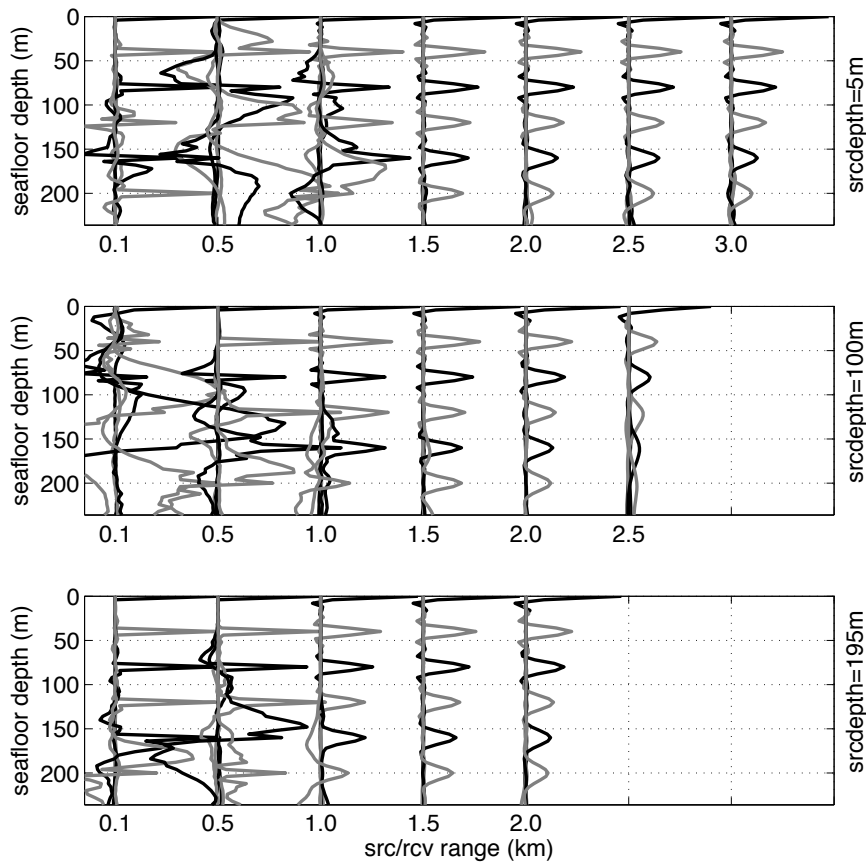


Figure 5.8: Averaging kernels as a function of depth, source range, and three source depths, computed from complete synthetic inversions with a 40-hydrophone VLA spanning the water column. The “true” bottom model was btm#1, shown in Figure 5.15; the ocean depth was 200m.

concatenating Jacobian matrices of the 200m array from different ranges. So in the second row, the 700m HLA still contains 40 hydrophones, but they are actually contained in two equally-spaced subarrays which together span 700m (every second hydrophone from pairs of 200m HLAs in the first row). In the third row, the 1200m HLA contains 40 hydrophones in three equally-spaced subarrays spanning 1200m (every third hydrophone from triplets of the 200m HLAs in the first row). And in the fourth row, the 1700m HLA contains 40 hydrophones in four equally-spaced subarrays spanning 1700m (every fourth hydrophone from quads of the 200m HLAs in the first row). In the second, third, and fourth rows, the

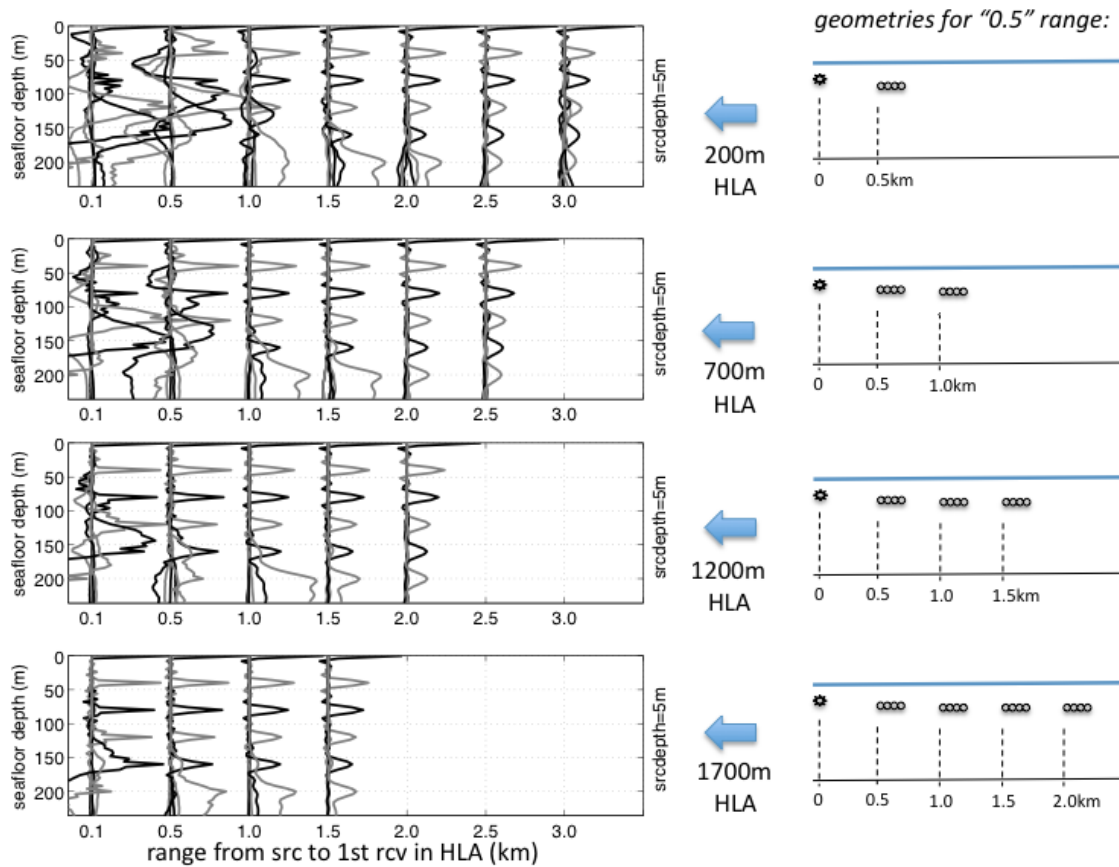


Figure 5.9: Improvements in stability and resolution with lengthening and positioning of HLA. Here the averaging kernels are functions of depth and source range, all for a source depth of 5m in every case, for four different lengths of HLA, each with 40 hydrophones spread over its respective array length. Results are produced from Jacobian matrices at the “true” bottom model of btm#1 (shown in Figure 5.15). The ocean depth was 200m. The array configurations for each of the four cases is depicted on the right for just the 0.5km range. The results for the other ranges are produced similarly, using the range increments shown on the plots; the range value on the plot is that of the closest element in the HLA. Note the improvement in resolution results at close range with the lengthening of the HLA.

missing averaging kernels at farthest ranges are due to this grouping of Jacobian matrices from the 200m array at various ranges in the top row.

The point of Figure 5.9 is to show not only that the resolution problems at close range can be ameliorated with increased HLA length (even for same number of hydrophones), but specifically how the results improve with specific array lengths. As seen in the plots, the

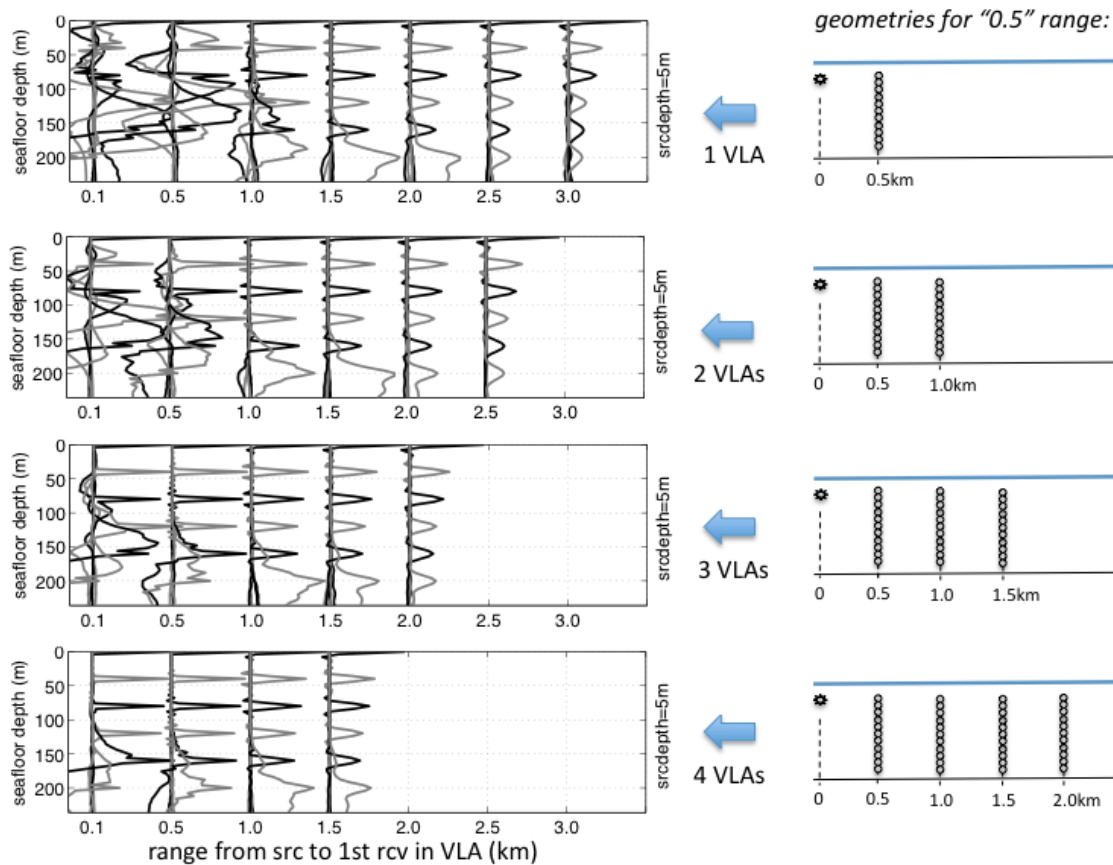


Figure 5.10: Improvements in stability and resolution with lengthening and positioning of VLA. Here the averaging kernels are functions of depth and source range, all for a source depth of 5m in every case, for one, two, three, or four VLAs, each case with 40 hydrophones spread over all the VLAs. Results are produced from Jacobian matrices at the “true” bottom model of $btm\#1$ (shown in Figure 5.15). The ocean depth was 200m. The array configurations for each of the four cases is depicted on the right for just the 0.5km range. The results for the other ranges are produced similarly, using the range increments shown on the plots; the range value on the plot is that of the closest VLA. Note the improvement in resolution results at close range with more VLAs.

lengthened arrays do not necessarily improve the resolution at farther ranges, where there was already sufficient information in the data. But for closer ranges, the addition of farther receptions stabilizes the problem and brings the averaging kernels into much sharper focus, in fact the sharpest of all the ranges (acknowledging the remaining drop in resolution at

depth). The framework of a very long HLA (or many HLAs) used for close range work is precisely that used by the oil exploration community.

Figure 5.10 presents an analogous set of resolution results from groups of VLA moorings. As in Figure 5.9, the right side of this figure shows the geometry of the receiver arrays just for the plot's 0.5km results, but the same layout is used at each range increment on the x-axes on the left side of the figure. The range on the x-axis is that of the closest mooring in each case. Also as above, the multiple-VLA cases are produced by combining Jacobian matrices from the single-VLA case in the top row of the figure. The top row shows the results for a single VLA of 40 equally-spaced hydrophones moored at each depth in the x-axis of the averaging kernels plot. The VLA essentially covers the water column (every four meters from 20 to 176m depth). The results in the second row of the figure are based on Jacobian matrices at pairings of ranges in the top row, but using every second hydrophone so that still only 40 hydrophones are used altogether. Similarly the third and fourth rows of the figure depict results for triple and quadruple groupings of the Jacobian matrices from the ranges in the top row's case, decimated to keep only 40 evenly distributed hydrophones in each case. In the second, third, and fourth rows, the missing averaging kernels at farthest ranges are due to the grouping of Jacobian matrices from the array at various ranges in the top row.

These plots in Figure 5.10 show patterns very similar to those in Figure 5.9, largely because these VLAs intersect the same rays as the HLAs did previously. The resolution at farther ranges remains consistent with additional VLAs, but that at close ranges improves dramatically with the additional VLAs.

The HLA and VLA cases explored here give similar results, but one configuration may be preferable to the other in a given experiment. The amount of specific details that can be used from resolution plots such as those in this section depends on how much is known *a priori* about the ocean bottom in the experiment region (i.e. is the candidate bottom profile used just one of many wild guesses which are being compared, or is it known to be closer to truth, based say on previous experiments?). With some structure already known, the details in these averaging kernel plots have more use than if less is known beforehand. In the latter case, these types of plots can be produced for a number of different candidate bottom

profiles, based on what is known about the area, and the broader patterns compared between the results to investigate choices of experiment geometry. This is the subject of Section 5.5. First, however, there is more that can be learned about these patterns in resolution as a function of experiment geometry and array configuration for a given candidate model profile, even just looking at a first-order description by analyzing singular value spectra and singular vectors of the problem.

5.3 SVD analyses of those geometry and array comparisons

As seen in earlier chapters, the multi-component Tikhonov regularization used in these geoaoustic inverse problems is more involved than simply truncating small singular values. However, looking at the singular value spectra and singular vectors for the locally linearized problems can greatly help the understanding of where information content changes or dwindles, and the links between that information content and the model structure. This section explores and compares the 200m-long and the 1km-long HLA examples via singular value decomposition (SVD) of the Jacobian matrix of the problem locally linearized at the “true” solution (the same true solution as in the previous discussions).

To clarify, while the regularization itself was not done by truncating a simple SVD, the inversion is still done with local linearizations and local Jacobian matrices. Since the SVD is a complete representation of the content of such a matrix, it is completely valid to explore the problem in this familiar format by decomposing and comparing the problem matrices before and after their regularization.

Figure 5.11 shows two sequences of singular value spectra over range, one for the 1km HLA (5.11a) and one for the 200m HLA (5.11b), at the same seven ranges used in Figure 5.9. As previously, the seven ranges span from 100m to 3km; this is the horizontal distance between the source and the first receiver in the HLA. Each subplot shows two singular value spectra. The black is that of the regularized problem $[\mathbf{G} \ \hat{\alpha}\mathbf{L}]^T$ (where $\hat{\alpha}$ is the regularization trade-off parameter at the solution, chosen via the knee of the L-curve), and the gray is that of the unregularized problem \mathbf{G} .

One of the first features to notice in these sequences of singular value plots is the strong range dependence of the spectra of the unregularized (“data-only”) problem. For both the

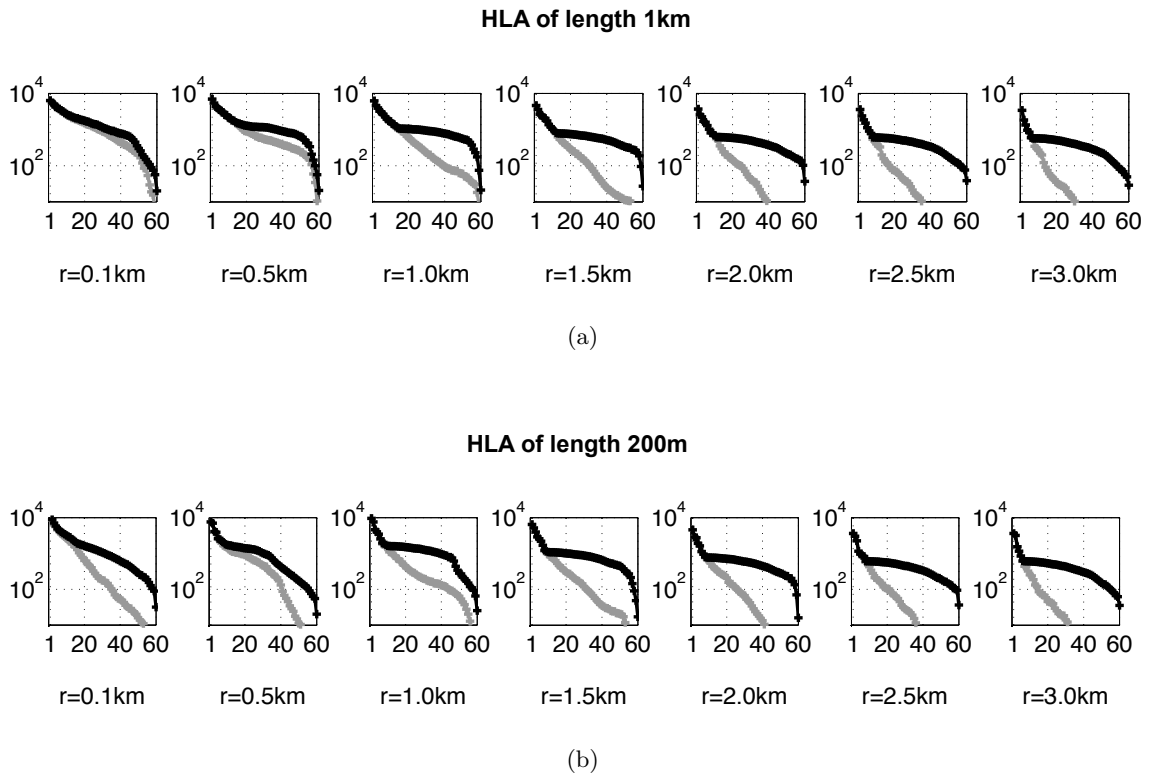


Figure 5.11: Range dependence of singular value spectra corresponding to the (a) 1km HLA problem in Figure 5.6 and the (b) 200m HLA problem in Figure 5.7. Axis labels were left off in order to fit the plots in one figure; the x axes are singular value index (the singular values are arranged in order from greatest to least), the y axes are the value of the singular values on a logarithmic scale. Source depth was 5m. The gray spectra are for the unregularized problem; the black spectra are for the regularized problem.

1km and 200m lengths of HLA, the spectral slope decreases significantly with range, which in turn de-weights more singular vectors as range increases, effectively reducing over range the number of singular vectors defining the structure of the bottom model. This corresponds with the ray picture shown in Figure 5.1, in which ray coverage decreases with range beyond a range of about 1km.

Still focusing on the unregularized spectra, next note in comparing the 1km and 200m HLA results that the spectra are very similar at farther range (say ≥ 1.5 km) but quite different from each other at short range. Considering the ray picture again, the 200m HLA

intersects far fewer rays at a time than the 1km HLA, and at ranges closer than 1.5km there are fewer rays. So at close range the 200m HLA has less sensitivity to the bottom model than the 1km HLA, which at close range can still reach into regions with more rays than the shorter array can. It is not that there is no information about the bottom model at close range – if this were the case then the singular value spectra (as well as the resolution results in Figure 5.9) at close-range with the 1km HLA would be no better than those at mid-range – and note there are reflecting rays at short range not depicted in Figure 5.1. But the problem null space at close-range with the 200m HLA is such that the regularization is not enough to stabilize the problem there.

Now considering the regularized (black) spectra in this same Figure 5.11, one sees that although the regularized spectral level remains about the same over range (i.e. the problem had to be regularized to raise the singular value spectra up to a certain level), the differences between the regularized and unregularized spectra increase over range. In other words, the problem had to be regularized more at the greater ranges, which corresponds to the gradually decreasing resolution with range seen in earlier figures such as Figure 5.9.

While the same regularization is used on both the 1km and 200m HLA problems, the regularized spectra in the shorter HLA drops off earlier than those for the longer HLA at short ranges. This is associated with the fact that as seen in earlier sections, the regularization was not enough to stabilize the 200m HLA problem at short ranges. The longer HLA provides the extra information needed at these short ranges, as can be seen further in the plots of the singular vectors.

Figure 5.12 shows sets of singular vectors associated with four of the subplots in Figure 5.11: the decompositions for both the 1km (5.12a) and 200m (5.12b) HLAs at 0.5km and 2.5km, i.e. a short-range and a long-range example for each HLA length. The indices on the x axis correspond to those on the x axes in Figure 5.11, so the singular vectors with the lowest indices are weighted the strongest in the decomposition; thus note only the first 25 singular vectors (of 60) are shown in each case here. The singular vectors are functions of model depth, so the model at which they were calculated (the “true” model in this case) is plotted next to them to pick out features associated with the model. Lastly, just as Figure 5.11 showed the unregularized spectra in gray and the regularized spectra in black, here

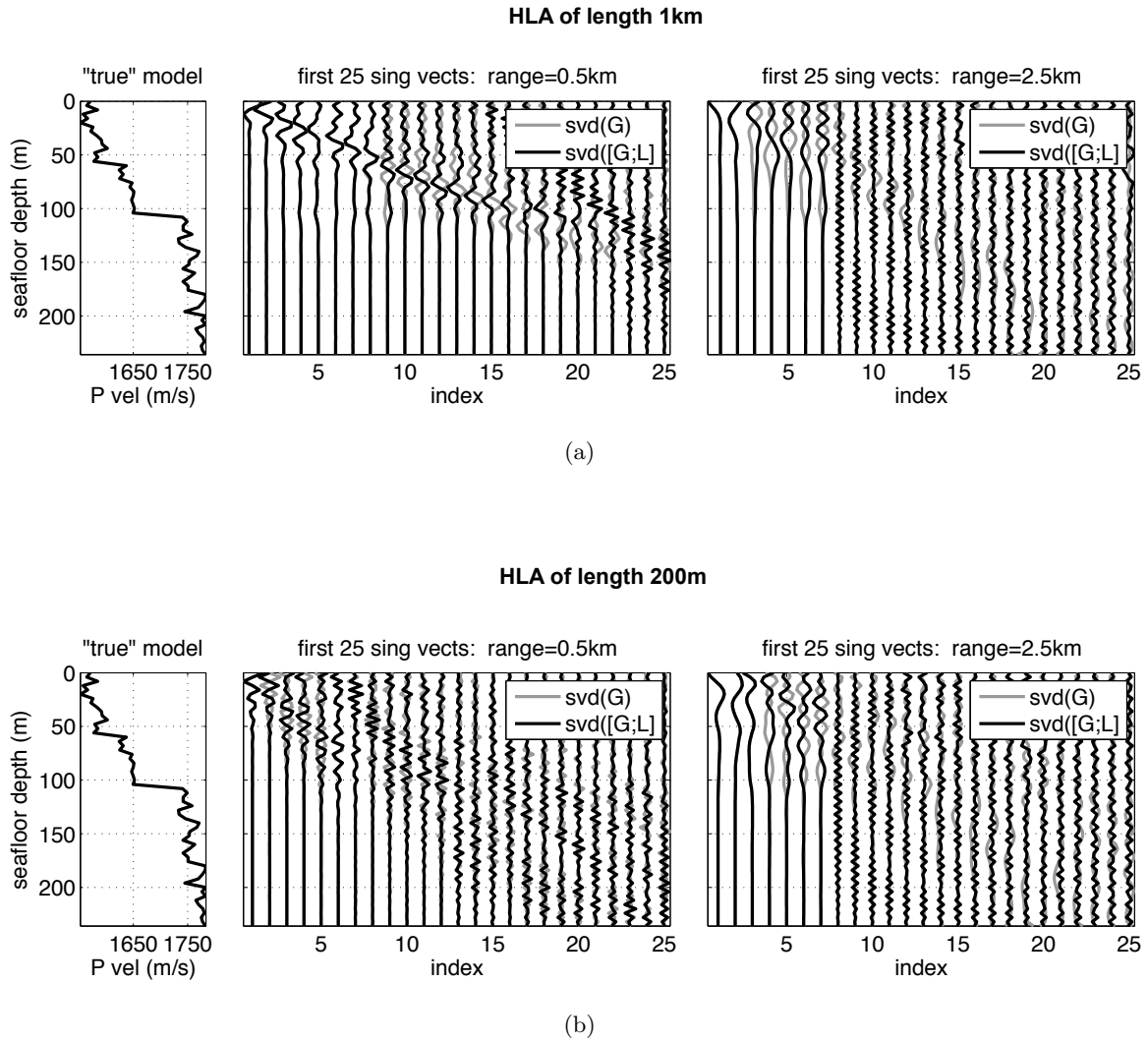


Figure 5.12: Singular vectors corresponding to the (a) 1km and (b) 200m HLA problem geometries in Figure 5.11, for ranges of 0.5km and 2.5km, and a source depth of 5m. The index axes correspond to the indices on the x axes of Figure 5.11, and the y axis in all components of this figure is the seafloor depth as labeled at left. The gray singular vectors are for the unregularized problem; the black spectra are for the regularized problem. The “true” bottom model is $\text{btm}\#1$ and the ocean depth was 200m.

too the corresponding unregularized and regularized singular vectors are shown in gray and black respectively.

The four plots in Figure 5.12 – for short and long HLAs, at short and long ranges – show two main features initially. First, there is a difference in the look of the singular vectors between at short and long ranges, which look somewhat the same between the two HLAs at the long ranges, but starkly different between the HLAs at the short ranges. Second, at short range, the difference between the singular vectors for the two HLAs might be described as “structured” for the long HLA and “unstructured” for the short one. Other features in these singular vector plots will be discussed momentarily.

Just as the singular value spectra in Figure 5.11 showed a drop in slope (less weighting of the higher-index singular vectors) with increasing range, there is a drop in structure in higher-index singular vectors with increasing range in Figure 5.12a. The short-range singular vectors in Figure 5.12b have almost no structure at all, looking essentially like noise because the short HLA was not able to resolve the bottom model at short ranges. The structure in the singular vectors of Figure 5.12a at short range show more specific information.

Note the depth correspondence to the indices of the singular vectors in Figure 5.12a, i.e. the more singular vectors included the deeper the model is resolved (up to a certain limit in the index, after which things get more complicated, albeit with much subtler effect given the smaller corresponding singular values). Comparing the bottom model plot with the short-range singular vectors in this figure, one sees that the regularization did not change the fact that the first eight singular vectors resolved the structure down to the first of the two large discontinuities (i.e. at about 55m and 105m). Then the regularization did have an effect in resolving the structure between those two large discontinuities, and then deeper than the 105m discontinuity, the structure in the singular vectors changes again and resolving the model is somewhat less straightforward (although as seen in Figure 5.6 and 5.7 the model is in fact resolved down there, to a lesser extent).

Similarly at long range in Figure 5.12a, in the first seven non-noisy singular vectors structure above the 55m discontinuity is resolved more finely than that below it, and then below the 105m discontinuity little is resolved at all, which matches the result seen in the averaging kernel plots in Figure 5.6. At this range (for both long and short HLAs), almost all the singular vectors were affected by the regularization, unlike the short-range case for

the long HLA in which the model above the 55m discontinuity could be resolved regardless of the regularization.

That the resolution of model features and the effects of regularization are dependent on position above, between, and below model discontinuities is readily considered in the intuition of the seismologist or acoustician. But to quantify and verify these phenomena via SVD like this can be a powerful aid to problem interpretation and planning.

5.4 Monte Carlo analysis to examine where linear approximations of resolution and uncertainty are valid and invalid

The linear approximations to the uncertainty and resolution used thus far have their limits in this nonlinear inverse problem, and it is prudent to explore where the linear approximations break down, and how they break down, in the problem. Recall that even if the linearized inversion method successfully finds the solution in the nonlinear problem, the linear approximation assumes the shape of the objective surface (which directly affects the model uncertainty and resolution) is a paraboloid, giving ellipsoidal error bounds. This approximation of the objective surface shape matches the true nonlinear problem's objective surface shape well in some neighborhood of the solution point, but diverges from it with increasing distance from the solution, in other words with increasing model uncertainty.

An ideal (but slow) tool for investigating nonlinear objective surfaces and problems is Monte Carlo analysis. Section 3.1 clarified the use of a frequentist inversion approach in this work and its distinction from a Bayesian one – while Monte Carlo methods are perhaps more popularly used in Bayesian inversions, they can also be used in the frequentist framework to analyze the effects of the non-paraboloidal objective surface. In this synthetic inverse problem, the random noise added to the synthetic data is recreated N times for N Monte Carlo runs, and the inverse problem is solved N times. Similarly for an inversion of real-world experiment data, the N instantiations of random noise on the data can be produced by bootstrapping the noise in the real data (estimated by subtracting the data predicted by the inversion from the measured data); correlated noise can be blocked-bootstrapped. Then the inversion can be solved N times in that case as well.

Figure 5.13a shows 71 Monte Carlo solutions to the previously discussed VLA synthetic inverse problem for source depth 5m and range 1.5km, again using the “true” bottom model btm#1 (Figure 5.15). Only 71 Monte Carlo runs were computed here because the inversion computations were very time consuming (more so for this 240m deep model than for the 120m deep model in the Monte Carlo analysis in Section 4.3); so the estimates of model standard deviations here are somewhat less accurate than those in Chapter 4, but

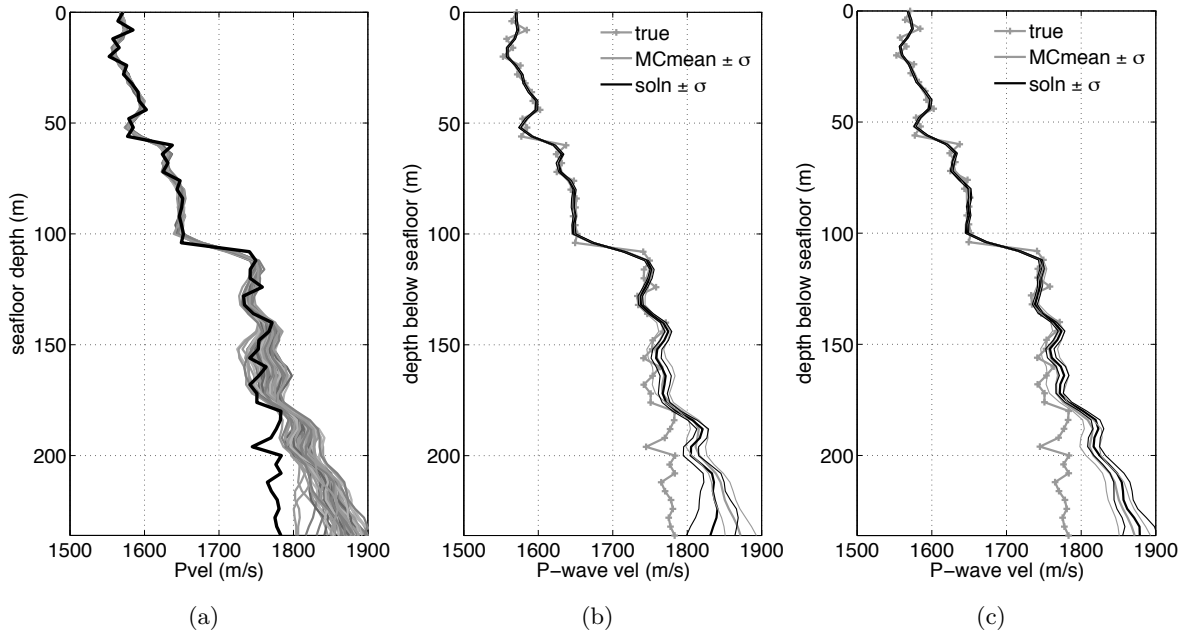


Figure 5.13: Monte Carlo solutions ($N=71$) of the Chapter 5 VLA problem given new random instantiations of data noise. Source depth is 5m and range is 1.5km, using the 240m-deep “true” bottom model of btm#1 (Figure 5.15). The ocean depth was 200m. There are 71 Monte Carlo solutions shown in (a), corresponding to 71 instantiations of the random noise on the synthetic data. The gray profiles are the Monte Carlo solutions and the jagged black profile is the “true” bottom model for comparison. In (b) and (c), just the first two Monte Carlo solutions (respectively) of (a) are shown, here with their standard deviations in dashed lines for discussion in the text of where the linear approximation to model uncertainty breaks down. The lightest-gray solid curves in (b) and (c) depict $\mathbf{Rm}_{\text{true}}$, i.e. the smoothed versions of the true model for each solution (recall that \mathbf{R} is solution-dependent). It is these smoothed true models that the inversion solutions estimate. These results are directly comparable to the analogous ones for the Chapter 4 problem in Figure 4.13, except that the bias seen here was not seen at the bottom of Chapter 4’s results.

still these samples still give useful information about patterns in where and how the linear approximation of the model uncertainty and resolution break down.

The smooth gray profiles in Figure 5.13a are the Monte Carlo solutions and the jagged black profile is the “true” bottom model for reference – recall however it is the smoothed version of this true bottom model that those Monte Carlo solutions are estimating.

There is a bias of these Monte Carlo solutions below depths of about 150m, in contrast to the earlier Monte Carlo example in Figure 4.13 in Section 4.3. However, the depth span of this bias coincides with the poor resolution at the bottom of the model depths in Figures 5.9 and 5.10; there is little information about the model at those depths present in the data. Figures 5.13b and 5.13c show comparisons of the linearly approximated model standard deviations to the actual standard deviations estimated from the Monte Carlo samples, also analogously to Figure 4.13. But do note when comparing this figure to Figure 4.13 that the true model is different in the two cases – not only is the depth of the model deeper here in Chapter 5, but the discontinuities are not at the same place.

In both the Monte Carlo and linear cases, note that standard deviations are not the entirety of the second moment of the solution statistics – there are also correlations over model depth in those statistics which are not depicted in these plots and which can affect the correct interpretation of the uncertainty. Neglecting the correlations can potentially cause underestimation of the model uncertainty, even if the Monte Carlo shows the linear approximation to the uncertainty is reasonable.

There are other effects that the Monte Carlo analysis shows regarding the limits of the linear description of the solution statistics. The uncertainty and resolution of the solution are inherently linked, so those effects in the model solution uncertainty also show up in the model solution resolution. It has been stated already that the frequentist inversion process here estimates a smoothed version of the true model, and that this smoothed true model is solution dependent since it is equal to $\mathbf{R}\mathbf{m}_{\text{true}}$ (in which the \mathbf{R} is solution dependent). Thus, many Monte Carlo solutions means there will also be many of these smoothed true models, and it is useful to note their spread too if one is to correctly interpret the model solutions. Figure 5.14a shows $\mathbf{R}\mathbf{m}_{\text{true}}$ for the same 71 Monte Carlo runs as depicted in Figure 5.13a, and in this case the result shows that the spread in smoothed true models being estimated is small. Figure 5.14b similarly shows the averaging kernels for those 71 Monte Carlo solutions overlaid on top of each other. Just as the nonlinear aspects in the model uncertainties and smoothed true models became apparent below about 150m depth, the averaging kernels increasingly spread out with depth below 150m. That is, above that depth the resolution is consistently represented by the averaging kernels, whereas increasingly below 150m the

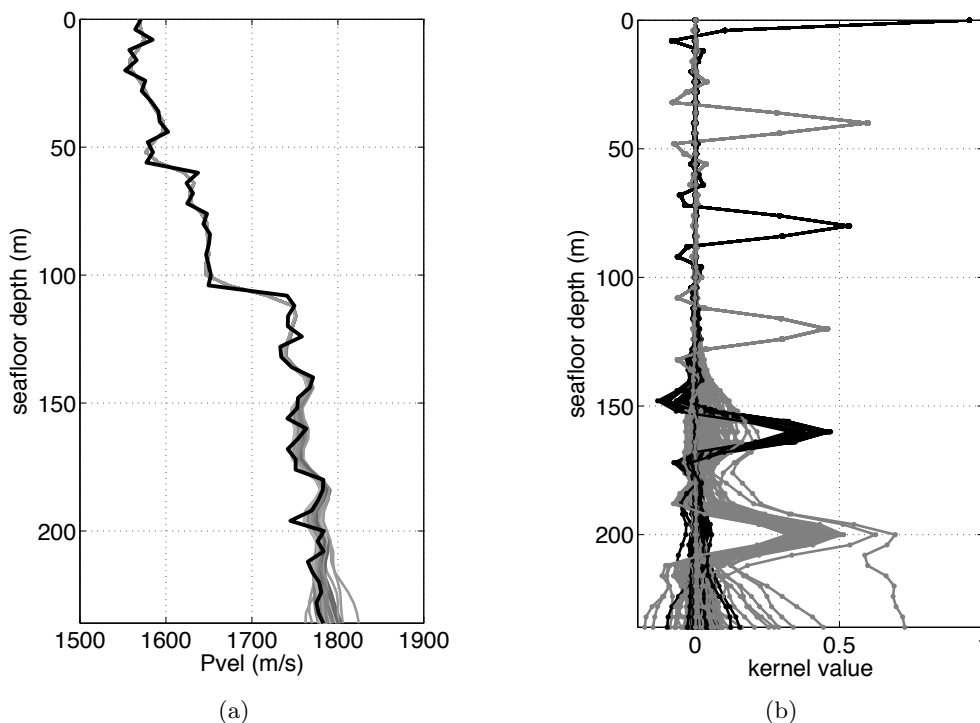


Figure 5.14: Monte Carlo estimates of (a) smoothed true models $\mathbf{Rm}_{\text{true}}$ and (b) averaging kernels for the VLA problem with source depth 5m and range 1.5km, corresponding to the 71 Monte Carlo solutions shown in Figure 5.13. These results are similar and directly comparable to the analogous ones for the Chapter 4 problem in Figure 4.14; note the depth spans are different but the kernel widths are about the same in both cases.

averaging kernels smear out, showing that the true resolution of the nonlinear problem is greater than that reported by individual inverse solutions.

There were poor-resolution features in this same depth region in the averaging kernels in Figure 5.10, but not in those in Figure 5.8 (focusing on the averaging kernels at 5m source depth and 1.5km range to match the above Monte Carlo problem). As described earlier, the results in Figure 5.10 were calculated from Jacobian matrices at the inverse problem solutions, while the results in Figure 5.8 were calculated from Jacobian matrices at the true model, very nearby in the model space. The averaging kernels at 200m in both these figures matched similar ones seen at 200m in both Figure 5.14b – in the Monte Carlo analysis the differences were caused by random variation in the noise that led to small variations in

model solutions analogous to the difference between true model and inversion solution in Figures 5.10 and 5.8.

As in Section 4.3.3, while the linearly approximated model standard deviations are comparable to the actual ones as estimated by Monte Carlo, and there is very little variation in the smoothed true model due to the nonlinearity, the nonlinearity causes a region of stronger sensitivity of the model resolution to the location in model space at the bottom of the model profile. So when using a linear resolution analysis to plan an experiment, it is useful to be aware of this region – while just a handful of Monte Carlo runs would not be able to give much useful statistical information, it may still provide some useful information about where these nonlinear issues arise. On the other hand, if one can compute enough Monte Carlo runs then one can check that the apparent bias in the single solution (relative to the true model) really is a bias, rather than simply attributable to a poor estimate of model uncertainty around that solution via the linear approximation.

Additionally, unlike the case in Chapter 4, here there was also a bias in the solution from the true model due to the nonlinearity in the portion of the model with the least sensitivity to the data, smaller than that in Chapter 4 due to the doubly deep model. This suggests an interesting trade-off between mitigating resolution artifacts due to non-negligible derivatives at bottom of the model (as discussed in Section 4.3.2) and bias in the inversion solution at the bottom of the model. Lastly, it is also helpful to notice that while there was bias in the model solution, and variability in the averaging kernels at the deepest portion of the model, there appears to be little or no bias in the *locations* of those averaging kernels.

Finally, the same effect of low velocity zones (LVZs) was seen in these Monte Carlo examples as in the ones in Section 4.3.3 – there is a correspondence between the especially poor resolution kernels in Figure 5.14b and Monte Carlo solutions with LVZs at their bases in Figure 5.13a. In other words, as seen earlier, this resolution analysis has its main shortcomings with the presence of LVZs in the model.

5.5 Results compared between different candidate bottom profiles

Since the geoacoustic inversion investigated in this thesis is a nonlinear inverse problem, the uncertainty and resolution results are dependent on the bottom model. This means

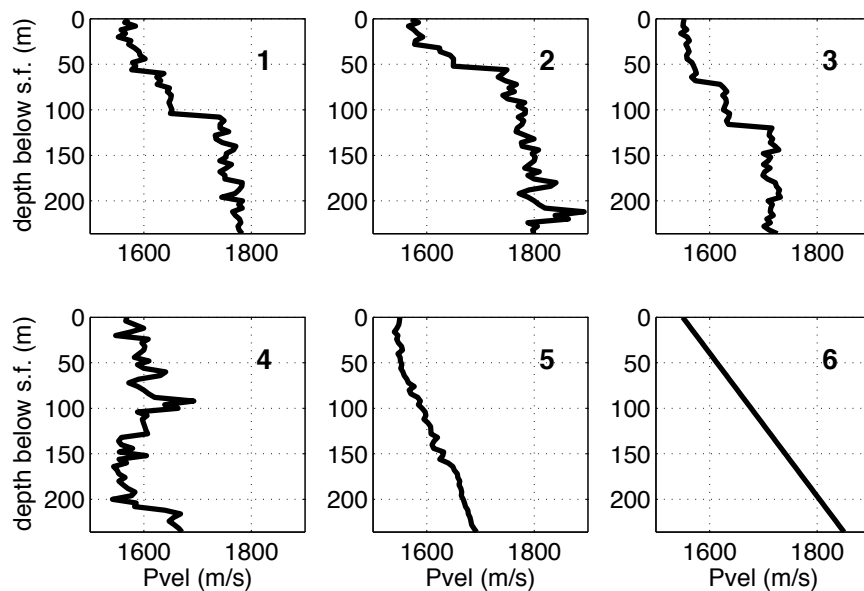


Figure 5.15: Six different bottom model profiles used to compare effects of “true” model on the resolution results. Btm#1 is used extensively in earlier sections of this chapter and in previous chapters.

that all the results considered previously in this chapter for the one bottom model (which was chosen to help demonstrate various features of the analysis) may be different for other choices of bottom model. If this is an analysis done before the experiment, then the true bottom model is in fact unknown, or at least not well known if other *a priori* information was available. So is any of this analysis still valid? How is the analysis affected by this significant issue, as a function of how well the bottom model may be known *a priori*?

That is an enormously rich question, and as with many nonlinear geophysical inverse problems a fully comprehensive answer may not be feasible. However, the focus of this chapter is the practical interest in planning a geoacoustic experiment, so to that end an empirical approach is taken here, to consider these questions generally regarding the resolution analysis and to show that it does in fact still have merit. Six example “true” bottom model profiles of varying similarity are run through the resolution analysis and results are compared between them. These six bottom models are shown in Figure 5.15. The first model profile is the “btm#1” model used extensively to this point; the second

and third model profiles are variants of it in the sense of different random variations in P-wave velocity between two discontinuities at differing depths. The expectation is that these three conceptually similar profiles might produce similar resolution results, as a way to consider the case of knowing some *a priori* information about the bottom such as “two main discontinuities based on nearby sub-bottom profiler results” and guesstimates at average velocities between discontinuities, perhaps based on a previous experiment or core samples in a nearby region. The fourth model profile has a simple constant gradient and approximates the endpoints of the first two model profiles. The fifth and sixth are based on two real-world bottom profiles taken from Ocean Drilling Project data [69], albeit filtered and resampled, to provide realistic but completely different example model profiles. The fifth is gently varying with a lesser and almost-constant gradient approximating that between the endpoints of model profile three; this model also notably has a velocity in the surficial 85m that is less than that at the bottom of the water column. The sixth model is strongly varying but with an even smaller gradient overall.

Figure 5.16 shows overlaid resolution results for the same VLA problem as in Figure 5.8, discussed in Section 5.2.1, here reduced to resolution diagonal curves (which were introduced in Section 5.1.2 and demonstrated in Figures 5.3 and 5.4). Unlike Figure 5.8 which was based only on btm#1, here the results are based on all six of the “true” bottom models in Figure 5.15 and overlaid for comparison. These are for the single-VLA problem as a function of depth, source range, and two source depths, computed from complete synthetic inversions with a 40-hydrophone VLA spanning the water column. The ocean depth was 200m. This figure is admittedly a busy one; zooms of this figure with call-outs labeling which resolution diagonal is associated with which bottom model are shown in Figure 5.17. But the goal of this busy figure is to show the resolution results from each of the six “true” bottom models relative to each other, to gauge similarity and contrasts.

The poor short-range results show the same stability troubles discussed in Section 5.2 for all the “true” models. More information about how these stability troubles manifest themselves in the inverse solutions can be seen in the averaging kernels (as in Figure 5.8 for btm#1); here the plots are used to simply note where the stability trouble is.

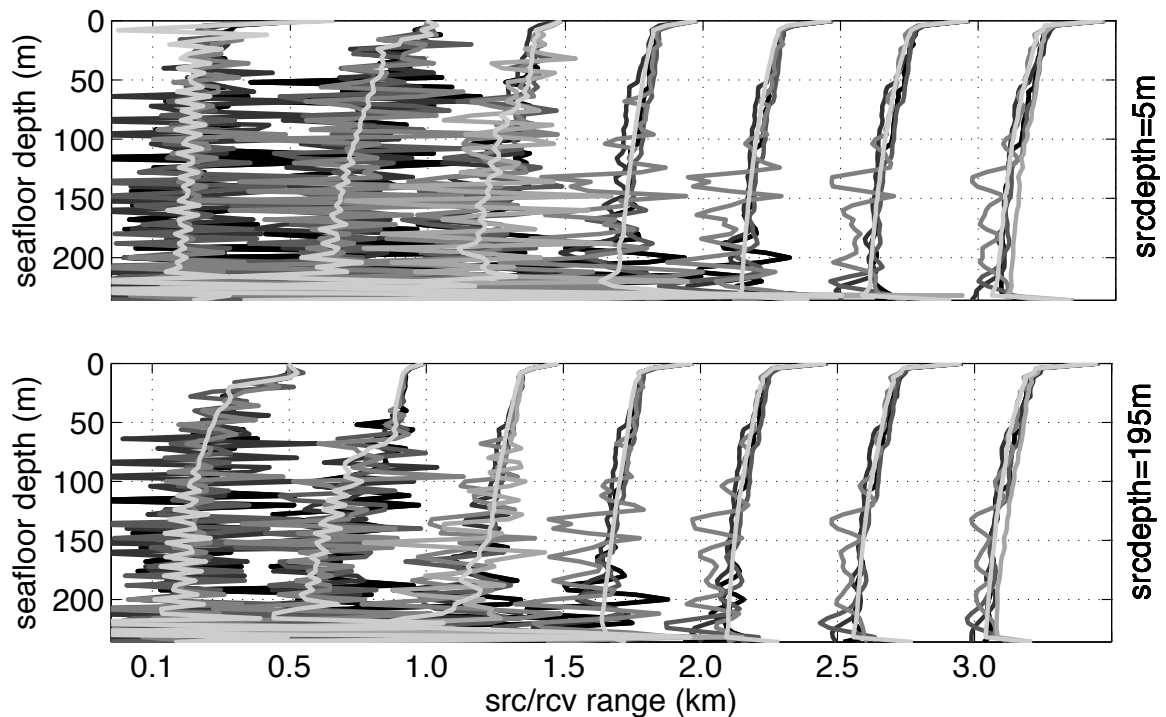


Figure 5.16: Overlaid resolution diagonals for six different bottom model profiles in the VLA problem, for two source depths, for the same problem as in Figure 5.8. The six shades of gray represent the six bottom models in order (darkest first), but without intention of the reader actually distinguishing the individual shades here – two zooms of this figure are shown in Figure 5.17 with explicit callouts labeling the bottom model for each curve.

Overall, the key point to the figure is that the six bottom models yield broadly similar resolution results, both in terms of where the stability trouble comes into play and how the resolution falls off with model depth and source range. The six “true” bottom models all show similar enough results that one would likely draw the same conclusions about experiment geometry planning from any of them in this problem, while their differences are discussed below. The curves are colored in a gray scale in order of the “true” bottom models numbered in Figure 5.15, with darkest first, and in this figure show that the most similar “true” bottoms (the first three) yield the most similar resolution results as well. This is more readily seen in the zooms in Figure 5.17.

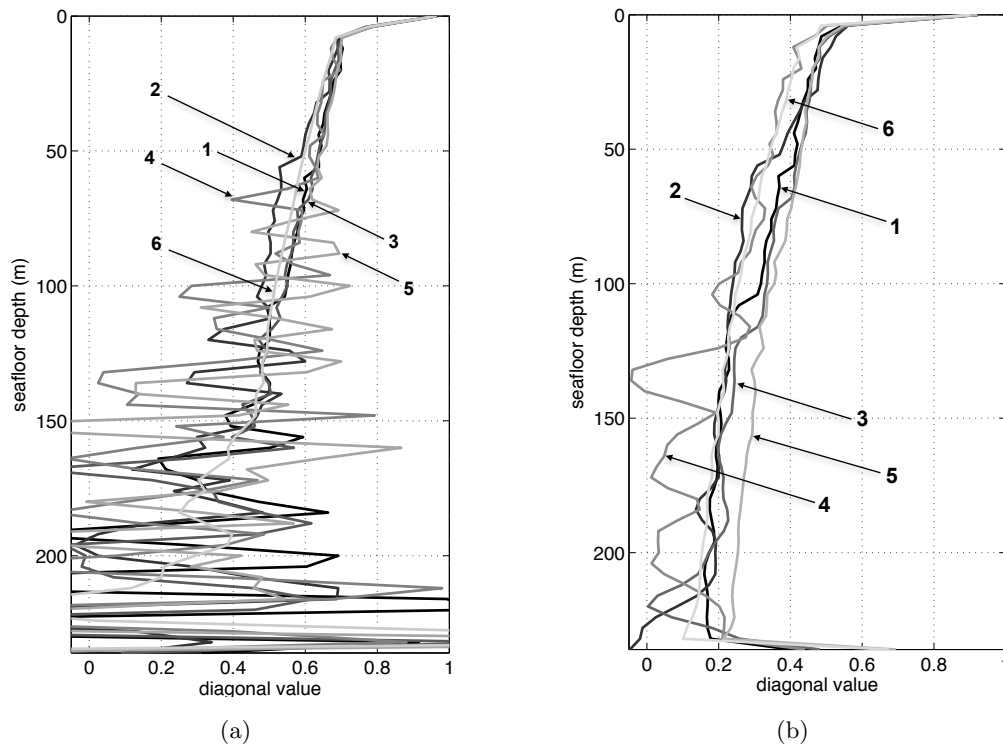


Figure 5.17: Zoom and labeling of two of the overlaid resolution diagonal plots in Figure 5.16. These plots are for (a) source depth 195m at range 1.0km and (b) source depth 5m at range 3.0km in that figure. The labeled numbers correspond to the “true” bottom models 1-6 shown in Figure 5.15.

The zoomed-in plots in Figure 5.17 show the resolution diagonal results more closely for just the 1.0km (5.17a) and 3.0km (5.17b) ranges at 195m source depth. The labeled numbers correspond to the “true” bottom models 1-6 shown in Figure 5.15. At farther range (5.17b) the first four and the sixth bottom models show similar resolution results down to about 130m depth, below which btm #4 has virtually no resolution at all due to its LVZ there (see Figure 5.15). Bottom #5 shows better resolution than all the others overall, due to its softer gradient at shallower depths as well as its sub-water velocity at those shallow depths, both of which cause more rays to return at farther range, i.e. nearer the 3.0km range of Figure 5.17b.

At short range (5.17a), the stability trouble is evident in the results from all six bottom models. The more-similar bottom models 1-4 and 6 behave similarly here too in terms of

value of the resolution diagonal at shallower depths where they are well-behaved and the depth at which the stability difficulties begin (approximately 100m). Btm #5 on the other hand has stability difficulties at all depths at this range under the same regularization for the same reason that its resolution is better than the others at farther range – the bulk of its sensitivity (and of its returning rays) is focused at farther range so that its sensitivity at closer range is reduced at closer range.

At both short and long ranges, the conclusion from the above is that the similar “true” bottom models have similar resolution results; thus if one knows more about the bottom *a priori* then one can narrow down the span of candidate bottoms explored in a pre-experiment resolution analysis. This particularly comes into play with respect to the effects of LVZs as seen in the previous section. If one knows either that no significant LVZs exist in the bottom of interest, or at what depths those LVZ are, then one can either have confidence in the results of the linearly-based resolution analysis or know where to be cautious of the results as one designs the experiment.

5.6 Summary and conclusions

In summary then, this chapter has analyzed the results and uses of a resolution analysis of our continuous geoaoustic inverse problem. The focus has been on a linearized analysis, but with an additional Monte Carlo investigation to consider the limits of where that approximation of local linearity is invalid. Advantages and disadvantages of different views into the linearized resolution results were reviewed. The most quantitative of these views, the averaging kernel plots, were used to look at the resolution of synthetic inversion results as a function of experiment geometry. The effects of the problem regularization on that resolution, as distinguished from the range effects, were seen in the singular value spectra and singular vectors of the locally linearized problem. The sensitivity of conclusions in experiment geometry planning based on this resolution analysis to variations in the unknown (or partially-known) “true” bottom model was explored using six different bottom models.

These techniques and conclusions are appropriate when inverting for velocity profiles in scenarios related to the demonstration problem of this chapter – shallow (200m) water, relatively short (≤ 3 km) range, flat bottom. The focus in this work was one-dimensional

bottom profiles of a predominantly sand-based composition, as opposed to including strongly elastic components; this was purely a constraint of the Hamilton regressions used to narrow the problem and does constitute additional *a priori* information about the bottom model.

Of the three levels of summarization of the linearized resolution results, the averaging kernels were seen to be the most complete and reliable view. The resolution-diagonals and the trace plots each had issues that required the user to verify the domains of validity of the diagonals and trace plots by use of the averaging kernel plots. However, these plots still have their uses even with that caveat, as demonstrated by Section 5.5.

There were hints that a deeper source is better in this synthetic analysis but was not as strong a factor as the other issues.

Perhaps the most functional demonstration of the chapter was the comparison of the resolution results for different receiver array configurations and lengths. Regardless of the “true” bottom model used to compute the resolution results, at ranges $> 1.5\text{km}$ in this problem the VLA and either the 200m- or the 1km-long HLA were seen as equivalent in terms of providing the same resolution in the inversion results. But at shorter ranges, $< 1.5\text{km}$, the 1km HLA or several VLAs were clearly better. In other words, distributing the array receivers was certainly advantageous at shorter ranges, and not particularly disadvantageous at longer ranges. With appropriate choices of receiver arrays, as might be expected the resolution of the bottom model improved dramatically with decreasing range. Note one could choose an array configuration and experiment geometry based on other information in the analysis as well however, such as the quantitative estimates of resolution of the actual inversion solutions expected when that experiment data is inverted.

Results in the Monte Carlo analysis as well as the comparison over different “true” bottoms highlighted the role that LVZs have as a limiter of this resolution analysis. While the analysis overall behaves essentially linearly (as long as one operates within the local minimum of the solution to avoid cycle skipping), the exception to this is that the analysis is highly sensitive to LVZs. The LVZs prevent acoustic energy from returning to the receivers, thus the data have no sensitivity to the bottom model in the LVZ, and the resolution can drop off suddenly if one places an LVZ in the candidate “true” model being explored.

Variations in the resolution analysis results were compared across different candidate bottom models, but among the bottom models investigated here it was seen that the resolution analysis results were actually similar for even rather different bottom models. The exception again was the presence of an LVZ in the model, to which the resolution results were highly sensitive. If even just some information is known *a priori* about the bottom, perhaps from a core sample or previous experiment in the area, the concern about LVZs might be better dealt with. But outside of this issue the analysis allows the practitioner to both devise experiment layout and quantitatively gauge the effects of regularization choices in the inversion. Overall the technique is encouraging for more quantitative experiment planning in the geoacoustic community in the future.

BIBLIOGRAPHY

- [1] R. K Andrew, B. M Howe, and J. A Mercer. Long-time trends in ship traffic noise for four sites off the north american west coast. *The Journal of the Acoustical Society of America*, 129(2):642651, 2011.
- [2] R. K Andrew, M. R Zarnetske, B. M Howe, and J. A Mercer. Ship-Suspended acoustical transmitter position estimation and motion compensation. *Oceanic Engineering, IEEE Journal of*, 35(4):797810, 2010.
- [3] R. C. Aster, B. Borchers, and C. H. Thurber. *Parameter Estimation and Inverse Problems*. Academic Press, San Diego, 2005.
- [4] G. Backus and F. Gilbert. Uniqueness in the inversion of inaccurate gross earth data. *Philosophical Transactions of the Royal Society of London. Series A, Mathematical and Physical Sciences (1934-1990)*, 266(1173):123–192, 1970.
- [5] N. Barth and C. Wunsch. Oceanographic experiment design by simulated annealing. *Journal of Physical Oceanography*, 20:1249–1263, 1990.
- [6] K. M. Becker, S. D. Rajan, G. V. Frisk, and W. H. O. Instn. Results from the geoacoustic inversion techniques workshop using modal inverse methods. *Oceanic Engineering, IEEE Journal of*, 28(3):331–341, 2003.
- [7] Kyle M Becker and George V Frisk. The impact of water column variability on horizontal wave number estimation and mode based geoacoustic inversion results. *Journal of the Acoustical Society of America*, 123(2):658, 2008.
- [8] Ebru Bozdag, Jeannot Trampert, and Jeroen Tromp. Misfit functions for full waveform inversion based on instantaneous phase and envelope measurements. *Geophysical Journal International*, (185):845–870, 2011.
- [9] D. M.F Chapman. What are we inverting for? In *Inverse problems in underwater acoustics*, page 114. Springer-Verlag, New York, 2001.
- [10] N. R. Chapman and L. Jaschke. Freeze bath inversion for estimation of geoacoustic parameters. In *Inverse Problems in Underwater Acoustics*, pages 15–35. Springer-Verlag, New York, 2001.
- [11] Darrell Coles and A Curtis. Efficient nonlinear Bayesian survey design using DN optimization. *Geophysics*, 76(2):Q1–Q8, 2011.

- [12] A. Curtis. Optimal experiment design: cross-borehole tomographic examples. *Geophys. J. Int.*, 136:637–650, 1999.
- [13] A. Curtis and R. Snieder. Reconditioning inverse problems using the genetic algorithm and revised parameterization. *Geophysics*, 62:1524–1532, 1997.
- [14] Andrew Curtis and Hansruedi Maurer. Optimizing the design of geophysical experiments: Is it worthwhile? *The Leading Edge*, 19(10):1058–1062, 2000.
- [15] F. A. Dahlen, S. H. Hung, and G. Nolet. Frechet kernels for finite-frequency traveltimes-I. theory. *Geophys. J. Int.*, 141(1):157–174, 2000.
- [16] Jan Dettmer, Stan E. Dosso, and Charles W. Holland. Model selection and bayesian inference for high-resolution seabed reflection inversion. *The Journal of the Acoustical Society of America*, 125(2):706–716, February 2009.
- [17] S. E. Dosso. Quantifying uncertainty in geoacoustic inversion. i. a fast gibbs sampler approach. *The Journal of the Acoustical Society of America*, 111:129, 2002.
- [18] S. E. Dosso and P. L. Nielsen. Quantifying uncertainty in geoacoustic inversion. II. application to broadband, shallow-water data. *The Journal of the Acoustical Society of America*, 111:143, 2002.
- [19] S. E. Dosso, P. L. Nielsen, and M. J. Wilmut. Data error covariance in matched-field geoacoustic inversion. *The Journal of the Acoustical Society of America*, 119:208, 2006.
- [20] S. E. Dosso and M. J. Wilmut. Quantifying data information content in geoacoustic inversion. *Oceanic Engineering, IEEE Journal of*, 27(2):296–304, 2002.
- [21] S. E. Dosso, M. L. Jeremy, J. M. Ozard, and N. R. Chapman. Estimation of ocean-bottom properties by matched-field inversion of acoustic field data. *IEEE Journal of Oceanic Engineering*, 18(3):232–239, July 1993.
- [22] M. R. Fallat, P. L. Nielsen, S. E. Dosso, and M. Siderius. Geoacoustic characterization of a range-dependent ocean environment using towed array data. *IEEE Journal of Oceanic Engineering*, 30(1):198–206, January 2005.
- [23] P. Gerstoft. Inversion of acoustic data using a combination of genetic algorithms and the GaussNewton approach. *The Journal of the Acoustical Society of America*, 97:2181, 1995.
- [24] Philip E. Gill, Walter Murray, and Margaret H. Wright. *Practical optimization*. Academic Press, 1981.

- [25] G. H. Golub and C. F. Van Loan. *Matrix Computation*. The Johns Hopkins University Press Baltimore, 1996.
- [26] David Gubbins. *Time series analysis and inverse theory for geophysicists*. Cambridge University Press, 2004.
- [27] Edwin L Hamilton. Sound attenuation as a function of depth in the sea floor. *Journal of the Acoustical Society of America*, 59(3):528–535, 1976.
- [28] Edwin L. Hamilton. Sound velocity–density relations in sea-floor sediments and rocks. *The Journal of the Acoustical Society of America*, 63(2):366–377, February 1978.
- [29] Edwin L. Hamilton. Vp/Vs and poisson’s ratios in marine sediments and rocks. *The Journal of the Acoustical Society of America*, 66(4):1093–1101, October 1979.
- [30] Per Christian Hansen. *Rank-Deficient and Discrete Ill-Posed Problems: Numerical Aspects of Linear Inversion*. Society for Industrial Mathematics, January 1987.
- [31] F. S Henyey, Kevin L Williams, Jie Yang, and Dajun Tang. Simultaneous Nearby Measurements of Acoustic Propagation and High-Resolution Sound-Speed Structure Containing Internal Waves. *Oceanic Engineering, IEEE Journal of*, 35:684–694, 2010.
- [32] Chen-Fen Huang, Peter Gerstoft, and William S. Hodgkiss. Uncertainty analysis in matched-field geoacoustic inversions. *The Journal of the Acoustical Society of America*, 119(1):197–207, January 2006.
- [33] Chen-Fen Huang, Peter Gerstoft, and William S Hodgkiss. Effect of ocean sound speed uncertainty on matched-field geoacoustic inversion. *Journal of the Acoustical Society of America*, 123(6):EL162, 2008.
- [34] F. B. Jensen, W.A. Kuperman, M.B. Porter, and H. Schmidt. *Computational Ocean Acoustics*. Amer Inst of Physics, New York, 1994.
- [35] Yong-Min Jiang and N. Ross Chapman. Bayesian geoacoustic inversion in a dynamic shallow water environment. *The Journal of the Acoustical Society of America*, 123(6):EL155–EL161, June 2008.
- [36] Yong-Min Jiang and N Ross Chapman. The impact of ocean sound speed variability on the uncertainty of geoacoustic parameter estimates. *Journal of the Acoustical Society of America*, 125(5):2881, 2009.
- [37] Yong-Min Jiang, N. Ross Chapman, and Mohsen Badiy. Quantifying the uncertainty of geoacoustic parameter estimates for the new jersey shelf by inverting air gun data. *The Journal of the Acoustical Society of America*, 121(4):1879–1894, April 2007.

- [38] Yongmin Jiang, N. Ross Chapman, and Harry A. DeFerrari. Geoacoustic inversion of broadband data by matched beam processing. *The Journal of the Acoustical Society of America*, 119(6):3707–3716, June 2006.
- [39] Zhenglin Li, Renhe Zhang, Jin Yan, Fenghua Li, and Jianjun Liu. Geoacoustic inversion by matched-field processing combined with vertical reflection coefficients and vertical correlation. *Oceanic Engineering, IEEE Journal of*, 29:973–979, 2004.
- [40] Y T Lin, C F Chen, and James F Lynch. An Equivalent Transform Method for Evaluating the Effect of Water-Column Mismatch on Geoacoustic Inversion. *Oceanic Engineering, IEEE Journal of*, 31(2):284–298, April 2006.
- [41] Y. Luo and G. T. Schuster. Wave-equation travelttime inversion. *Geophysics*, 56(5):645–653, 1991.
- [42] Yi Luo and Gerard T. Schuster. Wave-equation travelttime + waveform inversion. *SEG Technical Program Expanded Abstracts*, 9(1):1223–1225, 1990.
- [43] James F. Lynch, Subramaniam D. Rajan, and George V. Frisk. A comparison of broadband and narrow-band modal inversions for bottom geoacoustic properties at a site near corpus christi, texas. *The Journal of the Acoustical Society of America*, 89(2):648–665, February 1991.
- [44] Mark A. McDonald, John A. Hildebrand, Sean M. Wiggins, and Donald Ross. A 50-year comparison of ambient ocean noise near san clemente island: A bathymetrically complex coastal region off southern california. *The Journal of the Acoustical Society of America*, 124(4):1985, 2008.
- [45] Steven L Means and Martin Siderius. Effects of sea-surface conditions on passive fathometry and bottom characterization. *The Journal of the Acoustical Society of America*, 126(5):2234–2241, November 2009. PMID: 19894804.
- [46] W. Menke. *Geophysical Data Analysis: Discrete Inverse Theory*. Academic Press, San Diego, 1989.
- [47] K. Mosegaard. Resolution analysis of general inverse problems through inverse monte carlo sampling. *Inverse Problems*, 14:405–426, 1998.
- [48] Michael Nicholas, John S Perkins, Gregory J Orris, and Laurie T Fialkowski. Environmental inversion and matched-field tracking with a surface ship and an L-shaped receiver array. *Journal of the Acoustical Society of America*, 116:2891–2901, 2004.
- [49] R. L. Parker. *Geophysical Inverse Theory*. Princeton University Press, Princeton, 1994.

- [50] G. R. Potty and J. H. Miller. Geoacoustic tomography: Range dependent inversions on a single slice. *J. Comput. Acoust*, 8(2):325345, 2000.
- [51] G. R. Potty and J. H. Miller. Nonlinear optimization techniques for geoacoustic tomography. *Inverse Problems in Underwater Acoustics*, 2001.
- [52] G. R. Potty, J. H. Miller, P. H. Dahl, and C. J. Lazauski. Geoacoustic inversion results from the ASIAEX east china sea experiment. *Oceanic Engineering, IEEE Journal of*, 29(4):1000–1010, 2004.
- [53] G. R. Potty, J. H. Miller, J. F. Lynch, and K. B. Smith. Tomographic inversion for sediment parameters in shallow water. *The Journal of the Acoustical Society of America*, 108:973, 2000.
- [54] S. D. Rajan, J. F. Lynch, and G. V. Frisk. Perturbative inversion methods for obtaining bottom geoacoustic parameters in shallow water. *The Journal of the Acoustical Society of America*, 82:998, 1987.
- [55] Subramaniam D. Rajan. Determination of geoacoustic parameters of the ocean bottom—data requirements. *The Journal of the Acoustical Society of America*, 92(4):2126–2140, October 1992.
- [56] Subramaniam D. Rajan. Waveform inversion for the geoacoustic parameters of the ocean bottom. *The Journal of the Acoustical Society of America*, 91(6):3228–3241, June 1992.
- [57] Purnima Ratilal, Yisan Lai, Deanelle T. Symonds, Lilimar A. Ruhlmann, John R. Preston, Edward K. Scheer, Michael T. Garr, Charles W. Holland, John A. Goff, and Nicholas C. Makris. Long range acoustic imaging of the continental shelf environment: The acoustic clutter reconnaissance experiment 2001. *The Journal of the Acoustical Society of America*, 117(4):1977–1998, April 2005.
- [58] Z J Rawlinson, J Townend, R Arnold, and S Bannister. Derivation and implementation of a nonlinear experimental design criterion and its application to seismic network expansion at Kawerau geothermal field, New Zealand. *Geophysical Journal International*, (191):686–694, 2012.
- [59] Daniel Rouseff and Terry Ewart. Effect of random sea surface and bottom roughness on propagation in shallow water. *The Journal of the Acoustical Society of America*, 98(6):3397, 1995.
- [60] P. S. Routh, G. A. Oldenborger, and D. W. Oldenburg. Optimal survey design using the point spread function measure of resolution. *SEG Expanded Abstracts*, 24:1033–1036, 2005.

- [61] J. A Scales and L. Tenorio. Prior information and uncertainty in inverse problems. *Geophysics*, 66(2):389397, 2001.
- [62] H. Schmidt and A. B. Baggeroer. Physics-imposed resolution and robustness issues in seismo-acoustic parameter inversion. In *Full Field Inversion Methods in Ocean and Seismo-Acoustics*, Modern Approaches in Geophysics, pages 85–90. Kluwer Academic Publishers, Dordrecht, 1995.
- [63] H. Schmidt and F. B. Jensen. A full wave solution for propagation in multilayered viscoelastic media with application to gaussian beam reflection at fluid-solid interfaces. *The Journal of the Acoustical Society of America*, 77:813, 1985.
- [64] H. Schmidt and G. Tango. Efficient global matrix approach to the computation of synthetic seismograms. *J. Astron. Soc*, 84:331–359, 1986.
- [65] Martin Siderius, Peter L Nielsen, Jürgen Sellschopp, Mirjam Snellen, and Dick Simons. Experimental study of geo-acoustic inversion uncertainty due to ocean sound-speed fluctuations. *Journal of the Acoustical Society of America*, 110(2):769–781, 2001.
- [66] Mirjam Snellen, Dick G Simons, Martin Siderius, Jürgen Sellschopp, and Peter L Nielsen. An evaluation of the accuracy of shallow water matched field inversion results. *Journal of the Acoustical Society of America*, 109(2):514, 2001.
- [67] R. Snieder. An extension of Backus-Gilbert theory to nonlinear inverse problems. *Inverse Problems*, 7(3):409–433, 1991.
- [68] Roel Snieder. A perturbative analysis of non-linear inversion. *Geophysical Journal International*, 101:545–556, 1990.
- [69] K. Tamaki, K. Pisciotto, and J. Allan. Proceedings of the ocean drilling program, initial reports. volume 127. Ocean Drilling Program, College Station, TX, 1990.
- [70] A. Tarantola. A strategy for nonlinear elastic inversion of seismic reflection data. *Geophysics*, 51(10):1893–1903, 1986.
- [71] A. Tarantola. Inversion of travel times and seismic waveforms. *Seismic Tomography*, pages 135–157, 1987.
- [72] Albert Tarantola. *Inverse Problem Theory and Methods for Model Parameter Estimation*. SIAM: Society for Industrial and Applied Mathematics, Philadelphia, 2005.
- [73] Caglar Yardim, Peter Gerstoft, and William S Hodgkiss. Geoacoustic and source tracking using particle filtering: Experimental results. *Journal of the Acoustical Society of America*, 128:75–87, 2010.

- [74] C. Zhou, W. Cai, Y. Luo, G. T. Schuster, and S. Hassanzadeh. Acoustic wave equation traveltime and waveform inversion of crosshole seismic data. *Geophysics*, 60(3):765–773, 1995.
- [75] C. Zhou, G. T. Schuster, S. Hassanzadeh, and J. M. Harris. Elastic wave equation traveltime and waveform inversion of crosswell data. *Geophysics*, 62(3):853–868, 1997.
- [76] Ji-Xun Zhou, Xue-Zhen Zhang, Zhaohui Peng, and James S. Martin. Sea surface effect on shallow-water reverberation. *The Journal of the Acoustical Society of America*, 121(1):98, 2007.
- [77] Hejun Zhu, Ebru Bozdog, Daniel Peter, and Jeroen Tromp. Structure of the European upper mantle revealed by adjoint tomography. *Nature Geoscience*, 5:493–498, July 2012.

Appendix A

**GENERALIZED SINGULAR VALUE DECOMPOSITION
FORMULATION OF RESOLUTION**

This dissertation uses generalized singular value decomposition (GSVD), and a definition of the model resolution matrix derived from that decomposition, following the notation used in Aster et al. [3]. For convenience that definition and derivation are provided here in the Appendix.

A.1 Definition of generalized singular value decomposition

Linear or locally linearized problems regularized with “zeroth-order Tikhonov regularization” (sometimes called “ridge regression”), where $\mathbf{L} = \mathbf{I}$ in the generalized inverse of Eq. (3.21), can be decomposed with singular value decomposition (SVD). However in the general case where $\mathbf{L} \neq \mathbf{I}$ they cannot. There is a related decomposition applicable in that case, called the generalized singular value decomposition (GSVD), defined and applied below. Unfortunately, while the SVD has a standardized definition, the newer GSVD still has several different conventions. This dissertation uses the convention in Aster et al. [3]. Readers familiar with the SVD should note that \mathbf{U} and \mathbf{V} below are *not* the same as those in the SVD.

The GSVD decomposes the two matrices $\hat{\mathbf{G}}$ and \mathbf{L} simultaneously, such that:

$$\hat{\mathbf{G}} = \mathbf{U} \begin{bmatrix} \mathbf{\Lambda} & \mathbf{0} \\ \mathbf{0} & \mathbf{I} \end{bmatrix} \mathbf{X}^{-1} \quad (\text{A.1})$$

$$\mathbf{L} = \mathbf{V} \begin{bmatrix} \mathbf{M} & \mathbf{0} \end{bmatrix} \mathbf{X}^{-1} \quad (\text{A.2})$$

The dimensions of these various matrices are:

$$\hat{\mathbf{G}} : m \times n$$

$$\mathbf{L} : q \times n$$

$$\mathbf{U} : m \times n$$

$$\mathbf{V} : q \times q$$

$$\mathbf{X} : n \times n$$

$$\mathbf{\Lambda} : q \times q$$

$$\mathbf{M} : q \times q$$

Here $\hat{\mathbf{G}}$ and \mathbf{L} are from Eq. (3.21), m is the length of the data vector, n is the length of the model vector, q is the rank of \mathbf{L} , and $m \geq n \geq q$. The null spaces of $\hat{\mathbf{G}}$ and \mathbf{L} are assumed to only intersect at the zero vector. The $\mathbf{0}$'s and \mathbf{I} 's in Eq. (A.1) and Eq. (A.2) come into play when \mathbf{L} is not square; note the dimension of the \mathbf{I} in Eq. (A.1) and the $\mathbf{0}$ in Eq. (A.2) is $(n - q)$ by $(n - q)$, so that in the special case when \mathbf{L} is square they do not exist.

A.2 Derivation of the resolution matrix in terms of the GSVD

As presented in Aster et al. [3], using the GSVD one can rewrite Eq. (3.21) as:

$$\mathbf{G}^\dagger = \mathbf{X} \begin{bmatrix} \mathbf{\Lambda}^2 + \nu^2 \mathbf{M}^2 & \mathbf{0} \\ \mathbf{0} & \mathbf{I} \end{bmatrix}^{-1} \mathbf{X}^T \mathbf{X}^{-T} \begin{bmatrix} \mathbf{\Lambda}^T & \mathbf{0} \\ \mathbf{0} & \mathbf{I} \end{bmatrix} \mathbf{U}^T \quad (\text{A.3})$$

$$= \mathbf{X} \begin{bmatrix} \mathbf{F} \mathbf{\Lambda}^{-1} & \mathbf{0} \\ \mathbf{0} & \mathbf{I} \end{bmatrix} \mathbf{U}^T \quad (\text{A.4})$$

\mathbf{F} is defined as the diagonal matrix of filter factors for the Tikhonov regularization:

$$F_{i,i} = \frac{\gamma_i^2}{\gamma_i^2 + \nu^2}, \quad \gamma_i^2 = \frac{\lambda_i}{\mu_i} \quad (\text{A.5})$$

The λ_i are the diagonal elements of $\mathbf{\Lambda}$, with:

$$0 \leq \lambda_1 \leq \lambda_2 \leq \dots \leq \lambda_q \leq 1 \quad (\text{A.6})$$

and the μ_i are the diagonal elements of \mathbf{M} , with:

$$1 \geq \mu_1 \geq \mu_2 \geq \dots \geq \mu_q > 0 \quad (\text{A.7})$$

Using Eq. (3.23) and (A.3) the model resolution matrix can be written:

$$\mathbf{R} = \mathbf{X} \begin{bmatrix} \mathbf{F}\boldsymbol{\Lambda}^{-1} & \mathbf{0} \\ \mathbf{0} & \mathbf{I} \end{bmatrix} \mathbf{U}^T \mathbf{U} \begin{bmatrix} \boldsymbol{\Lambda} & \mathbf{0} \\ \mathbf{0} & \mathbf{I} \end{bmatrix} \mathbf{X}^{-1} \quad (\text{A.8})$$

$$= \mathbf{X} \begin{bmatrix} \mathbf{F} & \mathbf{0} \\ \mathbf{0} & \mathbf{I} \end{bmatrix} \mathbf{X}^{-1} \quad (\text{A.9})$$

This equation may be more recognizable in the special case for which $\mathbf{L} = \mathbf{I}$, when the generalized singular value decomposition in Eq. (A.1) and Eq. (A.2) collapses to the standard singular value decomposition $\hat{\mathbf{G}} = \mathbf{U}\boldsymbol{\Lambda}\mathbf{V}^T$ so that \mathbf{R} becomes

$$\mathbf{R} = \mathbf{V}\mathbf{F}\mathbf{V}^T \quad (\text{A.10})$$

where diagonal matrix \mathbf{F} contains the filter factors for the zeroth-order Tikhonov regularization:

$$F_{i,i} = \frac{\lambda_i^2}{\lambda_i^2 + \nu^2} \quad (\text{A.11})$$

VITA

Andrew Ganse is a PhD candidate in the UW Department of Earth and Space Sciences, focusing on inverse theory and theoretical seismology as they apply to underwater acoustics at the ocean bottom. He also has worked as a staff research scientist at UW's Applied Physics Laboratory (APL-UW) since 1999, working on ocean bottom geophysical problems for most of that time, but also ocean surface radar scatterometry and radio-Doppler based planetary gravimetry. Andrew has kept his role as a staff researcher at APL-UW throughout his PhD work, supported in part by the APL Graduate Fellowship (APL-UW's grow-your-own-P.I. program), and in later years finishing the PhD while employed by APL-UW's North Pacific Acoustic Laboratory research group. After graduation Andrew will continue his career at APL-UW as a new Principal Investigator. He may be contacted at aganse@apl.washington.edu.